Physics beyond the Standard Model Enhanced through Quantum Information

Xiangjun Tan, z5343935
Supervisor: Prof. Susan Coppersmith

A Literature Review submitted to the University of New South Wales

in partial fulfilment of the degree of Bachelor of Science (Honours)

School of Physics

Faculty of Science

November 2024

Typeset in LaTeX 2_ε.

I hereby declare that this submission is my own work and to the best of my knowledge it contains no materials previously published or written by another person, or substantial proportions of material which have been accepted for the award of any other degree or diploma at UNSW or any other educational institution, except where due acknowledgement is made in the thesis. Any contribution made to the research by others, with whom I have worked at UNSW or elsewhere, is explicitly acknowledged in the thesis. I also declare that the intellectual content of this thesis is the product of my own work, except to the extent that assistance from others in the project's design and conception or in style, presentation and linguistic expression is acknowledged.

Xiangjun Tan

Acknowledgements

I am deeply grateful to all those who have supported and guided me in completing this one-hundred-page honours thesis.

First and foremost, I would like to express my sincere appreciation to my thesis supervisor, Prof. Susan Coppersmith, for her invaluable guidance, continuous support, and encouragement over these two years. Her insight, expertise, and passion for physics have been a constant source of inspiration and have significantly shaped my research approach. I am especially grateful for her countless hours reviewing my work and providing feedback with constructive criticism.

I also thank the Physics faculty members for fostering a stimulating academic environment. Special thanks go to Dr. Michael Schmidt and Prof. Baha Balantekin for their insightful discussions and for challenging me to think critically and creatively about complex problems.

To my fellow students and friends, Dr Zhanning Wang and Zhaoyan Liu, and also to my other friends, your camaraderie and mutual support have made this journey bearable and enjoyable. Thanks to all the UNSW Research Seminar Association executive members, I enjoyed working with you to make RSA become a larger society with 2000 members over these two years from zero; thank you for supporting my leadership as the president, which is my honour.

I am profoundly grateful to my family for their unwavering support and love. To my parents, thank you for believing in me and always encouraging me to pursue my passions, no matter how challenging they seem. Thank you all for supporting me in studying overseas at UNSW.

Lastly, I would like to acknowledge the countless physicists and scholars whose work laid the foundation for my research. Their dedication to advancing the field of physics continues to inspire me.

Thank you all for your support, guidance, and encouragement. This thesis would not have been possible without you.

Abstract

Nuclear structure plays a pivotal role in dark matter direct detection experiments, as understanding nuclear interactions can enhance the sensitivity and accuracy of these quantum technology-based studies. The nuclear structure of the target material critically influences the scattering cross-sections and the energy transfer during interactions, thereby providing a fundamental framework for researchers to characterize and differentiate potential dark matter interaction mechanisms accurately. This project aims to enhance the application of the Variational Quantum Eigensolver (VQE) algorithm on Noisy Intermediate-Scale Quantum (NISQ) devices by investigating the ground-state properties of the Nuclear Shell Pairing Model. A primary focus of this research is to investigate and mitigate errors that affect the accuracy of estimated energy differences; a comprehensive benchmarking framework was established to validate the effectiveness of our error mitigation strategies on noisy quantum devices. By thoroughly investigating the impacts of quantum errors and model configurations, our mitigation strategies reduced energy differences by up to 99.56%, indicating a promising pathway toward error-resilient quantum computations to solve the problem for complex nuclear systems.

Contents

When theory and experiment agree, that is the time to be especially suspicious.

Niels Bohr

1 Dark Matter Interaction & Detection

Dark matter (DM) is a mysterious and invisible substance that makes up about 26% of the universe. Unlike ordinary matter, it does not emit, absorb, or reflect light, making it detectable only through its gravitational effects on visible matter, radiation, and the large-scale structure of the universe. Scientists infer its existence by observing phenomena such as the rotation curves of galaxies and gravitational lensing. To better understand the cosmic composition, Fig.1.1 illustrates the distribution of dark matter alongside dark energy and ordinary matter, highlighting the significant role dark matter plays in the universe's overall mass-energy content.

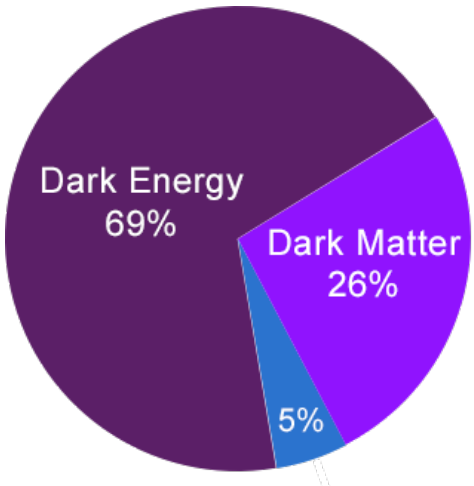

Figure 1.1: The universe's composition: 69% Dark Energy, 26% Dark Matter, and 5% Ordinary Matter. Dark Energy is the dominant component driving the accelerated expansion of the universe, while Dark Matter contributes to the gravitational structure. Ordinary Matter makes up the visible universe, including stars and planets. Source: Chandra X-ray Observatory.

Several astronomical measurements support the existence of Dark Matter like in Ref.[1, 2], one of

the most prominent being the Weakly Interacting Massive Particle (WIMP) model [3, 4]. WIMPs are theoretical candidates for DM, characterized by their non-relativistic mass and interactions primarily through nuclear force and gravity. This model has been posited to explain the so-called missing mass in the universe's mass-energy density [2]. However, a major question remains: *How can we detect DM or measure its corresponding signatures?*

Unlike normal matter, DM including WIMPs are invisible because they do not interact with electromagnetic force if the hypothesis is true [4]. The only way we can see them is by some other force in the Standard Model Framework; like some of them, they are heavy, and they can interact with the strong force within the nuclei; the theory can be found in the Appendix.A.1.1. The cross-section of the Nucleon will not depend on the wavefunction according to the Eq.A.21 under low energy case, so the symmetry restriction and non-elasticity elastic behaviour will be more important than the shape of potential.

To address this, we consider an elastic scattering process between a nucleon and a DM particle χ, assuming a low-energy regime where relativistic effects can be ignored [5]. In this scenario, the interaction can be described by a set of four-fermion operators, denoted by $\hat{O}$ in Eq.A.46 in the Appendix. These operators can be reduced or simplified up to second-order terms and are primarily dependent on key variables such as the momentum transfer $p(q)$, relative velocity v, and the spins of the nucleon and DM particle, denoted by $S_{N,\chi}$. The set can be found in Tab.A.1, and for more details about the EFT operators and symmetries, they can be found in the Appendix.A.1.2.

To detect dark matter interactions, researchers have developed a variety of experimental techniques focused on measuring nuclear recoil events caused by DM particles colliding with nuclei [6, 7]. These direct detection experiments typically involve highly sensitive detectors placed deep underground to minimize interference from cosmic rays and other background noise. Technologies such as cryogenic detectors, liquid noble gas detectors (like those using Xenon or Argon), and scintillating crystals are employed to capture and measure the faint signals produced by these interactions. Advanced statistical methods are applied to distinguish genuine DM signals from background events, and ongoing efforts aim to improve detector sensitivity and expand the search range to explore different mass and cross-section parameter spaces. Experimental details are in the Appendix A.2.

The energy transfer (100keV) is small in these low-energy cases, far below the nuclear ground state energy and its spectrum (100GeV). As a result, the potential interactions between DM and nucleons do not excite the atomic structure, meaning all nucleons remain in the same eigenstate post-interaction. Due to the total calculation is very complicate, we have demonstrated a easier case with scalar interaction operators only in the Appendix.A.1.3 for a Deutrium-like atom (The target nucleus will be significantly larger than the Deutrium, so the many-body calculations will include many terms). Within this framework, the calculations are directly based on the target nuclear response function A.52 that corresponds to the nuclear recoil and recoil energy; the measurement of nuclear recoil becomes the key signature of a DM interaction. Different operators govern the response of the nucleus to this interaction, and experiments that aim to detect this response are referred to as direct detection experiments.

Since quantum simulation could be used with qubits and their entanglement properties to simulate other many-body systems' behaviour [8]. In our project, the basic idea is to use quantum technologies to help us understand the internal structure of the target nucleus for direct detection, but nowadays, quantum computers with imperfect gate fidelity cannot give us a reliable result, so there is a need for us to investigate how to reduce the errors on the quantum computer and also how well the factors influence on the noisy result.

In summary, accurate calculations of the nuclear structure of target materials are essential for elucidating the properties of dark matter, as they directly impact the theoretical predictions of dark matter-nucleus interaction cross-sections [9, 10]. Quantum computing presents a promising avenue

for achieving more precise nuclear structure calculations due to its potential to handle complex quantum many-body problems more efficiently than classical methods [11, 12]. However, current quantum computers are constrained by limitations in qubit coherence, gate fidelity, and overall computational capacity, which hinder their ability to perform high-precision calculations required for detailed nuclear modelling [13]. To overcome these challenges, we optimise the computational strategies using Variational Quantum Eigensolvers, a hybrid quantum-classical algorithm. Additionally, we employ simplified models of nuclear systems to systematically quantify and correct for errors, thus paving the way for more reliable nuclear structure calculations on near-term quantum devices.

2

Quantum Information & Quantum Simulation

Quantum computers in the most common case are designed to use the qubit as the minimal operation unit and the register. Unlike classical bits, which represent either a 0 or 1, qubits can exist in superpositions of states, enabling the simultaneous processing of vast amounts of data. The way we convert the problems into the quantum observables and operating qubits array are called quantum computation.

In 2019 researchers from Google demonstrated the practical potential of quantum computers to solve complex problems [11], and predict the potent benefit of other problems such as factoring large numbers or simulating quantum systems, that are intractable for classical computers, even though there are still some arguments about the quantum supremacy [14]. In this section, we will review quantum technologies and clarify how we will use it in our project.

2.1 Quantum Computation

2.1.1 Basics of Quantum Register

Usually, a well-defined two-level fermionic quantum system is a proper carrier for locating a quantum register corresponding to two different eigenstates, which we call a quantum bit or Qubit [15, 16]. Mathematically, these eigenstates must be orthonormal states that simultaneously obey the properties of normalization and orthogonalized, so the inner product of these eigenstates will be $\langle\psi_a|\psi_b\rangle = 0$ and $\langle\psi_i|\psi_i\rangle = 1, i \in a, b$. However, it is possible to use other anharmonic quantum systems with more than two distinguishable eigenstates, and it could be used to define Qutrit ($N = 3$) and Qudit ($N = 4$), etc [17]. Notice that if the energy difference is the same, controlling the system to enter a certain excitation state is nearly impossible, but when it is mapped to the Higher dimensional Hilbert space, the eigenstates should also be orthogonal to each other.

Typically, the effective wavefunction for a Qubit can be written down with two complex coefficients α and β with the relationship $|\alpha|^2 + |\beta|^2 = 1$ similar to a spin $\frac{1}{2}$ system:

$$|\psi\rangle = \alpha|0\rangle + \beta|1\rangle \tag{2.1}$$

The natural manifold for geometrical representation of the pure state space with a spin $\frac{1}{2}$ system is the Bloch Sphere. The coefficients can be expressed as:

$$\begin{aligned} \alpha &= e^{i\delta} \cos\frac{\theta}{2} \\ \beta &= e^{i(\delta+\varphi)} \sin\frac{\theta}{2} \end{aligned} \tag{2.2}$$

It's not hard to get the eigenstates defined along the z-axis that $|0\rangle = \begin{bmatrix} 1 \\ 0 \end{bmatrix}$ and $|1\rangle = \begin{bmatrix} 0 \\ 1 \end{bmatrix}$. The definition of combinations of eigenstates on the z-axis can express the eigenstates in other axes.

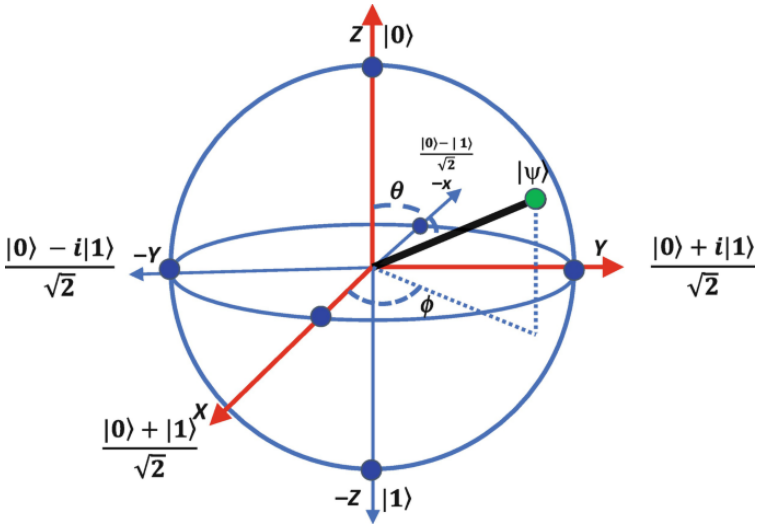

Figure 2.1: The surface of the Bloch sphere represents the pure quantum state, but it should be noted that the sphere is not orthogonal in itself [18]. The x,y, and z axes correspond to the axes in Euclid space, and the coefficient δ is cancelled because it represents a global phase.

The density matrix $|\psi\rangle\langle\psi|$ is very useful to describe a quantum system. For a Qubit, we use the Pauli Vector $\vec{P}$ with identity matrix to define the density matrix:

$$\rho = \frac{1}{2}(I + \vec{P}) \tag{2.3}$$

where the Pauli vector is defined by:

$$\vec{P} = \sum_{i \in x,y,z} \sigma_i r_i, \vec{r_i} \in \text{coordinates of real space} \tag{2.4}$$

Different from Qubit, the Qutrit has three independent eigenstates [19]. It is usually located by a spin1 Bosonic system with a different commutation and representation algebra. All of the states could be represented in the Poincaré sphere with the normalized polarization vector:

$$\mathbf{S} = \frac{1}{S_0} \begin{bmatrix} S_0 \\ S_1 \\ S_2 \\ S_3 \end{bmatrix} \tag{2.5}$$

In this literature review, Qubit's representation will be deployed to all of the models and all the quantum operations.

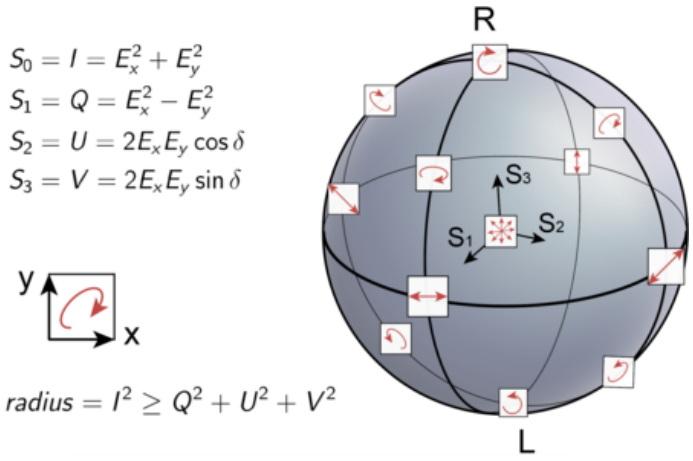

Figure 2.2: The Poincaré sphere is a geometrical representation of the state of the Bosonic system on a unit sphere, where each point corresponds to a unique polarization state. [20]

2.1.2 Universal Set of Quantum Gates

A universal gate set is a collection of quantum gates consisting of one and two Qubits that can approximate any quantum gate to a specified level of precision [21]. For any unitary operation U, we can find a sequence for a combination of gates in universal gate set U_{approx} that satisfies $\|U - U_{\text{approx}}\| < \epsilon$, where $\epsilon > 0$.

According to the Solovay-Kitaev Theorem, the running time of an algorithm using one gate set is equivalent to that using another gate set, differing only by logarithmic factors [22]. This implies that quantum speedups of polynomial magnitude are consistent across different gate sets, and the universal gate set is not unique. Consequently, to harness the complete capabilities of quantum computing, it is only necessary to implement a finite set of gates [23].

Basically, a universal quantum gate set will include some single qubit gates that can rotate the Pauli vector point to every point at the surface of the Bloch sphere. Each single-qubit gate corresponds to a 2x2 unitary matrix with the relation $U^\dagger U = UU^\dagger = I$ and $U^\dagger = U^{-1}$, and these matrices can generate any element of SU(2) representation since they form a dense subset. All of the single qubit gates could be decomposed into the rotations around x,y,z axes with corresponding phases.

$$U_{Euler} = e^{i\alpha} R_z(\beta) R_y(\gamma) R_z(\delta) \tag{2.6}$$

However, this is not enough to become a many-body interacting system, so we need to make the qubits into an entanglement state to get the higher dimension of Hilbert space, so we will need to define a multi-qubit gate with the square matrix of dimension 2^N instead. The most often used multi-qubit gate is the CNOT or Controlled-NOT gate with two qubits:

$$U_{CNOT} = \begin{bmatrix} 1 & 0 & 0 & 0 \\ 0 & 1 & 0 & 0 \\ 0 & 0 & 0 & 1 \\ 0 & 0 & 1 & 0 \end{bmatrix} \tag{2.7}$$

Some new generation devices will use a more efficient gate instead of a CNOT gate called ECR. Actually, ECR operation is the entangling part of the CNOT operation, which is given out by:

$$ECR = \frac{1}{\sqrt{2}} \begin{bmatrix} 0 & 1 & 0 & i \\ 1 & 0 & -i & 0 \\ 0 & i & 0 & 1 \\ -i & 0 & 1 & 0 \end{bmatrix} = \frac{1}{\sqrt{2}}(IX - XY) \tag{2.8}$$

The flourishing quantum computing community, especially IBM Quantum Hardware, has created a native basic gate set for the dominant superconducting Qubit nowadays. It has the following gates $U_{CNOT}, X, ID, R_z, \sqrt{X}$. Where the R_z is the rotation gate along the z-axis, and X gate is the Pauli X operation, $\sqrt{X}$ can be equivalently defined as $R_z(\frac{\pi}{2})$ gate with a $-\frac{\pi}{4}$ global phase:

$$R_x(\pi/2) = \frac{1}{\sqrt{2}} \begin{bmatrix} 1 & -i \\ -i & 1 \end{bmatrix} = e^{-i\frac{\pi}{4}} \sqrt{X} \tag{2.9}$$

$$X = \begin{bmatrix} 0 & 1 \\ 1 & 0 \end{bmatrix} \tag{2.10}$$

$$R_z(\lambda) = \exp\left[-i\frac{\lambda}{2}Z\right] = \begin{bmatrix} e^{-i\frac{\lambda}{2}} & 0 \\ 0 & e^{i\frac{\lambda}{2}} \end{bmatrix} \tag{2.11}$$

2.1.3 Quantum Dynamics

In real-world experiments, observables correspond to physical properties that can be measured. For quantum hardware with N Qubits, the observables O can be expressed by the sum of the Pauli matrix product [24]:

$$O = \sum_{k=1}^{K} \alpha_k P_k, \quad P_k \in \{I, X, Y, Z\}^{\otimes N}, \quad \alpha_k \in \mathbb{R} \tag{2.12}$$

But sometimes, the system is not static, like the time-dependent wavefunction with a known initial state corresponding to an example time-dependent quantum system below under the Heisenberg picture.

$$|\psi(t)\rangle = e^{-iHt}|\psi(0)\rangle \tag{2.13}$$

According to the Trotterized Real-Time Evolution [25], it can approximate the time evolution of a system for a time slice with time step $\frac{t}{n}$ by re-writing the Hamiltonian into time-independent $H = \sum_j a_j H_j$. The wavefunction for a certain time can then be approximated as:

$$|\psi(t)\rangle \approx \left(\prod_j e^{-ia_j H_j \frac{t}{n}}\right)^n |\psi(0)\rangle \tag{2.14}$$

The Suzuki-Trotter formula can have some improvements that could reduce the error for it [26], like for second-order decomposition on two operators A and B:

$$e^{A+B} \approx e^{B/2} e^{A} e^{B/2} \tag{2.15}$$

Under the second-order approximation (Higher-order approximation will have less error, but it will increase the competitivity), the time-evolution operator can be expressed as the product form below:

$$U = e^{-it(H+\Delta H)} = e^{-i\frac{t}{2}\Delta H} e^{-itH} e^{-i\frac{t}{2}\Delta H} + \mathcal{O}\left(t^3\right) \tag{2.16}$$

So, whether the described system is time-dependent or time-independent, we can always find a mapping from the system's unique Hamiltonian to the sum of the tensor product of Pauli operators. However, not all mappings are generally effective especially the direct mapping as we shown in Fig.2.3. We must create an adaptive mapping using the system's properties and mathematical structure to lower the usage of quantum resources and evaluation time. Different encoding processes, from origin representation to qubit spin representation, will be used to describe different systems effectively [27, 28]. The quantum sampler could give the outcome, which takes thousands of measurements each time to get the final probability of each state after the quantum circuit operation [12].

2.1.4 Operator Transformation

To achieve higher encoding efficiency, we will first identify the quantum system by the commutation algebra to the quasi-fermion and quasi-boson systems. For Fermionic system encoding, the occupation number for those type systems can only be 0 or 1 under the second quantization. So there is a demand for a transformation to map spin operators to fermionic creation and annihilation operators.

The Jordan-Wigner transformation is the most common way to encode a fermionic system, which is topologically chained in a combination of non-closed loop forms [29, 30].

$$h_i = \sum_{pq\ldots rs} c_{i,pq\ldots rs} a_p^\dagger a_q^\dagger \ldots a_r a_s \tag{2.17}$$

Where the creation and destruction operator within the new form can be expressed as:

$$\begin{aligned} c_j^\dagger &= \left(\prod_{k=1}^{j-1} -\sigma_k^z\right) \frac{\sigma_j^x - i\sigma_j^y}{2} \\ c_j &= \left(\prod_{k=1}^{j-1} -\sigma_k^z\right) \frac{\sigma_j^x + i\sigma_j^y}{2} \end{aligned} \tag{2.18}$$

For Bosonic Fock state encoding, in quantum mechanics the bosonic system follows the commutation relation for:

$$\left[a, a^\dagger\right] = aa^\dagger - a^\dagger a = 1 \tag{2.19}$$

So for an N quanta bosonic system, for direct mapping we need n qubits with the relation $n = \lceil \log_2(N+1) \rceil$ [31]. The creation operator, when acting on a Fock state it will increase the number of particles [32]:

$$a^\dagger|n\rangle = \sqrt{n+1}|n+1\rangle \longrightarrow a^\dagger|n\rangle_{\text{qubits}} = \sqrt{n+1}|n+1\rangle_{\text{qubits}} \tag{2.20}$$

Also for the annihilation operator, which will reduce the number of particles:

$$a|n\rangle = \sqrt{n}|n-1\rangle \longrightarrow |n\rangle_{\text{qubits}} \rightarrow \sqrt{n}|n-1\rangle_{\text{qubits}} \tag{2.21}$$

Generally, all of the states will be represented by the qubit spin representation, and it will be more effective if we use binary to encode the occupation number.

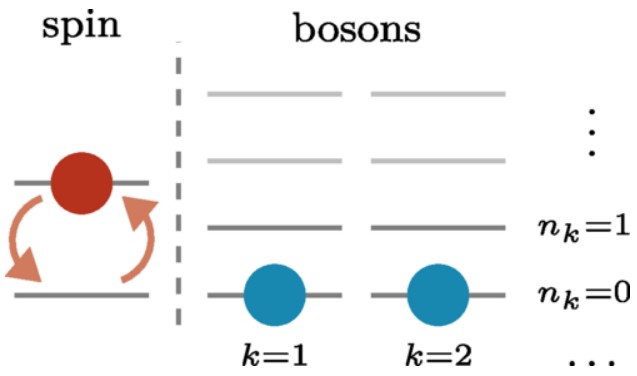

Figure 2.3: In the Scheme for Bosonic direct mapping, the spin representation can be converted to the occupation representation, so for k bosonic particles with n_k possible occupation number for each will need $N = n \cdot (k+1)$ qubits in total [33].

2.1.5 Variational Quantum Eigensolver

The Variational Quantum Eigensolver (VQE) algorithm is a hybrid quantum-classical algorithm designed to find a quantum system's ground state energy in the NISQ era [8, 34, 35].

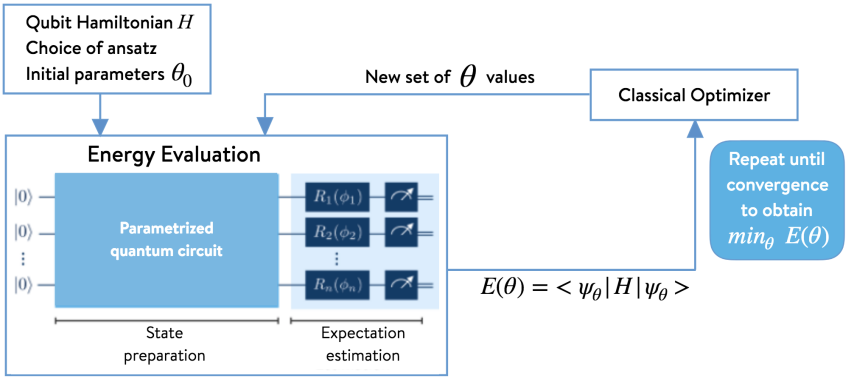

Figure 2.4: VQE is a quantum-classical hybrid algorithm, the system Hamiltonian and the parameterized wavefunction $|\Psi\rangle$ will be encoded to quantum circuits; the expectation value will estimated by the measurement outcome and sent to the classical optimizer to update the parameter θ set. [36].

As the Fig.2.4 shown above, the basic workflow of the VQE algorithm involves the following steps:

1. **Parameterization of the Trial Wave Function**: The quantum state $\psi(\theta)$ is parameterized by a set of parameters $\theta = (\theta_1, \theta_2, \ldots, \theta_n)$. This trial wave function is typically prepared using a quantum circuit with gates that depend on these parameters.

2. **Measurement of the Hamiltonian**: The Hamiltonian $\hat{H}$ of the system is expressed as a sum of Pauli operators $\hat{H} = \sum_i \alpha_i \hat{P}_i$. The expectation value of the Hamiltonian is measured by preparing the quantum state $\psi(\theta)$ and measuring it in various bases corresponding to the Pauli operators $\hat{P}_i$.

3. **Classical Optimization**: The measured expectation value $\langle\psi(\theta)|\hat{H}|\psi(\theta)\rangle$ is fed into a classical optimization algorithm, which updates the parameters θ to minimize this expectation value. Common optimization algorithms include gradient descent, Nelder-Mead, and COBYLA.

4. **Iteration**: Steps 1 through 3 are repeated iteratively until the expectation value converges to a minimum, approximating the system's ground state energy.

The goal of the VQE algorithm is to find the set of parameters θ that minimizes the expectation value of the Hamiltonian:

$$E(\theta) = \langle\psi(\theta)|\hat{H}|\psi(\theta)\rangle \tag{2.22}$$

This expectation value can be expressed as a weighted sum of the expectation values of the Pauli operators:

$$E(\theta) = \sum_i \alpha_i \langle\psi(\theta)|\hat{P}_i|\psi(\theta)\rangle \tag{2.23}$$

The optimization problem is then to find:

$$\theta_{\text{optimized}} = \arg\min E(\theta) \tag{2.24}$$

where $\theta_{\text{optimized}}$ represents the optimal set of parameters that minimize the expectation value of the Hamiltonian, thus approximating the ground state energy as a result shown in Fig.2.5.

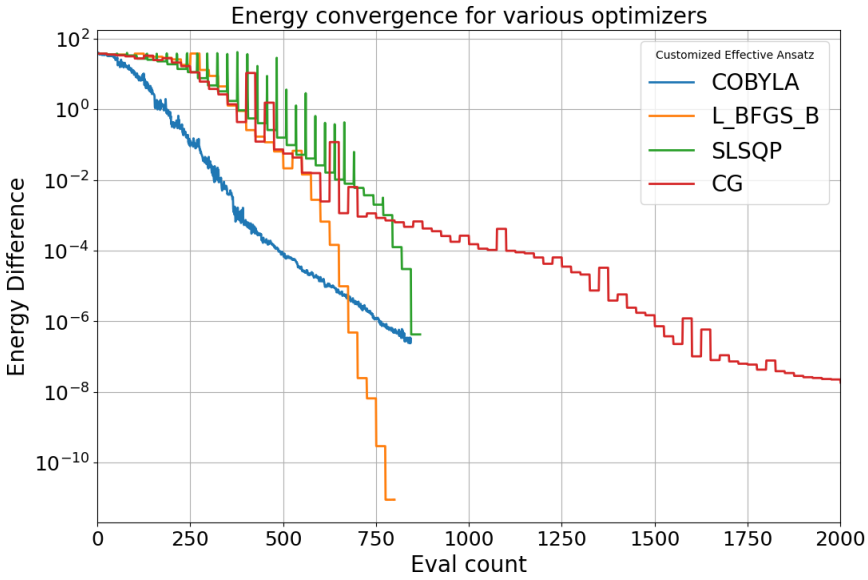

Figure 2.5: This Figure shows the case for a normal iteration process; the energy difference ($E_{ref} - E_{est}$) between the reference level and the estimation value will gradually reduce with evals. However, various optimizers could have different convergence speeds, which is more dependent on the features of our system. So it is also important to create the effective *ansatz* and use the proper optimizer [32].

Noticed that the VQE will be based on the quantum estimator primitives, a computational tool or algorithm used to infer the parameters or properties of a quantum system from measurement data, optimizing accuracy and minimizing uncertainty within the constraints of quantum mechanics [12], in our project the quantum estimator will be the core resource for us to analysis.

2.2 Noisy Quantum Computing

Nowadays, quantum devices still face some technological problems. Some researchers think NISQ devices are dead (They cannot perform and solve any real-world application) [37]; the limitations include gate error, measurement error, qubit connectivity, and gate fidelity.

Later in this section, we will introduce the quantum operation's qubit noise with quantum error in 2.2.1 and review the quantum error mitigation strategies in 2.2.3. These strategies could help us enhance the performance of our code and the noise model's establishing accuracy.

2.2.1 Characterization of Quantum Errors

Characterizing quantum errors is crucial for understanding and mitigating the impact of noise on quantum computations [38, 39]. Quantum errors can be broadly categorized into coherent and incoherent errors. The coherent errors are systematic and arise from deterministic imperfections in

the control of quantum gates, such as over-rotation or under-rotation. These errors can often be corrected through precise calibration and control techniques.

Mathematically, if we consider a single-qubit rotation gate $R(\theta)$ intended to rotate a qubit by an angle θ, a coherent error might result in an actual rotation by $\theta + \epsilon$, where ϵ is a small systematic error. The incorrect rotation can be expressed as:

$$R(\theta+\epsilon) = \begin{pmatrix} \cos\left(\frac{\theta+\epsilon}{2}\right) & -i\sin\left(\frac{\theta+\epsilon}{2}\right) \\ -i\sin\left(\frac{\theta+\epsilon}{2}\right) & \cos\left(\frac{\theta+\epsilon}{2}\right) \end{pmatrix} \tag{2.25}$$

This deviation from the ideal rotation gate can accumulate over many operations. Incoherent errors, on the other hand are random and typically result from interactions with the surrounding environment, leading to decoherence. Decoherence causes qubits to lose their quantum properties, such as superposition and entanglement, thereby degrading the overall performance of the quantum system [40].

A common model for decoherent errors is the phase damping channel, which affects the coherence between the basis states $|0\rangle$ and $|1\rangle$. The action of a phase damping channel on a qubit state ρ can be represented using Kraus operators E_0 and E_1:

$$E_0 = \begin{pmatrix} 1 & 0 \\ 0 & \sqrt{1-\lambda} \end{pmatrix}, \quad E_1 = \begin{pmatrix} 0 & 0 \\ 0 & \sqrt{\lambda} \end{pmatrix} \tag{2.26}$$

where λ is the probability of phase damping occurring. The density matrix of the transformed state ρ' after passing through the phase damping channel is given by:

$$\rho' = E_0\rho E_0^\dagger + E_1\rho E_1^\dagger \tag{2.27}$$

Various techniques are employed to characterize these errors, including randomized benchmarking [41], quantum process tomography [42, 43], and error-mitigation strategies [44, 45]. Randomized benchmarking involves applying a sequence of random gates to a quantum system and measuring the resulting error rates to infer gate fidelities. Quantum process tomography provides a detailed map of how quantum operations transform input states into output states, enabling the identification of specific error types.

So, to realize how much the noise affected our measured quantum states, it is crucial to define a physical property to compare with the expected ideal quantum states. Fidelity is a similarity measure between two quantum states, described by the density matrices ρ and σ [46]. It quantifies how well a quantum operation preserves the state of a system or how closely a given quantum state approximates another, so the best value will be $F = 1$ corresponding to the zero error. It is defined as:

$$F(\rho,\sigma) = \left(\mathrm{Tr}\sqrt{\sqrt{\rho}\sigma\sqrt{\rho}}\right)^2 \tag{2.28}$$

For pure states represented by $|\psi\rangle$ and $|\phi\rangle$, the fidelity simplifies to:

$$F(\rho,\sigma) = |\langle\psi|\phi\rangle|^2 \tag{2.29}$$

The Randomized benchmarking technology will be used for quantum gates to estimate the gate fidelity [41, 47], typically involving a subset of the Clifford gates. Clifford gates are a group of quantum operations that map Pauli operators to other Pauli operators under conjugation.

$$CP_iC^\dagger = P_i', \quad \forall i = 1,\ldots,n \tag{2.30}$$

where P_i is any Pauli operator acting on n qubits, and P_i' is the resulting Pauli operator after conjugation by C. Here are the steps to finish the benchmark based on Ref.[41].

1. **Prepare the Initial State**: Initialize the quantum system in a known state, often the $|0\rangle$ state for qubits.

2. **Apply a Random Sequence of Clifford Gates**: Generate a sequence of random Clifford gates $\{C_1, C_2, \ldots, C_m\}$ and apply them to the quantum system. The sequence length m varies in different experiments to observe how errors accumulate over longer sequences.

3. **Apply the Inversion Gate**: Compute and apply an inversion gate C_{inv} such that in the absence of errors, the composite operation $(C_{\text{inv}} \cdot C_m \cdot \ldots \cdot C_2 \cdot C_1)$ returns the system to the initial state.

4. **Measure the Output State**: Measure the quantum state of the system. The probability of finding the system in its initial state provi4 des the fidelity of the gate sequence.

5. **Repeat with Multiple Sequences**: Repeat steps 1 to 4 with many different random sequences of gates for each sequence length m to obtain a statistically significant measure of fidelity.

6. **Analyze the Data**: Plot the fidelity as a function of the sequence length m. Fit the resulting decay curve to an exponential function, $F(m) = Ap^m + B$, where p is the parameter related to the average gate fidelity. The decay rate provides an estimate of the average error rate per gate.

Currently, the single-qubit gate fidelity NISQ devices attach 99.99% and 99.9% for multi-qubit gates [48].

2.2.2 Noisy Quantum Local Simulators

Generally, noisy quantum local simulators are computational tools used to model the behaviour of quantum systems while incorporating various noise models to simulate realistic conditions. These simulators are particularly useful for testing quantum algorithms, like variational quantum algorithms, where the effects of noise can significantly impact the accuracy and convergence of the algorithm. There are methods to perform a qubit on a local classical computer.

However, those can only simulate the ideal noiseless case; real quantum devices are noisy, and we need to fit a mathematical noise model for them if we want to investigate their noise features. For more details of quantum operation errors, here is a summary in Tab.2.2 concluded by the Qiskit Team. By calibrating and measuring the current targeting quantum devices, we can build the approximated noise model to simulate the noise behaviour on NISQ devices.

So, the workflow involves fitting the noise behaviour and applying it mathematically to our simulation results; different simulation methods could also affect the noisy results due to truncation and random number generation.

The error could also occur during the measurement and readout. Note that there is a difference between the measurement and readout process as shown in Tab.2.3. Measurement collapses a quantum state into a classical outcome based on quantum rules. The readout is the physical and practical process of recording and interpreting the outcome of the measurement, which can introduce additional errors that must be mitigated.

Simulation Method	Description	Use Case
Statevector	Represents the full quantum state as a vector. It provides an exact simulation of quantum circuits but scales exponentially with the number of qubits.	Ideal for simulating small quantum systems or circuits with low qubit count.
Density Matrix	Represents mixed quantum states, accounting for decoherence and noise. Requires more memory than state vector simulations.	Useful for simulating noisy quantum circuits or systems with mixed states.
Matrix Product State	Efficient for simulating one-dimensional quantum systems with limited entanglement. Scales well with system size.	Best suited for large quantum systems with low entanglement.

Table 2.1: Comparison of Different Quantum Simulation Methods [12]. Obviously, the memory and performance cost by the state vector method will be the lowest due to fewer elements during the calculation. Unlike the State vector and Density Matrix, the Matrix Product State is a tensor network state that could describe the quantum system in low entanglement; more details will be in the Appendix.

Aspect	Measurement	Readout
Nature	A quantum process (wavefunction collapse).	A classical process (detecting the result).
Scope	Involves collapsing the quantum state.	Involves interpreting and recording the result.
Errors	Quantum uncertainties (inherent in quantum mechanics).	Hardware-induced errors (misread states).
Dependency	Defined by quantum mechanics.	Defined by the physical hardware system.
Output	A probabilistic quantum state outcome ($\|0\rangle$ or $\|1\rangle$).	A classical bit (0 or 1) recorded by the system.

Table 2.3: Key differences between measurement and readout in quantum computing.

With the features above, it is obvious that the outcome couldn't be the same as the classical calculation; to investigate and quantify those effects, a noisy quantum simulator should be established to avoid the waste of quantum device runtime.

2.2.3 Techniques for Quantum Error Mitigation

Even though we mentioned that NISQ is limited in capability in the last section, multiple strategies exist to enhance the performance of NISQ quantum channels through Quantum Error Correction (QEC) [49–51]. QEC is a crucial tool that protects quantum information from the detrimental effects of noise and decoherence, which are inherent in NISQ devices. It operates by encoding quantum information into a larger Hilbert space using additional qubits, allowing for detecting and correcting errors without measuring the quantum information directly, thereby preserving coherence and entanglement.

This section will review some existing efficient strategies and discuss how they can be deployed in our project to mitigate errors in NISQ devices. Indeed, the impact of errors can be mitigated not only at the level of software control, which involves optimizing quantum circuits and error mitigation techniques but also at the hardware level, through advancements in qubit design and environmental isolation. Furthermore, error suppression can also be achieved at the algorithmic level, where quantum algorithms are designed or adapted to be more resilient to noise and errors. These multi-layered strategies can significantly extend the practical usefulness of NISQ devices and improve the fidelity and reliability of quantum computations.

Whether we use the quantum estimator or quantum sampler, those primitives will always give feedback based on the shots of desired qubits. That corresponds to thousands of measurements and

Standard Error Function	**Details**
kraus_error	A general n-qubit error channel that is completely positive and trace-preserving (CPTP), represented by a set of Kraus matrices $[K_0, K_1, \ldots]$.
coherent_unitary_error	An n-qubit error characterized by a single coherent unitary operation, represented by a unitary matrix U.
pauli_error	An n-qubit Pauli error channel, which is a mixed unitary error described by a list of Pauli operators and their corresponding probabilities $[(P_0, p_0), (P_1, p_1), \ldots]$.
depolarizing_error	An n-qubit error channel where depolarization occurs with a specific probability p, uniformly distributing the error across all possible states.
reset_error	A single-qubit error in which the qubit is reset to the $\|0\rangle$ or $\|1\rangle$ state with respective probabilities p_0 and p_1.
thermal_relaxation_error	A single-qubit error channel that models thermal relaxation, defined by the relaxation time constants T_1 and T_2, the gate operation time t, and the excited state thermal population p_1.
amplitude_damping_error	A single-qubit error model that represents amplitude damping, characterized by a damping parameter λ and an excited state thermal population p_1.
phase_damping_error	A single-qubit error channel describing phase damping, parameterized by a phase damping rate γ.

Table 2.2: Overview of standard quantum error functions used in quantum error correction and simulation. Each function is described by its type (n-qubit or single-qubit) and the parameters that define the error model [12].

repeats of the total quantum circuits, which could be noisy and sensitive due to the measurement error. Luckily this type of error is generated with bias, so we can recover the origin noiseless measurement outcome by analysing the bias for each qubit on each state and then adding an inverse term to the outcome numerically.

As the Fig.2.6 shown, the readout error mitigator will generate a matrix 2^N by 2^N to calibrate the measurement outcome based on the assumption that the measurement error for different qubits are uncorrelated, this calibration will lead to an external mitigation complexity (O^{2N}) [52].

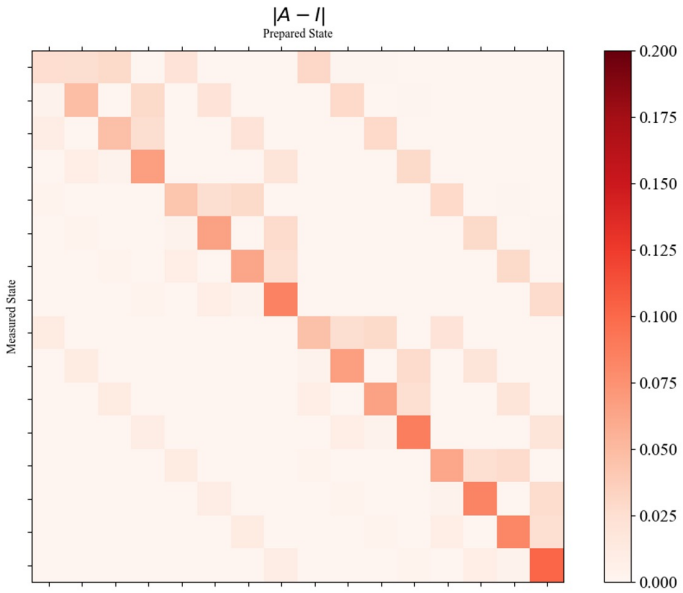

Figure 2.6: The figure shows the readout matrix of a four qubits system so 16 eigenstates in total, the heavy colour means higher probability distribution of the state. Ideally the colour will only appear on the diagonal line due to the measured states are exactly the prepared states, but according to the readout error the non-diagonal probability tends to be non-zero so the measured distribution will leak to the other states.

In our project, more strategies will be used to suppress the error and make better outcomes; the process description, like Zero Noise Extrapolation (ZNE) and Probabilistic Error Cancellation (PEC), will be in the Appendix.A.4 and A.5. On the hardware gate level, there are serval strategies like dynamical decoupling and Pauli gate twirling can be used to reduce the noise affect, more details will be in the Appendix.A.6.1 and A.6.2. In our VQE-based algorithm, multiple strategies will be deployed. Here is a performance view concerning their relative outcome error. The relative error will be reduced to an acceptable level with all strategies enabled [32]. However, more performance and gate costs will exist due to the extra manipulations [53].

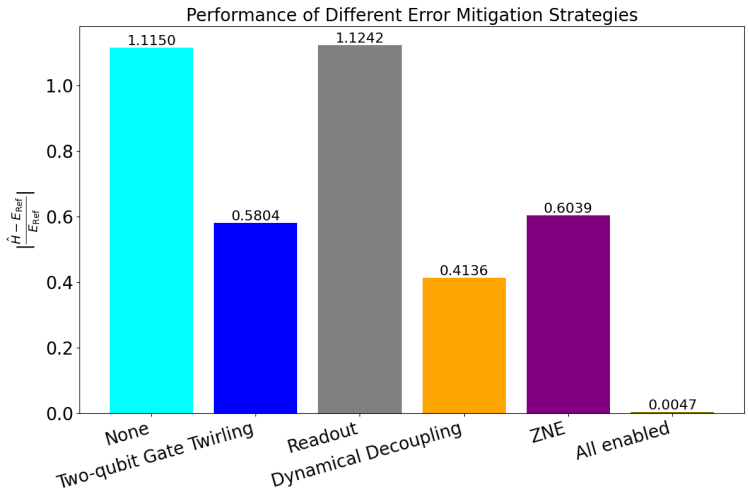

Figure 2.7: The figure shows the impact of different error mitigation techniques on the computed energy.

To evaluate the effectiveness of the error mitigation techniques, Fig.2.8 illustrates the resulting curves for various configurations.

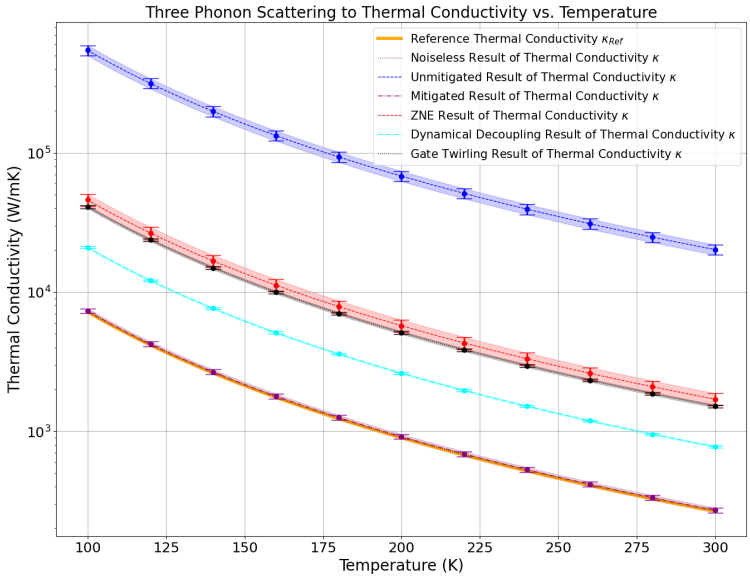

Figure 2.8: The figure illustrates that in a toy model of thermal conductivity calculation on NISQ devices, the estimated value could cause the final result of 1000 times more than we expected. However, with QEC strategies, the error could be reduced to an acceptable level, which is verified on a toy model. The ZNE and Dynamic Decoupling will significantly reduce the error rate according to the final outcome [32].

Based on the methods given above, it could be believed that in a toy model or low qubits usage with a thin circuit depth case, the total error and the fidelity could be mitigated to an acceptable level.

2.2.4 Quantum Volume

The Quantum Volume (QV) is a holistic metric introduced to evaluate the practical computational power of quantum devices. Unlike metrics based solely on qubit count or gate fidelity, Quantum Volume combines various factors such as the number of qubits, gate fidelity, coherence times, and qubit connectivity. The Quantum Volume of a device indicates its ability to perform complex quantum computations by running deep and wide quantum circuits with high fidelity.

In 2019, IBM's researchers modified the quantum volume definition to be an exponential of the circuit size [54]. Mathematically, Quantum Volume is defined as:

$$\log_2 V_Q = \arg\max_{n \leq N} \{\min[n, d(n)]\} \tag{2.31}$$

Where d represents the largest depth for a circuit with $n = d$ qubits and d layers that can be executed on the device with fidelity above a predefined threshold, typically 0.67 for Heavy Set [55].

Here is a figure to show how the randomized circuit is constructed, as shown in Fig.2.9. Note that the SU(4) operation corresponds to a two-qubit gate like CNOT and ECR gate, which could perform the rotation under that symmetry.

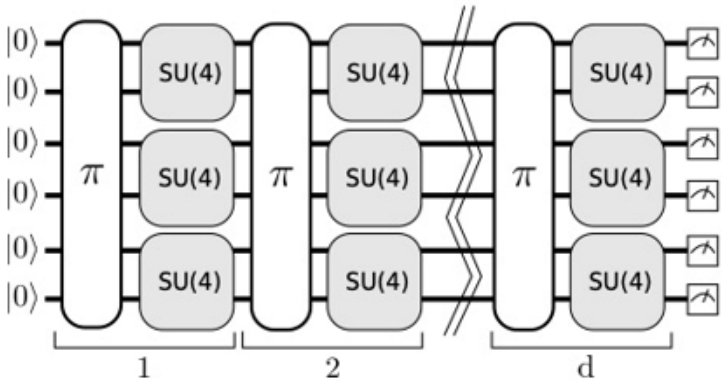

Figure 2.9: Example of a Quantum Volume Circuit Layout, the circuit begins with qubits initialized to $|0\rangle$ states. Each layer, labelled 1 to d, consists of randomized SU(4) gates applied to pairs of qubits, interspersed with permutation layers (π) that shuffle qubit pairs to maximize entanglement across the circuit. This structure repeats for d layers, followed by measurements on all qubits at the end [56].

To calculate Quantum Volume, the following steps are followed:

- **Random Circuit Generation:** A random quantum circuit is generated with $n = d$ qubits and depth d. The circuit applies a sequence of random gates, ensuring a mix of single- and two-qubit gates.

- **Execution and Measurement:** The quantum circuit is executed on the device, and the resulting state is measured.

- **Fidelity Evaluation:** Fidelity is assessed using cross-entropy benchmarking (XEB), which compares the measured output distribution p_{measured} to the ideal distribution p_{ideal}. The XEB fidelity F_{XEB} is calculated as:

$$F_{\text{XEB}} = \frac{1}{|S|} \sum_{s \in S} p_{\text{ideal}}(s) p_{\text{measured}}(s) \tag{2.32}$$

  Where S is a sample set of measurement outcomes. Remember for Quantum Volume to be valid, the average fidelity $\overline{F}$ must exceed a threshold ($\frac{2}{3}$).

With the Randomized circuit as Fig.2.9, we can run it many times and get the results, we will get the probability for each possible state, and we can calculate the mean probability in those states, then we can sum all the probabilities that are larger than the mean value which called Heavy Set like in Fig.2.10.

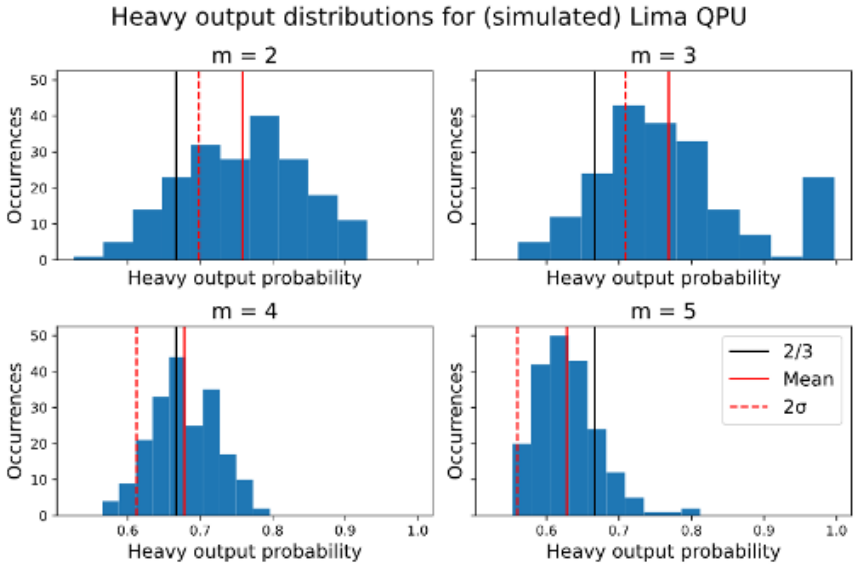

Figure 2.10: Heavy output distributions for the simulated Lima QPU at various circuit depths $m = 2, 3, 4, 5$. Each histogram represents the distribution of heavy output probabilities from multiple trials. The vertical black line corresponds to the theoretical success threshold of $2/3$, while the red dashed line indicates the mean heavy output probability for each depth. The shaded area around the mean represents the 2σ confidence interval, highlighting the variability in performance. This figure evaluates the Lima QPU's capability to generate heavy outputs as a function of increasing circuit complexity.

In this configuration, we will sum all the probabilities for states that are larger than the mean value of the probabilities, and then the Heavy Output Set has been set up and can be used to plot the distribution. If the sum is larger than the threshold for $\frac{2}{3}$ then it will pass with this Quantum Volume like for $m = 3$ case for $QV = 2^3$, but it will disagree with m=4 for $QV = 2^4$ due to the sum of the mean value is lower.

The difference from the gate fidelity also includes the factors that could affect the Quantum Volume (increasing the gate fidelity is not the only way to improve the Quantum Volume for a specific device:

1. **Qubit Quality:** Higher coherence times and lower error rates in qubits improve quantum volume, reducing the likelihood of errors during computation.

2. **Gate Fidelity:** The precision with which gates (single-qubit and two-qubit) are applied is critical. Higher gate fidelity allows for more accurate operations, impacting the depth and complexity of circuits that can be reliably executed.

3. **Qubit Connectivity:** The layout and connectivity of qubits (i.e., how qubits can interact with one another) affect the ability to apply two-qubit gates without significant error. Better connectivity reduces the need for additional operations to route qubit interactions, which can introduce errors.

4. **Error Mitigation Techniques:** Techniques that detect or correct errors (like error correction codes) can improve effective quantum volume by allowing deeper circuits with fewer overall errors.

5. **Noise Levels:** Background noise in the quantum system, including both thermal and environmental noise, can impact fidelity. Lower noise environments generally allow for higher quantum volume.

6. **Measurement Fidelity:** Accurate measurement is crucial since errors in the final measurement step can affect the observed fidelity, thus impacting the calculated Quantum Volume.

7. **Circuit Compilation Efficiency:** The ability of compilers to optimize circuits for specific hardware impacts the Quantum Volume. Efficient compilation reduces the number of necessary operations, thereby reducing errors and enhancing circuit depth.

8. **Calibration Frequency:** Regular calibration of qubits and gates ensures that the device performs optimally. Devices calibrated frequently tend to maintain higher fidelity over time, positively impacting Quantum Volume.

9. **Thermal Management:** For superconducting qubits and other temperature-sensitive quantum systems, maintaining a stable, ultra-cold environment is essential. Effective thermal management prevents decoherence and preserves qubit fidelity.

10. **Quantum Hardware Scalability:** As the number of qubits increases, managing and maintaining the quality of each qubit and gate operation across the entire system becomes challenging. High scalability with consistent performance across qubits improves Quantum Volume.

In summary, Quantum Volume reflects a device's ability to handle complex, high-depth quantum circuits and thus provides a realistic measure of its computational power. Devices with higher Quantum Volume are better suited to tackle intricate algorithms and demonstrate resilience to noise. By combining qubit count, gate fidelity, connectivity, and coherence into one figure of merit, Quantum Volume allows for a fair comparison across different quantum devices and architectures.

3

Application of Nuclear Structures

3.1 Overview of Our Proposed Work

In this section, we will briefly summarise our roadmap and project goals, including how the VQE will effectively estimate the ground-state energy based on the customized nuclear pairing model in 3.1.1, with our assumption to treat the proton only since the neutron will not affect the form factor from Ref.[10]. The Appendix A.9 will provide more details about the previous work with the Lipkin model.

The operator mapping details and the process to build the quantum circuits are in the 3.1.2, and we will also introduce some optimizers to finish the iterations for the VQE algorithm in 2.1.5 and 3.1.3.

3.1.1 Theoretical Framework of the Nuclear Shell Pairing Model

In many cases, the ground state energy of a nucleus cannot be solved precisely due to the complexity of the nuclear many-body system [57]. Quantum computing could have the potential to significantly enhance this model's efficacy by efficiently simulating complex many-body quantum systems, which are challenging for classical methods [10, 32]. This integration allows for more precise calculations of interaction cross-sections and detection rates, increasing the sensitivity and reliability of dark matter detection efforts [9]. The DM-Nuclei scattering can relate to the WIMP-Nuclei interaction, which can be calculated by quantum computing [10]. The basic idea is that WIMP will randomly hit (interact with) the nucleus with a tiny probability, but theoretically, it's always non-zero. The momentum and energy transfer will not change the nuclear shell structure and the ground state. It will affect charge density, which is the fundamental principle behind DM direct detection experiments. We introduce the nuclear shell pairing model, particularly for large atoms to address this. The nuclear shell pairing model is vital for dark matter detection as it accurately describes the nuclear targets used in experiments, thereby improving the predictions of nuclear responses to dark matter interaction [58].

Similar to how electrons are arranged in shells around an atom, nucleons (protons and neutrons) occupy discrete energy levels within the nucleus. As nucleons are added to the nucleus, they drop into the lowest-energy shells permitted by the Pauli Principle, requiring each nucleon to have a unique set of quantum numbers to describe its motion. The nuclei will be stable only when the

shell is fully occupied [59].

Within the framework of the nuclear shell model, nucleons occupy orbitals characterized by half-integer angular momentum eigenvalues, such as $j = \frac{1}{2}, \frac{3}{2}, \frac{5}{2}, \ldots$. These nucleons form pairs within their respective orbitals, specifically in even numbers. By keeping the number of neutrons constant, the primary focus is directed towards the proton orbitals. The total angular momentum is zero for simplicity, effectively coupling a state $|j, m\rangle$ with its corresponding $|j, -m\rangle$ state. Consequently, the creation and annihilation operators are given by:

$$\begin{aligned} \hat{S}_j^+ &= \sum_{m>0} (-1)^{(j-m)} a_{jm}^\dagger a_{j-m}^\dagger, \\ \hat{S}_j^- &= \sum_{m>0} (-1)^{(j-m)} a_{j-m} a_{jm} \end{aligned} \tag{3.1}$$

The pair creation operator $\hat{S}_j^+$ creates a pair of nucleons in the orbital j with projections m and $-m$, while the pair annihilation operator $\hat{S}_j^-$ annihilates a pair of nucleons from the same orbital. With the mutually SU(2) algebras $\left[\hat{S}_i^+, \hat{S}_j^-\right] = 2\delta_{ij}\hat{S}_j^0$, $\left[\hat{S}_i^0, \hat{S}_j^\pm\right] = \pm\delta_{ij}\hat{S}_j^\pm$.

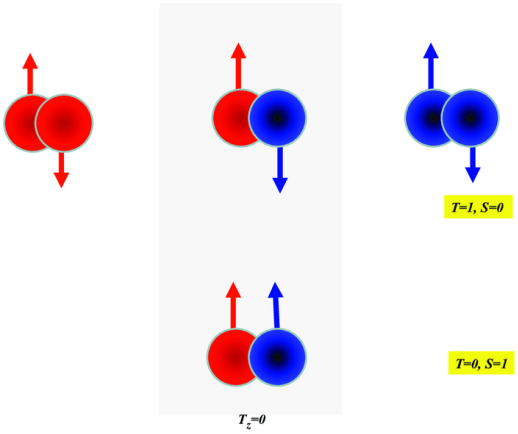

Figure 3.1: This image illustrates four different types of nucleon pairs, characterized by their spin (S) and isospin (T) properties for nuclei with the same number of protons and neutrons ($Z = N$) [60]. The left side with red colour is the Proton-Proton Pair, the Mixed Pair in the middle, and the Neutron-Neutron Pair on the right.

It is similar to the electron Spin Singlet State ($S = 0$), both protons or neutrons paired with opposite spins (left and right diagrams in Fig 3.1), resulting in zero total spins. Neutron-proton pairs in an isospin singlet state also exhibit this behaviour (middle top diagram). And for Spin Triplet State ($S = 1$), Neutron-proton pairs with parallel spins form a triplet state (bottom middle diagram), resulting in a total spin of one.

In our project, here's one thing that should be mentioned: we neglect the difference between the proton and neutron as they are equivalent [9, 10], the customized Nuclear Shell Pairing Hamiltonian of the nucleons interacting with a pairing force scale $|G|$ system is

$$\hat{H} = \sum_{jm} \epsilon_j a_{jm}^\dagger a_{jm} - |G| \sum_{jj'} c_{j,j'} \hat{S}_j^+ \hat{S}_{j'}^- \tag{3.2}$$

The $a_{jm}^\dagger a_{jm}$ can be regarded as the nucleon number operator $N = N_p + N_n$. Where the coefficient $\sum_j \sum_{j'} \left|c_{j,j'}\right|^2 = 1$. Since the operators, it's naturally adapt the representation of SU(2) algebras

as the same as the qubit form, it can be expanded into the sum of the following terms

$$\begin{aligned}\hat{H} = &\epsilon_{1/2} S^0_{1/2} + \epsilon_{3/2} S^0_{3/2} - c_{1/2,1/2} S^+_{1/2} S^-_{1/2} \\ &- c_{1/2,3/2} S^+_{1/2} S^-_{3/2} - c_{3/2,1/2} S^+_{3/2} S^-_{1/2} - c_{3/2,3/2} S^+_{3/2} S^-_{3/2}\end{aligned} \tag{3.3}$$

The VQE algorithm can be employed to estimate this Hamiltonian's ground state energy. The VQE algorithm optimizes a parameterized trial wave function to minimize the expected energy. The estimated energy, which depends on the variational parameters $\theta_1, \cdots, \theta_n$, is iteratively refined until it converges to its minimum value. This estimated energy is always greater than or equal to the ground state energy:

$$E(\theta_1, \cdots, \theta_n) = \langle \hat{H} \rangle \geq H_0 \tag{3.4}$$

The expectation value of the Hamiltonian is expressed as:

$$E(\theta_1, \cdots, \theta_n) = \sum_i \alpha_i \left\langle \psi(\theta_1, \cdots, \theta_n) \middle| \hat{P}_i \middle| \psi(\theta_1, \cdots, \theta_n) \right\rangle \tag{3.5}$$

Here, α_i are the coefficients corresponding to the Pauli operators $\hat{P}_i$, and $\psi(\theta_1, \cdots, \theta_n)$ is the parameterized trial wave function. The objective is to determine the set of parameters $\theta_1, \cdots, \theta_n$ that minimizes $E(\theta_1, \cdots, \theta_n)$, thereby providing an estimate of the ground state energy H_0.

3.1.2 Qubit Mapping and Circuit Design

An important step then is to map the physical observables in the modelled system to qubits observables, not only for the Hamiltonian but also for the approximate *ansatz*.

Based on the derivation of the nuclear pairing model, the Hamiltonian can be written as the form of the sum of Pauli products. Then the quantum estimator will evaluate the Hamiltonian that converts to the qubits' observable form, but an effective trial wavefunction is still needed.

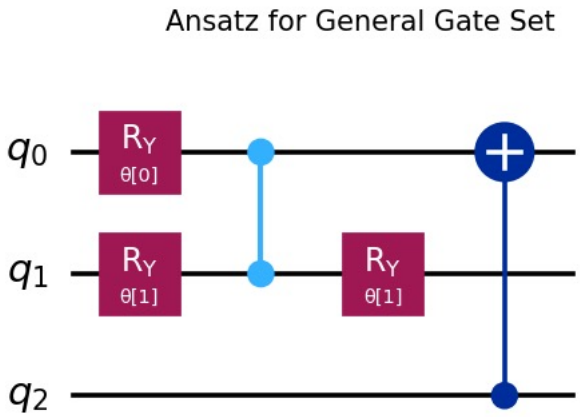

Figure 3.2: This figure shows the effective *ansataz* for two parameters case in a general gate set. The light blue multi-qubit gate is Controlled-Z gate that corresponds to Z operation on the desired qubit with the condition of control qubit. And extra CNOT gate will be used to create the entanglement between those qubits as a many-body system.

However, different quantum platforms have their own gate definition and universal gate set, so commonly, a general gate set will not truly and exactly be deployed into our algorithm. Only the

conventional gate will participate in the quantum operation. The IBM quantum platform has a basic gate set definition [12]. The figure below shows the converted version of the IBM basic gate set.

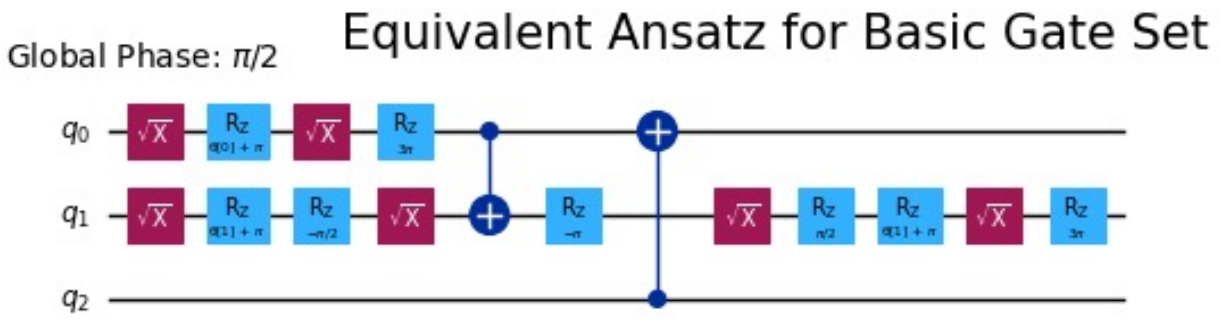

Figure 3.3: This figure shows the quantum circuit after the conversion. The CZ gate will be replaced by the combination of CNOT gate and R_Z gate.

With the different gate set definitions above in Fig.3.3 and Fig.3.2, the number of gates will also differ under the set transformation, even if the quantum operation unitary matrix is mathematically equal.

Depending on the type of qubit, unitary operations(gate or circuit) applied to the physics qubit can be done with a laser pulse or external dynamic field. For IBM Quantum Hardware, the pulse sequence defines all of the quantum gates [12]. An algorithm that incorporates excessive gates can substantially degrade its performance accuracy. This deterioration occurs as the increased gate count reduces the available dephasing time and amplifies the quantum errors introduced during computation. Once a job is submitted to the quantum platform, which must include an executable quantum circuit, it includes a combination of serval quantum gates.

3.1.3 Classical Optimizer and Quantum Iterations

In VQE, two primary components are crucial: the classical optimizer and quantum iterations. The classical optimizer's role in VQE is to find the optimal parameters for a quantum circuit that minimizes a cost function, which typically represents the expectation value of the Hamiltonian with respect to a specific quantum state. Here, we include a table showing the most commonly used optimizers we may deploy to our algorithm based on the benchmark.

Optimizer	Type	Description
Gradient Descent	Gradient-Based	Adjusts parameters iteratively in the direction of the negative gradient to minimize the cost function.
COBYLA (Constrained Optimization BY Linear Approximations)	Gradient-Free	A derivative-free method that handles constraints by linearly approximating the cost function within a region.
Nelder-Mead	Gradient-Free	A simplex-based method effective for optimizing non-smooth functions without requiring derivatives.
BFGS	Gradient-Based	Uses an iterative approach to approximate the Hessian matrix for efficient local minimum finding.
Simulated Annealing	Stochastic/Heuristic	Explores the solution space probabilistically, allowing occasional cost increases to escape local minima.
SLSQP (Sequential Least Squares Programming)	Gradient-Based	A gradient-based optimization method efficiently handles equality and inequality constraints using a sequential quadratic programming approach.
SPSA (Simultaneous Perturbation Stochastic Approximation)	Stochastic/Heuristic	An efficient optimization algorithm that approximates the gradient by perturbing all parameters simultaneously, making it suitable for noisy environments.

Table 3.1: Common Classical Optimizers used in VQE. This table categorizes several optimizers based on their types—gradient-based, gradient-free, and stochastic/heuristic—and briefly describes their key characteristics and use cases. Gradient-based optimizers, such as Gradient Descent and BFGS, rely on gradient information to navigate the cost landscape, while gradient-free methods like COBYLA and Nelder-Mead do not require derivatives and are useful for non-smooth or constrained optimization problems. Stochastic/heuristic methods, including Simulated Annealing and SPSA, are designed to handle noisy environments and escape local minima by probabilistically exploring the solution space. These optimizers are vital for tuning the parameters of quantum circuits in VQE, a hybrid quantum-classical algorithm for finding the ground state energy of quantum systems. [61]

With the optimizers above, we can create the corresponding cost function of the expected ground state energy of the nuclear pairing model. With the energy cost estimated, the parameters could be sent to iterate until the energy cost is attached the minimum. The Fig.3.4 below shows there are huge differences for various optimizers under a specific noise configuration.

The configurations above include COBYLA, L-BFGS-B, and SLSQP [62]. Each optimizer is evaluated under several scenarios: with depolarizing errors of 0.01, 0.05, and 0.1, and with a "GenericBackendV2." The Generic Backend will be created by the real noise data and fitting them into the noise model by IBM [12, 61].

The total evaluation process will be run on a real quantum backend offered by IBM Quantum. However, due to the limited run time and expensive cost of 1.6 USD/s, we had to test our algorithm locally before we submitted the job to IBM Cloud. In the previous section, we concluded the simulation method so that we could evaluate it locally on our PC according to the matrix operation,

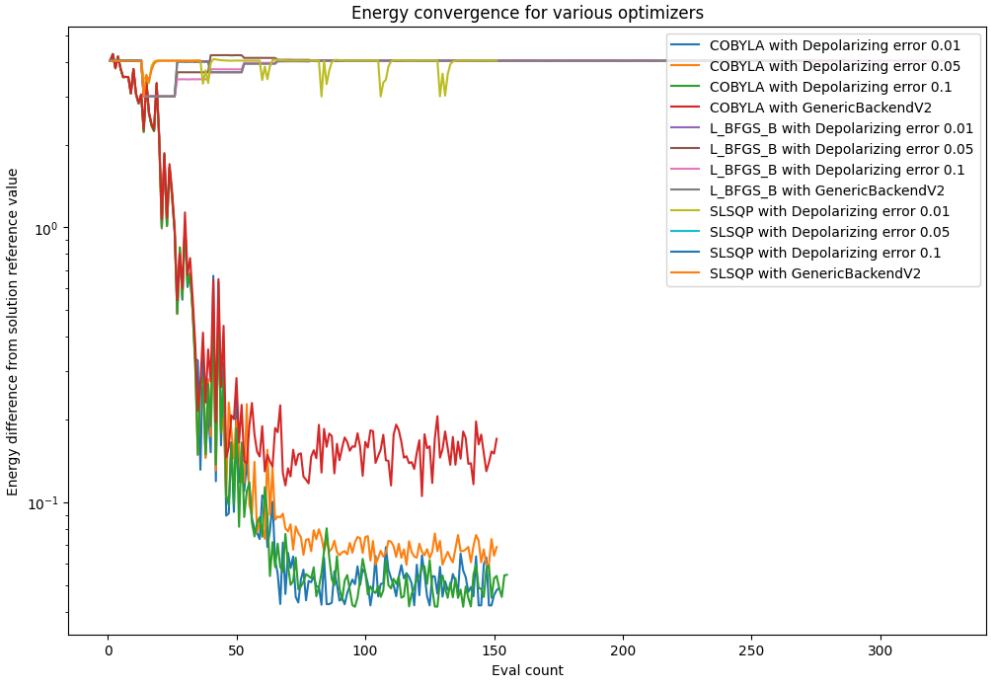

Figure 3.4: The figure illustrates the energy convergence for various optimization algorithms under different conditions. The y-axis represents the energy difference from the solution reference value, plotted on a logarithmic scale, while the x-axis indicates the evaluation count.

and the process could also enhanced through parallel computing via GPU [12].

The memory cost of local quantum simulations depends on the size of the simulated quantum system and the specific simulation method used. For simulating a quantum system with n qubits, if using a full state vector representation, the memory cost scales exponentially as 2^n complex numbers, requiring 16×2^n bytes (assuming each complex number uses 16 bytes for double-precision floating-point format). However, for local quantum simulations that leverage tensor network methods like Matrix Product States (MPS) A.8, the memory cost can be significantly reduced and scales as $O\left(nD^2\right)$, where D is the bond dimension that depends on the entanglement in the system [63]. In our program, most noisy simulations on local computers will be done with MPS methods if there are no strict restrictions on accuracy.

Number of Qubits (n)	**Memory Cost (MB)**	**Memory Cost (GB)**
2	0.00025	0.00000024
4	0.004	0.000004
8	1.024	0.001
16	67,108.864	65.536
32	288,230,376,151,711.744	268,435,456

Table 3.2: Memory cost for simulating quantum systems from 2^n qubits up to 32 qubits in complex128 format. The cost could be half if we convert the format into complex64, but it will lose accuracy.

The memory cost will depend on the simulation process itself, and the quantum circuit depth will also affect it [12] as shown in Fig.3.5.

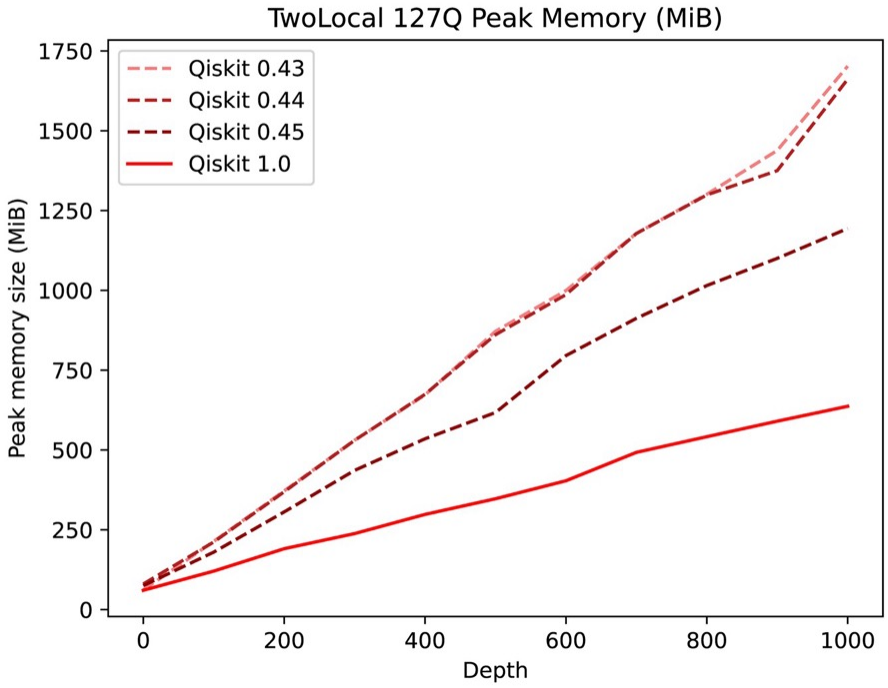

Figure 3.5: The figure illustrates the memory cost for the 127 Qubits devices; different software package versions will also influence it. The circuit depth or circuit layer will be in linear relation with the cost, so it is important to find an effective mapping and effective storage method [12].

So it is crucial to quantify the relation between the number of parameters used in *ansatz* and the multi-qubit depolarisation noise level corresponding to the estimated energy difference with reference energy. Those could help us build a more effective algorithm with fewer errors and performance cost, and the outcome could be within an acceptable range.

4 Results

The results presented in this chapter provide valuable insights into the effectiveness of various error mitigation techniques in enhancing the accuracy of the VQE algorithm under noisy conditions. By systematically analyzing the impact of measurement error mitigation, ZNE, and PEC methods (also with error suppression methods in the A.6), it becomes evident that each approach offers distinct benefits and limitations depending on the type and extent of noise present.

This section will expand upon these findings, considering each mitigation strategy's practical implications and theoretical significance in the context of near-term quantum devices. In particular, we will explore how the trade-offs between mitigation accuracy and computational overhead may influence the selection of techniques for specific applications. The results of the broader challenges of quantum error correction and the ongoing development of hybrid approaches that combine mitigation with early-stage error correction methods will also be discussed. Through this analysis, we aim to establish a clearer understanding of how these strategies can support the advancement of quantum algorithms in the NISQ era, while also identifying potential pathways for further research into optimizing quantum computation amidst hardware limitations.

4.1 Impact of Quantum Errors

The imperfections in quantum gates, especially prevalent in the NISQ era, pose significant challenges to the accuracy and reliability of quantum computations. These imperfections manifest as gate errors, decoherence, and measurement errors, collectively contributing to deviations from the ideal quantum behaviour we introduced in 2.2. In the context of the VQE algorithm, such errors can lead to discrepancies in the computed energy levels, potentially undermining the algorithm's ability to approximate the ground state energy of a given Hamiltonian accurately.

This section delves into how quantum gate imperfections impact the expectation values obtained from quantum measurements. We began from the characterization in 4.1.1. We systematically analysed how various types of errors—such as single-qubit gate errors, two-qubit gate errors, and readout errors—affect the convergence and accuracy of the VQE algorithm in 4.1.2. Additionally, we explore the cumulative effect and the accuracy of the number of parameters over multiple iterations of the algorithm in 4.1.3, highlighting the importance of error mitigation techniques.

Furthermore, we investigate the effectiveness of Quantum devices' quantum volume in 4.1.4,

noting that this metric reflects their capability to run complex algorithms. The temporal variability of quantum errors introduces additional complexity. By examining these metrics, we aim to provide a comprehensive understanding of the impact of quantum errors on algorithmic performance, laying the groundwork for strategies to enhance the robustness of nucleus simulation on near-term quantum computers.

4.1.1 Error Characterization

Accurate characterization of qubit performance and error rates is crucial for designing efficient quantum circuits and implementing effective error mitigation strategies [64]. The table below presents the average values of these parameters for the `ibm_brisbane` quantum system. The relaxation time (T_1) of the qubits is measured to be 228.87 μs, indicating the average time a qubit remains in its excited state before decaying to the ground state. The dephasing time (T_2) is 144.28 μs, representing the timescale over which a qubit preserves its phase coherence, considering both energy relaxation and dephasing from environmental interactions. The qubit frequency is approximately 4.906 GHz, which affects the qubit's operational speed and interaction with control pulses. The Error Per Logical Gate (EPLG) is reported as 1.98%, providing an estimate of the average error rate per single-qubit gate operation.

ibm_brisbane	
Parameter	**Average**
$T_1(\mu s)$	228.87
$T_2(\mu s)$	144.28
Qubit frequency (GHz)	4.906
EPLG	$1.98e{-2}$
Pauli-X gate error	$2.287e{-4}$
ECR gate error	$8.082e{-3}$
Readout error $P(0 \mid 1)$	0.0152
Readout error $P(1 \mid 0)$	0.0136

Table 4.1: Average performance parameters and error rates for the IBM Quantum System `ibm_brisbane`, including coherence times (T_1 and T_2), qubit frequency, gate errors, and readout errors.

As previously discussed, precise characterization of qubit performance and error rates is essential for designing efficient quantum circuits and selecting suitable error mitigation strategies. For our implementation, we will prioritize mapping to the qubits exhibiting the best performance, given that not all qubits on the device will be utilized. These performance parameters serve as the foundation for our subsequent benchmarking tests, where we systematically assess the behaviour of quantum algorithms under realistic operational conditions. Moreover, it is essential to note that error rates are not static; they fluctuate over time and tend to increase due to cumulative temporal effects.

We chose the following qubits layout in Tab.4.2 with the best performance for the transformation and compilation process for the two parameters case.

With the characterization above, we can map the *ansatz* to the physical quantum gate sequence with the best entanglement performance and lowest error rate.

Physical Qubit	Ansatz Qubit	Classical Register
19	0	0
20	1	1
21	2	2

Table 4.2: Mapping of *ansatz* logical qubits to physical qubits on the quantum device. Due to low qubits usage, all logical qubits are directly connected; there are no ancillary qubits to facilitate the necessary swaps to establish connectivity.

4.1.2 Impact of Gate Fidelity on Energy Estimation Accuracy

In the presence of noise, the results obtained from quantum computations deviate from those of an ideal, noiseless system. It is therefore crucial to define an acceptable tolerance for these deviations, particularly in relation to the energy expectation value. For our analysis of the simplest nuclear pairing model, the target pairing energy estimate is set at -0.48072, and we establish a tolerance threshold of 1×10^{-2}. This threshold ensures that the noise-induced discrepancies in the energy estimation remain within a range considered practically acceptable for our application.

To thoroughly investigate the impact of gate fidelity on energy estimation accuracy, we incorporate a noise model into our simulations. This noise model is designed to replicate the errors typically encountered in real quantum hardware, such as gate errors, decoherence, and measurement noise. By simulating these noise effects, we can better understand how they influence the performance of the VQE algorithm, particularly in terms of energy estimation accuracy. The noisy simulation allows us to systematically explore the relationship between gate fidelity and the resulting energy deviations, enabling the identification of critical thresholds beyond which the accuracy of the energy estimate becomes unacceptable.

The quantum noise can be described by the quantum channel, we have demonstrate a general form of it in the Appendix.A.3. Nowadays on the NISQ devices, the dominant noisy channel will be a depolarizing channel on both single-qubit and multi-qubit gates, which can be represented by:

$$\mathcal{E}(\rho) = (1-p)\rho + \frac{p}{d}I \tag{4.1}$$

where p is the depolarizing error rate, d is the dimension of the Hilbert space ($d = 2$ for a single qubit), and I is the identity matrix.

The fidelity F of a quantum gate under depolarizing noise is defined as:

$$F = \int d\psi \, \langle\psi|\mathcal{E}(|\psi\rangle\langle\psi|)|\psi\rangle \tag{4.2}$$

$$F = (1-p)\int d\psi \langle\psi \mid \psi\rangle + \frac{p}{d}\int d\psi \langle\psi|I|\psi\rangle \tag{4.3}$$

Substituting the noise model:

$$\mathcal{E}(\rho) = \begin{bmatrix} \left(1-\frac{2p}{3}\right)a + \frac{2p}{3}d & \left(1-\frac{4p}{3}\right)b \\ \left(1-\frac{4p}{3}\right)b^* & \left(1-\frac{2p}{3}\right)d + \frac{2p}{3}a \end{bmatrix} \tag{4.4}$$

$$F = (1-p) + \frac{p}{d}\cdot d \tag{4.5}$$

For a single qubit ($d = 2$):

$$F = 1 - \frac{3}{4}p \tag{4.6}$$

In general the depolarizing channel for a two-qubit gate, like the ECR gate, could be calculated using the same method (with $d = 4$). With the formula given above, we can set up the depolarizing error for the noise model and find out how to get the estimated energy in the acceptable range. However, in our case the measurement error is also ineligible. For a single qubit, the measurement error can be represented by a 2×2 probability matrix:

$$M = \begin{pmatrix} 1 - P(1 \mid 0) & P(1 \mid 0) \\ P(0 \mid 1) & 1 - P(0 \mid 1) \end{pmatrix} \tag{4.7}$$

Where the $P(0 \mid 1)$ is the probability of measuring $|0\rangle$ when the actual state is $|1\rangle$, and $P(1 \mid 0)$ is the probability of measuring $|1\rangle$ when the actual state is $|0\rangle$. With this matrix, we can easily recover the bias from our measurement outcome.

In Figure 4.3, we explore the influence of gate fidelity on VQE performance by examining how the energy difference from the reference value varies under different fidelities. This plot illustrates VQE runs with various trail wavefunction configurations (custom *ansatz*, RYRZ+CNOT *ansatz*, EfficientSU2, and EfficientSU2 with two repeats) under single-qubit and two-qubit gate noise conditions.

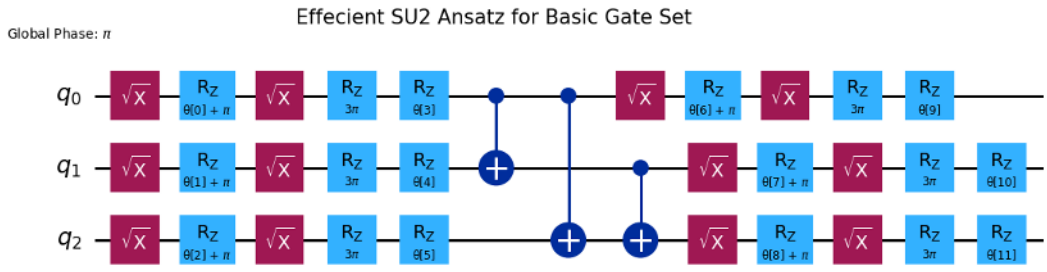

Figure 4.1: This is the most commonly used HEA *ansatz*, which uses linear connection by CNOT gate to create the entanglement states for the system of total qubits. Due to the multi-layer of a single rotation gate, the output can precisely vary when we change the variational parameters. However, this form will cost more for the number of gates and number of parameters in use with longer runtime and iteration on QPU.

Refer to the traditional HEA *ansatz* above, here is a new type of HEA *ansatz* for the RYRZ+CNOT *ansatz* created by us.

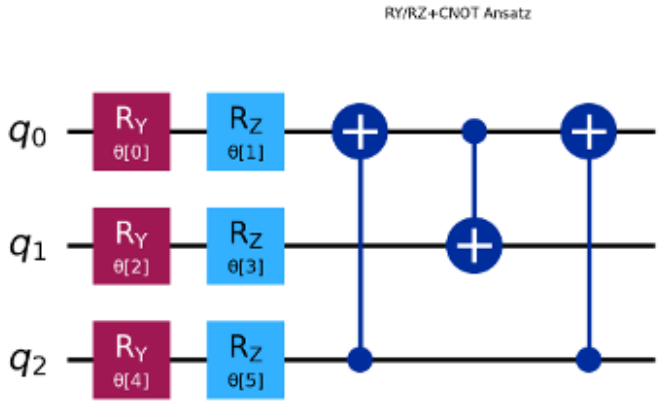

Figure 4.2: This types *ansatz* include the R_Y gate, which could represent the complex trail wavefunction naturally, with a reverse linear connection for three qubits. The total gate cost will between our customized *ansatz* and the IBM Efficient SU2 *ansatz*.

In our attempt for the VQE performance, we sweep the gate fidelity on all of those *ansatz* versus the output energy difference. Note that the peaks occur because sometimes the error is large, and the optimizer cannot iterate to the correct value and stop.

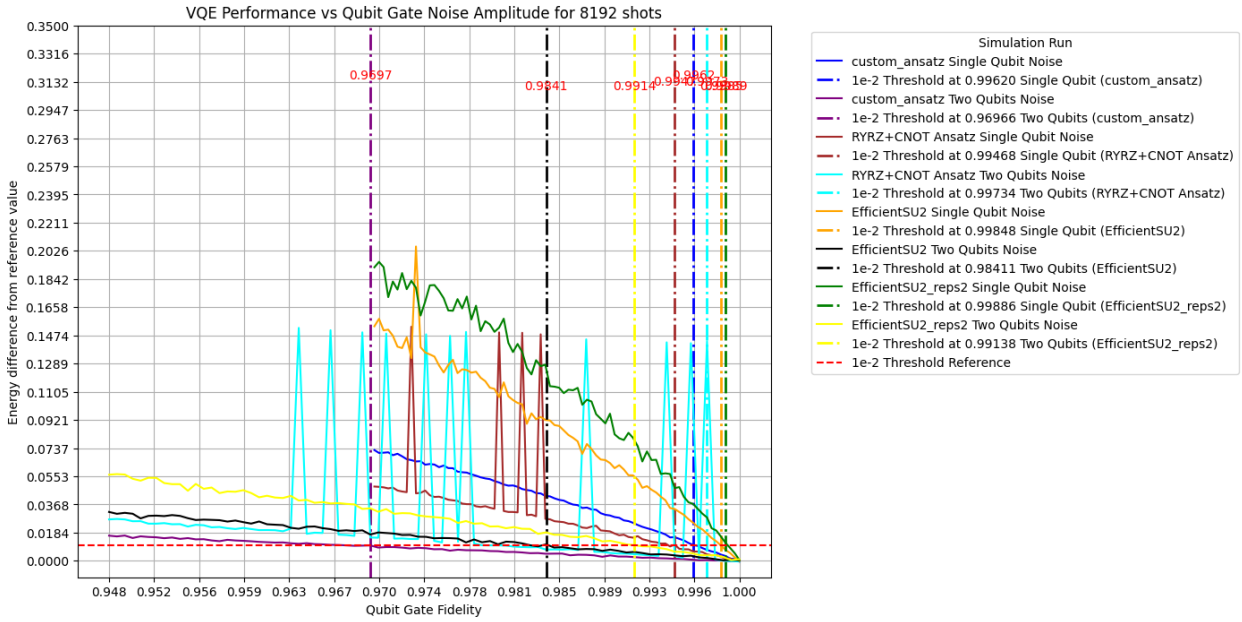

Figure 4.3: VQE performance as a function of qubit gate fidelity for 8192 shots. The plot shows the energy difference from the reference value across various simulation runs, including different ansatz configurations (custom_ansatz, RYRZ+CNOT Ansatz, EfficientSU2, and EfficientSU2_reps2) under single and two-qubit noise conditions. Vertical dashed lines indicate the points at which the energy difference exceeds the set threshold of 1×10^{-2}, highlighting the impact of noise on the accuracy of the energy estimation. The red dashed line marks the 1×10^{-2} threshold reference for energy difference.

It demonstrates how qubit gate fidelity affects VQE performance, specifically by examining the energy difference from a reference value across multiple *ansatz* configurations under single- and two-qubit noise conditions. As gate fidelity decreases, the energy difference typically increases,

reflecting the impact of noise on computation accuracy. The custom *ansatz* configuration reaches the 2e-2 accuracy threshold at relatively high fidelities (0.9962 for single-qubit noise and 0.9697 for two-qubit noise), indicating a sensitivity to noise. The RYRZ+CNOT **Ansatz** performs somewhat better, achieving the threshold at slightly lower fidelities (0.9946 for single-qubit noise and 0.9734 for two-qubit noise). The EfficientSU2 *ansatz* further improves on this, maintaining accuracy down to fidelities of 0.9984 for single-qubit noise and 0.9841 for two-qubit noise, showing enhanced robustness in comparison. Among the tested configurations, EfficientSU2 with two repeats is the most resilient, crossing the threshold only at 0.9986 for single-qubit noise and 0.9914 for two-qubit noise.

In conclusion, the findings underscore the varying robustness of VQE *ansatz* designs to noise; traditional HEA *ansatz* does not demonstrate superior tolerance to reduced fidelity. This suggests that certain *ansatz* configurations, such as our custom *ansatz*, are better suited for implementation on NISQ devices, where gate fidelities are often constrained. Identifying specific fidelity thresholds provides a practical guideline for selecting an appropriate ansatz based on hardware fidelity, balancing the demands for computational accuracy and noise resilience in quantum applications.

4.1.3 Effect of Iteration Parameter and Gate Count

It is hypothesized that energy discrepancies may increase with more parameters in the *ansatz*. To explore this, we developed the standard HEA and customized efficient ansatz based on $R_Y + R_Z$ gate, with fewer single-qubit gates.

During our investigation, we observed a significant increase in quantum errors as the system's complexity escalated. This observation underscores the critical need for thorough characterization and quantification of these errors, as they directly impact the accuracy of estimated ground-state energy and the convergence behaviour of iterative algorithms. To address this, we have conducted a series of experiments that vary the number of parameters in the ansatz. In parallel, we examined the correlation between estimated energy and the fidelity of CNOT and ECR gates, given their prominent role in contributing to quantum errors within NISQ devices.

Feature	IBM Heron R2	IBM Eagle R3
Number of Qubits	156	127
Architecture	Heavy-hexagonal lattice	Heavy-hexagonal lattice
Qubit Technology	Fixed-frequency qubits with tunable couplers	Fixed-frequency qubits with fixed couplers
Gate Fidelity	Improved gate fidelities with Error per Layer Gate (EPLG) of 0.4%	Enhanced coherence properties leading to lower gate errors
Signal Delivery	Utilizes high-density flex cabling for fast, high-fidelity control	Advanced semiconductor signal delivery and packaging technologies
Quantum Volume	512	128
Basic Gate Set	$\{CZ, ID, RZ, SX, X\}$	$\{ECR, ID, RZ, SX, X\}$

Table 4.3: Comparison between IBM Heron R2 and Eagle R3 quantum processors.

Generally, the Heron R2 include 156 qubits, tunable couplers, and a quantum volume of 512, is optimized for complex computations requiring high gate fidelity and flexible interactions. Eagle R3, with 127 qubits and fixed couplers, emphasizes coherence stability, benefiting applications requiring extended qubit state duration despite a lower quantum volume of 128. Both share a heavy-hexagonal lattice architecture, supporting connectivity and reduced cross-talk. While Heron R2 uses high-density flex cabling for rapid signal control, Eagle R3 leverages advanced semiconductor signal technologies. Their shared gate set, $\{X, SX, R_Z, ID\}$, allows for versatile quantum operations. Together, these processors reflect IBM's advancements in fidelity, scalability, and coherence management.

To better display the relation between the number of gates and the number of parameters (DOF) on the different generations of quantum devices, we have created a statistic figure below to show the number of different types of gates on Heron and Eagle devices.

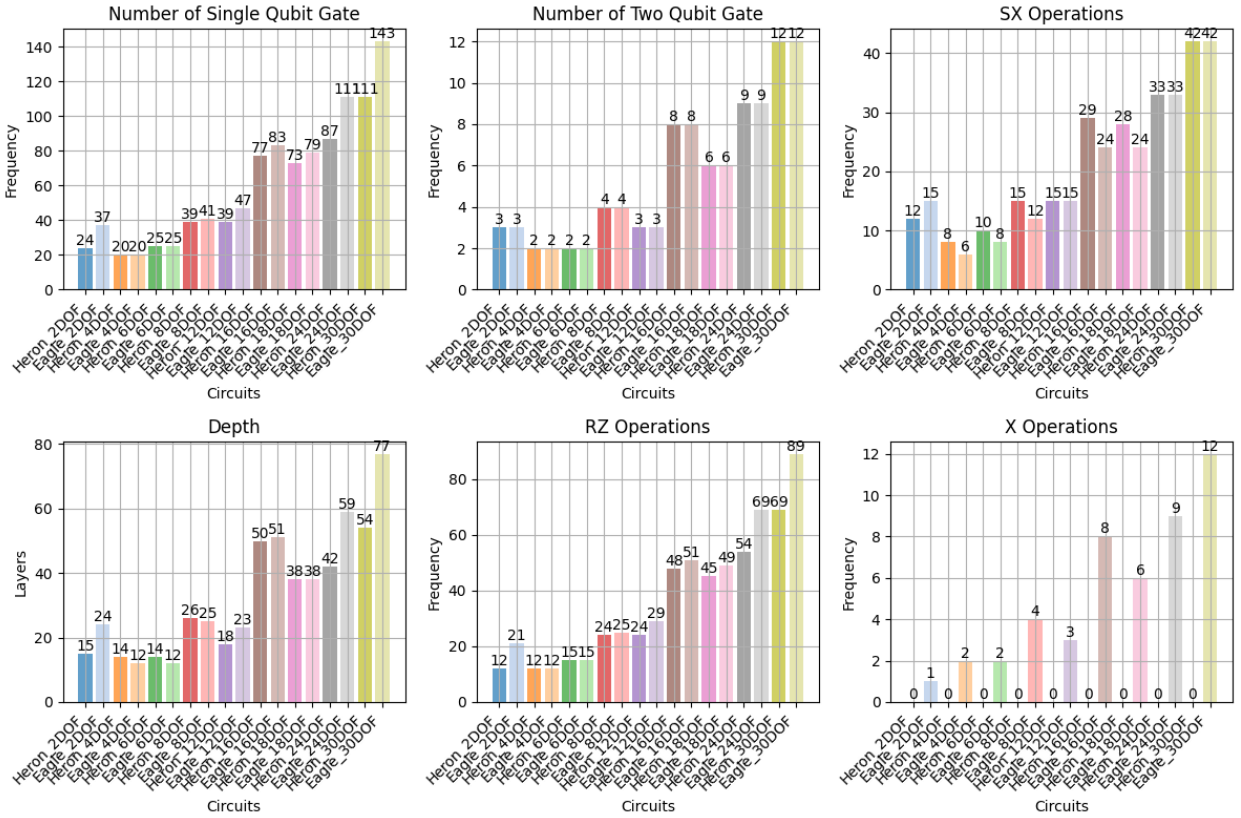

Figure 4.4: Working in Progress

Note that the relation between the number of variational parameters and the number of single/multi-qubit gates is not a linear relation due to different types of *ansatz*, and the gate cost may be significantly different on two platforms. The Depth is corresponding to the actual quantum gate layers on the specific devices, a deeper circuit will cause larger time cost due to more basic operations, which may also lead to extra error by additional gates.

A comprehensive presentation of the results, illustrating the impact of both parameter count and gate fidelity on system performance, is provided in Fig.4.5.

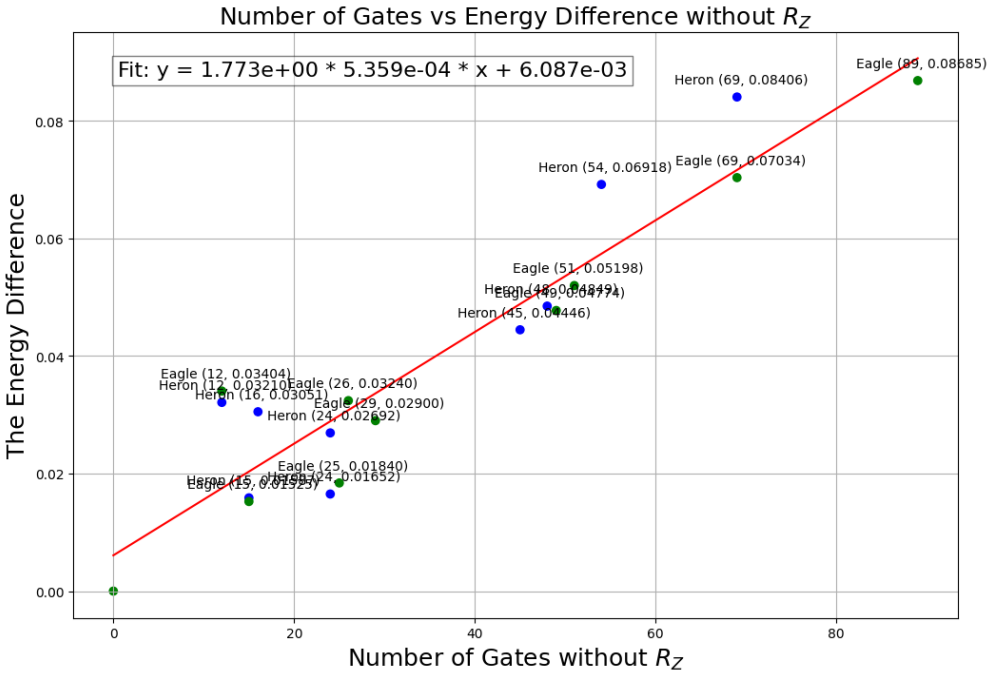

Figure 4.5: This figure illustrates the linear dependence of the gate cost, excluding the R_Z operation, versus the estimated energy difference. The R_Z operation is omitted because it is a purely software-based operation on the IBM Q platform, introducing no error. Detailed values are displayed in the brackets. To reach the minimum energy difference, we set the optimal point as the input for the quantum estimator, replacing the need for VQE iterations.

In summary, this finding shows that the energy difference is not directly relevant to the number of variational parameters in the *ansatz*, but a linear relation to the number of gates instead.

4.1.4 Is the Quantum Volume a Good Metric?

The need to verify Quantum Volumes' validity arises from the inherent complexity of quantum systems. Different quantum tasks—such as optimization, simulation, and cryptography—place varying demands on the hardware. A metric that works well for one type of quantum workload might not necessarily be suitable for another. By scrutinizing QV, we aim to ensure that it accurately reflects the quantum computer's ability to perform meaningful and diverse tasks rather than just being an abstract or overly generalized measure, especially compared to fidelity.

In Figures 4.6 and 4.7, we explore the relationship between QV and the accuracy of energy estimations in quantum simulations. The plots illustrate how increasing QV correlates with improved energy estimation, as lower estimated energies generally indicate a better approximation of the ground state energy in quantum systems. This suggests that higher QV systems can handle more complex quantum states and deeper circuits, which are crucial for accurate quantum simulations. Both figures illustrate how increased quantum volume, generally achieved through a combination of higher qubit counts and circuit depth, correlates with decreased estimated energy, suggesting that higher quantum volume (ranging from 8 to 256) leads to more accurate energy estimations.

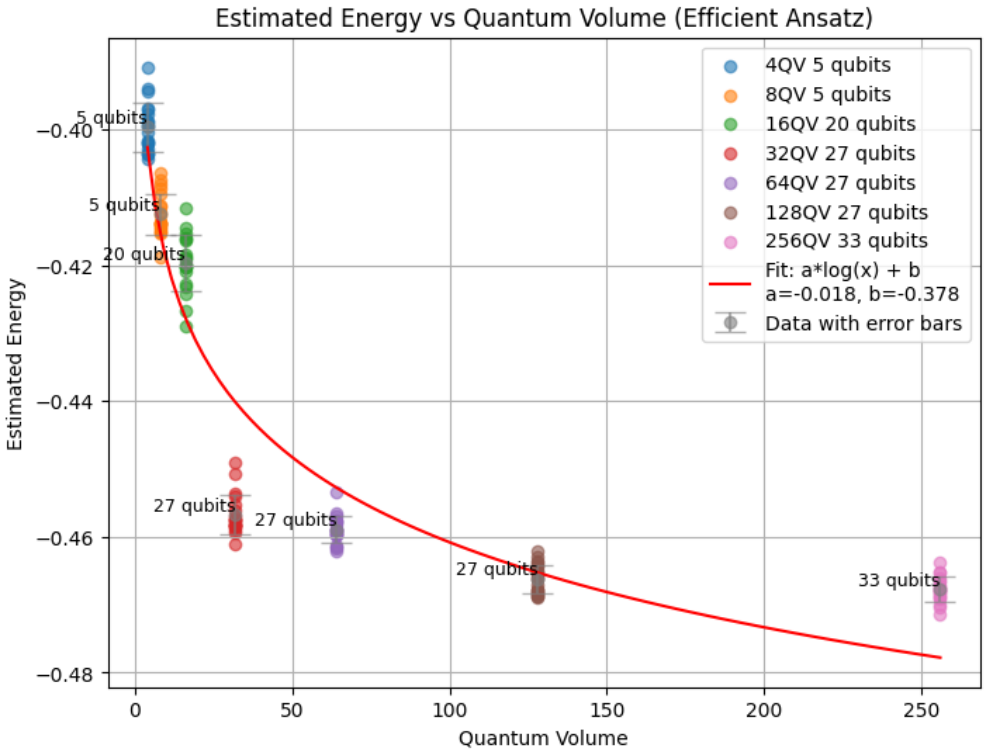

Figure 4.6: Plot of Estimated Energy versus Quantum Volume for different qubit counts using an Efficient Ansatz. Data points correspond to various QV values with qubit counts ranging from 5 to 33, indicated by color-coded markers. The fitted curve follows the function $f(x) = a.\ \log(x)+b$, with parameters $a = -0.018$ and $b = -0.379$, shown as a red line. Error bars represent the uncertainty in estimated energy measurements, illustrating how increased quantum volume generally leads to a lower estimated energy.

In Fig.4.6, the fitted curve follows the function $f(x) = alog(x) + b$ with parameters $a = 0.018$ and $b = 0.379$. This plot shows a moderate decrease in energy as quantum volume increases, with data points clustered around qubit counts of $5, 20$, and 27 and a slight levelling off of the energy reduction at higher volumes.

Figure 4.7 shows a similar plot but with the Efficient SU2 *ansatz* and reverse linear CNOT connectivity, where the fitted curve has parameters $a = 0.022$ and $b = 0.353$. In this case, the steeper slope ($a = 0.022$) suggests a stronger correlation between quantum volume and estimated energy reduction. This ansatz achieves a slightly lower estimated energy overall, indicating that the SU2 structure with reverse CNOT connectivity may be more effective in reducing energy than the generic Efficient Ansatz.

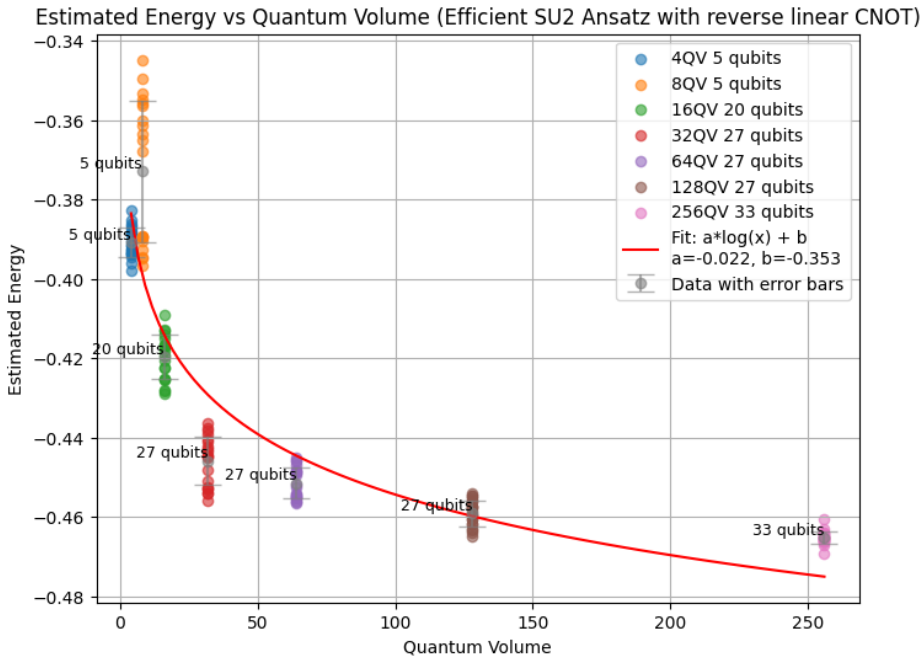

Figure 4.7: Plot of Estimated Energy versus Quantum Volume using an Efficient $SU2$ *ansatz* with reverse linear CNOT connectivity. Data points represent various QV values for qubit counts ranging from 5 to 33, identified by different colors. The fitted curve follows the function $f(x) = a \cdot \log(x) + b$, with parameters $a = -0.022$ and $b = -0.353$, depicted as a red line. The plot demonstrates a general decrease in estimated energy with increasing quantum volume, highlighting the impact of circuit depth and qubit count on energy estimation accuracy.

Comparatively, our custom *ansatz* yields lower energy estimates at similar quantum volumes, suggesting it may be more effective for energy accuracy than the traditional HEA Effcient SU(2) *ansatz*, potentially due to better entanglement and expressiveness provided by the reverse linear CNOT connectivity. This analysis highlights that the choice of *ansatz* structure and connectivity can significantly impact the efficiency and accuracy of energy estimation in quantum algorithms, with more structured approaches (like our customized effective *ansatz*) potentially outperforming simpler *ansatz* designs in practical implementations.

However, according to the comparison, the energy difference going down is more likely relevant to the gate fidelity, especially for the multi-qubit gates. Quantum Volume increased in the new generation of devices due to more qubits in the processor. So in our case, gate fidelity might be a better metric with linear fit than the Quantum Volume.

4.2 Techniques for Error Suppression

This section focuses on various techniques for error suppression in quantum computing, not only in the QISKIT library. It begins with a discussion on measurement prediction for a three-qubit system incorporating error mitigation strategies, emphasizing the practical applications of error reduction in 4.2.1. In 4.2.2, we explore new error mitigation approaches, providing a method to counteract the effects of noise and operational inaccuracies in quantum systems by a quadratic form cancellation on the measured expectation value. The section further delves into second-order perturbation theory applied to Hamiltonians under noisy conditions, offering insights into how theoretical models can account for and predict the impact of noise in 4.2.3. Note that the second-order perturbation

theory will also have the quadratic form in the expression. However, it formulates the errors in the ansatz and state preparation by the perturbative gate Hamiltonian; it's different from the quadratic form on the measurement expectation value. Finally, we conclude with benchmarking and outline potential future research directions to improve quantum computations' robustness and accuracy in 4.2.4.

Fig.4.8 shows the noiseless sweeping for the two parameters in our nuclear pairing custom *ansatz*.

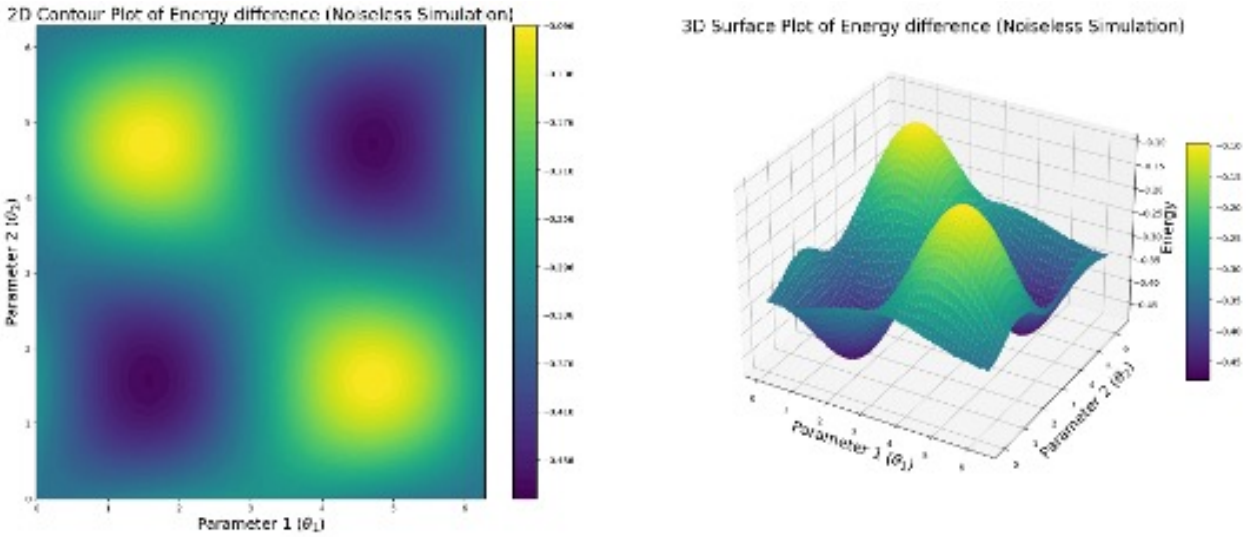

Figure 4.8: Illustration of results in the noiseless iteration case, each figure has 200*200 sites and runs with 8192 shots; the noise model only has depolarising errors on single-qubit and multi-qubit gates. The upper left figure shows the estimated energy for the paring Hamiltonian, taking the parameters from 0 to 2pi, and the right plot is in 3D viewing.

Results from noisy simulators are quite different from those from the noiseless case; it even demonstrates that the estimated energy could be lower than the classical prediction at some point. To justify this, we have created a noise model to adapt the noise features in Tab.2.2, which could give us a more realistic result close to the actual quantum backend.

Fig.4.9 shows the energy difference for the noisy and noiseless case, $\delta E = E_{noisy} - E_{noiseless}$.

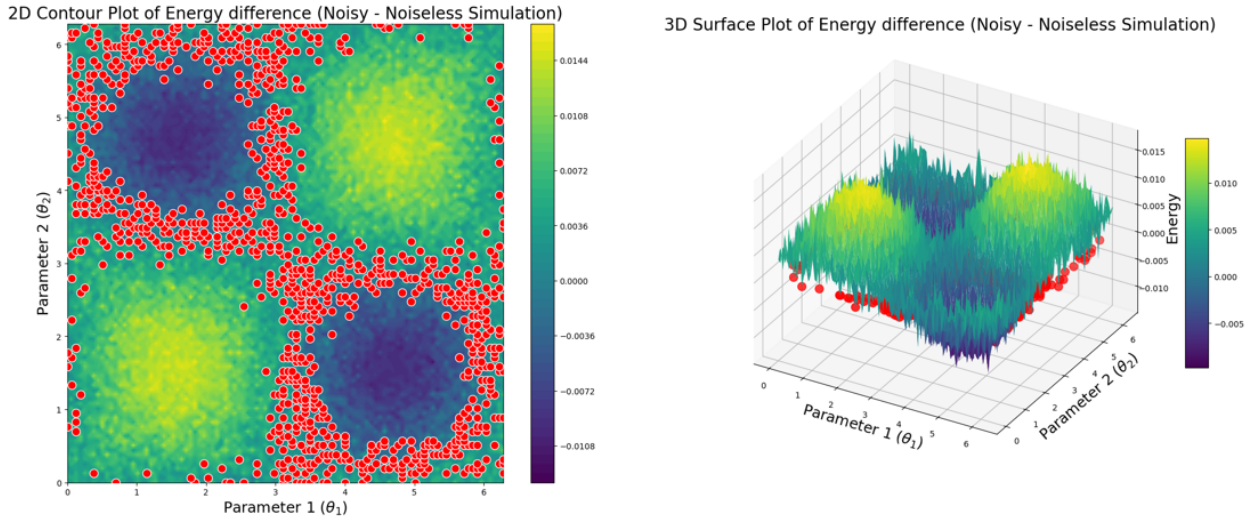

Figure 4.9: Comparison of energy difference between noisy and noiseless simulations. The left panel shows a 2D contour plot of the energy difference as a function of parameters θ_1 and θ_2, with red markers indicating zero value points (results are the same) under a $1e-3$ tolerance. The right panel displays a 3D surface plot of the same energy difference, providing a detailed view of the variation across the parameter space.

We can find the minimum point with a minus sign $(1.56, 4.70)$ of Fig.4.9 corresponds to the maximum point in the previous noiseless result Fig.4.8. The maximum energy difference point with a positive $(1.56, 1.56)$ corresponds to the minimum in the noiseless result. If there is no error on the energy difference, the $3D$ View above should be a plane on the x-y axis with $z = 0$.

Then, there is a problem we must overcome: How can we decrease the energy difference and make the result more accurate?

To address this, we have to test the error mitigation strategies offered by QISKIT and present our ideas based on the noisy data as in the subsections below.

4.2.1 Measurement Prediction for Three-Qubit Case with Error Mitigation

The errors will not only occur during the state preparation but also during the measurement each time. So, the first step is to understand how the incorrect readout affects the result and what the model is to describe this phenomenon.

In our VQE algorithm, several sources contribute to measurement errors:

- **State Discrimination Errors**: Misclassification of $|0\rangle$ as $|1\rangle$ and vice versa, direct cause of bit-flip errors.
- **Cross-talk**: Measurement of one qubit affects neighbouring qubits.
- **Decoherence during Readout**: Loss of coherence during the measurement process.

Since there are only 0 and 1 outcomes for Qubits measurement, no matter which basis we choose, due to the binary orthonormal configuration similar to the classical bits, an error can occur due to incorrect state readout and be stored by switching them in the classical register, which means storing 0 for an actual 1 state; we call it bit-flip classically.

In the later attempt, we derive the measurement prediction for a three-qubit system subject to bit-flip errors during measurement. Assume that each qubit can undergo a bit-flip error with certain probabilities due to imperfect measurement. For qubit q, let $p_{0,q}$ denote the probability of

a bit-flip from $0 \to 1$, and $p_{1,q}$ denote the probability of a bit-flip from $1 \to 0$. The total bit-flip probability for each qubit is therefore defined as:

$$p_q = p_{0,q} + p_{1,q}. \tag{4.8}$$

The goal is to compute the expectation value of a noisy measurement of the operators $Z_1 \otimes Z_2 \otimes Z_3$ in the presence of these bit-flip errors.

For a single qubit measurement, the bit-flip corrected expectation value of any operators Z under bit-flip errors is given by:

$$E(\tilde{Z}) = (1 - p_0 - p_1)Z + (p_1 - p_0)I, \tag{4.9}$$

where $\tilde{Z}$ represents the noisy measurement of Z. When calculating the expectation value, the term proportional to I cancels out (since it contributes a constant factor), leaving only:

$$E(\tilde{Z}) = (1 - 2p)Z, \tag{4.10}$$

where $p = p_0 + p_1$ is the total bit-flip probability.

For Q qubits, the expectation value of the tensor product $Z_1 \otimes Z_2 \otimes \cdots \otimes Z_Q$ under independent bit-flip errors on each qubit can be written as:

$$E\left(\tilde{Z}_1 \otimes \tilde{Z}_2 \otimes \cdots \otimes \tilde{Z}_Q\right) = \prod_{q=1}^{Q} (1 - 2p_q)\, Z_1 \otimes Z_2 \otimes \cdots \otimes Z_Q. \tag{4.11}$$

This expression uses the fact that each qubit's measurement error contributes independently to the overall expectation value [65].

For our case there are three qubits in use for the shell pairing model, where we measure the operator $Z_1 \otimes Z_2 \otimes Z_3$, the expectation of the noisy measurement $E(\tilde{Z}_1 \otimes \tilde{Z}_2 \otimes \tilde{Z}_3)$ can be expanded as:

$$E\left(\tilde{Z}_1 \otimes \tilde{Z}_2 \otimes \tilde{Z}_3\right) = (1 - 2p_1)(1 - 2p_2)(1 - 2p_3)Z_1 \otimes Z_2 \otimes Z_3. \tag{4.12}$$

To better understand the correction factor, we expand the product $(1 - 2p_1)(1 - 2p_2)(1 - 2p_3)$ as follows:

$$(1 - 2p_1)(1 - 2p_2)(1 - 2p_3) = 1 - 2(p_1 + p_2 + p_3) + 4(p_1p_2 + p_2p_3 + p_1p_3) - 8p_1p_2p_3. \tag{4.13}$$

This expression represents the total correction factor for the three-qubit measurement, accounting for all possible combinations of single, double, and triple-bit flips. In the special case where we can assume each qubit has the same bit-flip probability p (i.e., $p = p_1 = p_2 = p_3$), the correction factor simplifies significantly. Substituting $p_1 = p_2 = p_3 = p$ into the expression, we get:

$$(1 - 2p)^3 = 1 - 2(3p) + 4(3p^2) - 8p^3 \tag{4.14}$$

$$= 1 - 6p + 12p^2 - 8p^3 \tag{4.15}$$

We can neglect the cubic term $8p^3$ in the recent near-term quantum devices since the value tends to zero. Thus, the correction factor when all qubits have the same bit-flip probability p is:

$$f(p) = 12p^2 - 6p + 1 \tag{4.16}$$

Therefore, the corrected expectation value for the noisy measurement of $Z_1 \otimes Z_2 \otimes Z_3$ is given by:

$$E\left(\tilde{Z}_1 \otimes \tilde{Z}_2 \otimes \tilde{Z}_3\right) = f(p) \cdot Z_1 \otimes Z_2 \otimes Z_3, \tag{4.17}$$

where

$$f(p) = 12p^2 - 6p + 1 \tag{4.18}$$

This correction factor $f(p)$ can be applied to the raw measurement outcomes to mitigate the effect of measurement errors, yielding a more accurate estimate of the actual expectation value. With the expression above, we can design our mitigation by cancelling these factors.

So the noisy expectation value $E_{measured}$ could be represented when the p is not large:

$$E_{measured} = Ef(p) = E(12p^2 - 6p + 1) \tag{4.19}$$

4.2.2 Error Mitigation Approaches

Consider a general adding form, the error mitigation approach assumes that the measured expectation value, $\mathrm{Ex}_{\mathrm{measured}}$, can be decomposed into the true expectation value, $\mathrm{Ex}_{\mathrm{real}}$, and an error term, $P(\mathrm{Ex}_{\mathrm{real}})$. This assumption is formalized as:

$$\mathrm{E}_{\mathrm{measured}} = \mathrm{E}_{\mathrm{real}} + P(\mathrm{E}_{\mathrm{real}}) \tag{4.20}$$

The correction term, $P(E)$, is hypothesized to have specific properties:

1. $P(E)$ should be nearly zero when E is near zero, where only quantum fluctuations occur.
2. $P(E)$ should reach its maximum absolute magnitude near $x = \pm 1$, which corresponds to the extreme values of $\mathrm{E}_{\mathrm{real}}$.

Given these considerations, the form of $P(E)$ is proposed to be quadratic:

$$P(E) = aE^2 + bE + c, \quad \text{where } E \in [-1, 1] \tag{4.21}$$

Here, a, b, and c are parameters to be determined based on the noise characteristics in the quantum device.

If the error term $P(\mathrm{E}_{\mathrm{real}})$ is assumed to be small, the corrected expectation value can be approximated by subtracting the error from the measured value:

$$\mathrm{E}_{\mathrm{corrected}} \approx \mathrm{E}_{\mathrm{measured}} - P(\mathrm{E}_{\mathrm{measured}}) \tag{4.22}$$

This approximation provides a more accurate estimation of the actual expectation value by accounting for noise-induced errors. So, in the following steps we need to finish getting the coefficients for the parameters in quadratic form.

4.2.3 Perturbation Theory for the Hamiltonian with Noise

However, we need to clarify something before we get any coefficients in the correction factor; the quadratic factor correction is not unique to the measurement process; it will also be involved in the perturbation theory of qubit Hamiltonian.

Like basic time-independent perturbation theory, the total noisy Hamiltonian of the system can be expressed as:

$$H = H_0 + \lambda V \tag{4.23}$$

where H_0 is the noiseless Hamiltonian, λ is a small parameter representing the noise strength, and V is the perturbative noise operator. The noisy energy expectation value can be expanded up to the second order in λ, neglecting higher-order terms:

$$E(\lambda) \approx E_0 + \lambda\langle\psi_0|V|\psi_0\rangle - \lambda^2 \sum_{n\neq 0} \frac{|\langle\psi_n|V|\psi_0\rangle|^2}{E_n - E_0} \tag{4.24}$$

Here, E_0 represents the ground state energy of the noiseless Hamiltonian, and $|\psi_0\rangle$ is the corresponding ground state wavefunction. The difference between the noisy and noiseless energies, ΔE, can be expressed as:

$$\Delta E = E(\lambda) - E_0 \approx \lambda \langle \psi_0 | V | \psi_0 \rangle - \lambda^2 \sum_{n \neq 0} \frac{|\langle \psi_n | V | \psi_0 \rangle|^2}{E_n - E_0} \tag{4.25}$$

This energy difference can be approximated as a quadratic function of E_0:

$$\Delta E = a \cdot E_0^2 + b \cdot E_0 + c \tag{4.26}$$

Where a, b, and c are the coefficients that relate to the noise characteristics in the quantum system. It gives the same form in quadratic as Eq.4.19.

According to the statistic result, we collect the data points in Tab.4.4 to fit the curve.

E data	**P(E) data**
-0.480585	-0.011394
-0.26202	0
-0.096502	0.016229

Table 4.4: Data points used for quadratic curve fitting with 8192 shots, the physical meaning of the coefficients corresponding to all types of quadratic corrections.

Due to all the data points here being less than zero, which is restricted by our operators' mapping, we guess a symmetric noise influences the expectation value. So, the data points for values larger than zero should be with a minus sign; the curve will look like doing a π rotation from the origin.

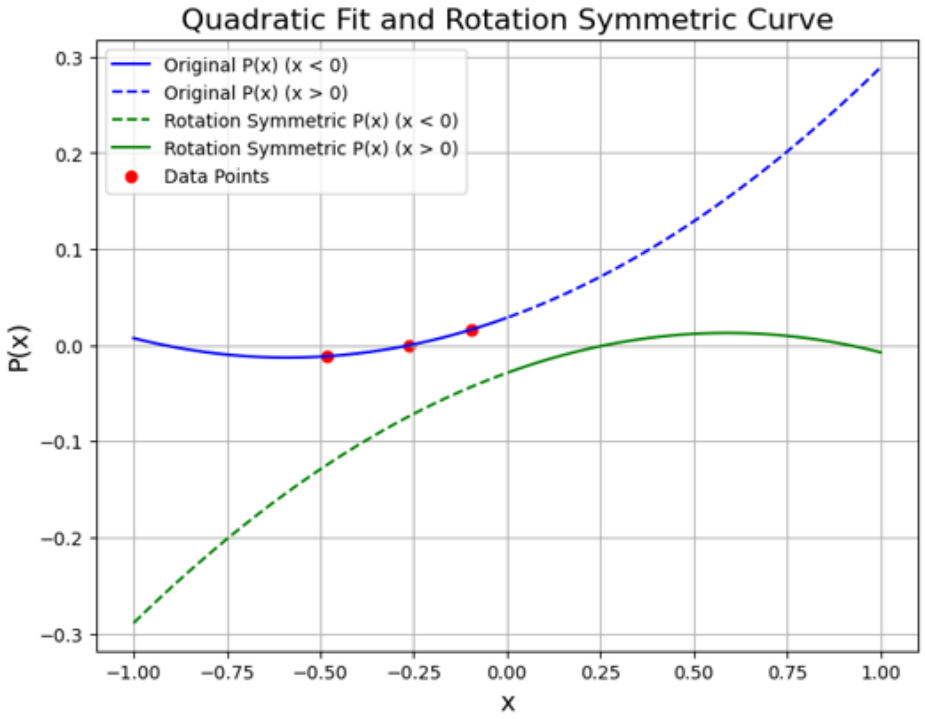

Figure 4.10: Quadratic fit and rotation symmetric curve used for result correction. The plot displays the original function $P(x)$ with distinct segments for $x < 0$ (solid blue line) and $x > 0$ (dashed blue line). The rotation symmetric version of $P(x)$ is due to the unbiased assumption on noise, with solid green for $x < 0$ and dashed green for $x > 0$. Red dots represent the data points used in the fitting process.

To ensure the reliability and accuracy of experimental measurements, it is essential to fit quadratic curves to datasets obtained from varying measurement configurations. This process helps evaluate the impact of noise and statistical fluctuations, particularly as the number of shots (N_{shots}) decreases. Fewer shots lead to greater susceptibility to noise, making it critical to understand the minimum N_{shots} required for reliable outcomes. The quadratic model can be validated by observing the consistency of the fitted parameters a, b, and c across different datasets.

Additionally, the intersection of the fitted curve with the x-axis, or the "zero" point, provides insight into the calibration of the measurement system. Consistent positioning of this point across varying N_{shots} indicates robust calibration. Moreover, this approach allows for the optimization of experimental resources by identifying the optimal N_{shots} that balances accuracy and resource usage. Finally, fitting the model to multiple configurations facilitates error analysis and uncertainty quantification, ensuring that the confidence intervals of the fitted parameters are well understood, thereby enhancing the reliability of the experimental conclusions. The results of this analysis are illustrated in Fig. 4.11, which shows the quadratic fits for different shot configurations along with their corresponding data points.

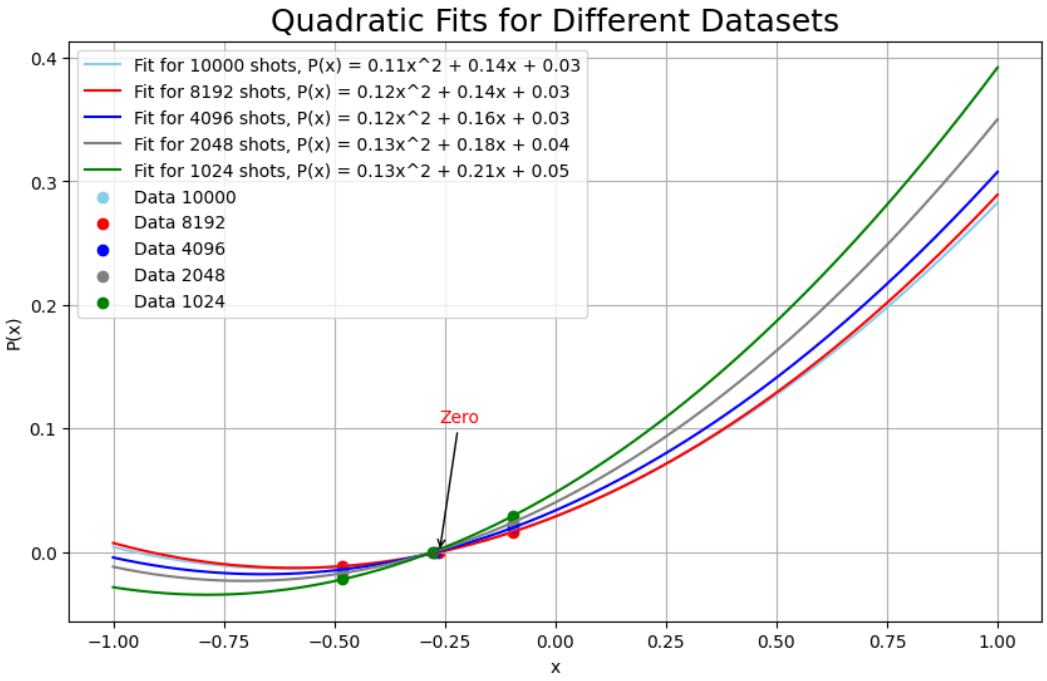

Figure 4.11: The plot illustrates the quadratic fits for datasets with different numbers of shots: 10,000 (gray), 8,192 (red), 4,096 (blue), 2,048 (black), and 1,024 (green). Each fit corresponds to a quadratic expression $ax^2 + bx + c$ with the coefficients displayed in the legend. Data points for each configuration are marked in different colours to indicate their corresponding datasets. The "Zero" point on the curve highlights where P(x) crosses the x-axis, reflecting the calibration of the measurement process. This comparison allows evaluation of how the number of shots affects the fit accuracy and stability of the quadratic model.

Refer to the figure above. The slope will gradually decrease and tend to. The correction amplitude may change when we vary the parameters for different energy expectation values, but the zero points will always be fixed. The physical explanation for the phenomenon near the zero point is that the probabilities on either side of the zero are often similar (positive and negative values tend to have comparable probabilities), so noise and statistical fluctuations tend to average out more effectively in this region. This contributes to the stability of the zero point.

4.2.4 Benchmarking and Cost Comparison

Benchmarking the quadratic mitigation technique is an essential step in rigorously evaluating its efficacy in minimizing noise and enhancing the precision of experimental outcomes. This process involves a detailed analysis of the method's performance across datasets with varying shot counts, focusing on critical parameters such as the stability of the fitted coefficients a, b, and c, as well as the consistency of the "zero" point calibration. By systematically comparing these metrics, we aim to comprehensively understand the technique's capacity to correct systematic errors and its robustness under different experimental conditions. The benchmarking results serve as a foundation for further refinement of the mitigation strategy, paving the way for future advancements that may include the integration of more sophisticated noise reduction algorithms or adaptive optimization frameworks.

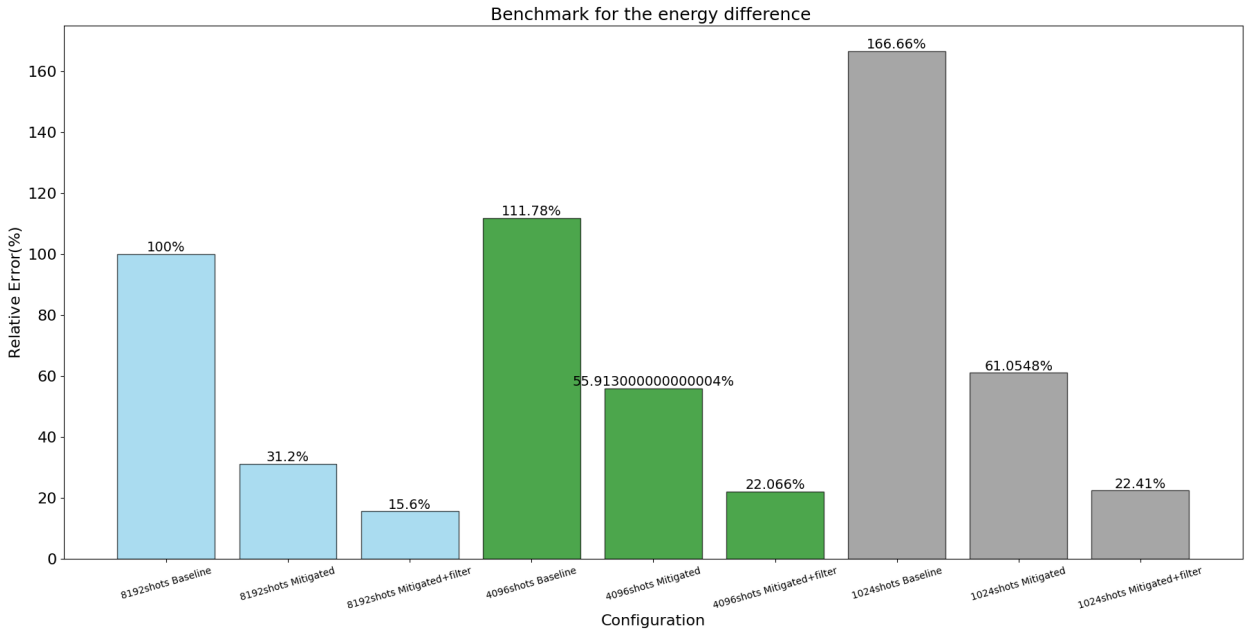

Figure 4.12: Benchmarking the impact of error mitigation strategies on the VQE results. The plot compares the relative error in energy differences across various configurations, representing different shot numbers (8192, 4096, and 1024) with baseline, mitigated, and mitigated with additional filtering. The figure demonstrates the effectiveness of error mitigation and filtering techniques in reducing the relative error of VQE results, highlighting their potential to enhance the accuracy of quantum computations on NISQ devices. Lower relative errors correspond to improved VQE performance.

Figure 4.12 presents a comparative analysis of error mitigation strategies on the accuracy of energy difference calculations in VQE experiments. The configurations shown vary by the number of shots (8192, 4096, and 1024), with each shot count evaluated in three modes: baseline (no mitigation), mitigated, and mitigated with additional filtering. The relative error percentages are plotted to indicate how close each configuration's results are to the ideal calculation.

The data clearly shows that applying error mitigation techniques drastically reduces the relative error across all configurations. For instance, the baseline configuration without mitigation at 8192 shots as the baseline, while the mitigated version reduces this error to 31.2%, and further, the addition of filtering brings it down to 15.6%. Similarly, for configurations with lower shot counts, such as 4096 and 1024, the error remains high in the baseline mode but drops substantially with mitigation and filtering.

This outcome underscores the importance of both error mitigation and filtering in achieving accurate quantum computations, especially in noisy environments characteristic of current NISQ devices. Error mitigation reduces the inaccuracies introduced by device noise, and additional filtering further refines the results by removing residual noise. This is particularly significant for lower shot counts, where fewer measurements typically result in higher statistical uncertainty. Thus, error mitigation and filtering make it feasible to achieve higher accuracy even with limited resources, such as fewer shots, demonstrating their effectiveness and necessity for enhancing the reliability of VQE and other quantum algorithms on today's quantum hardware.

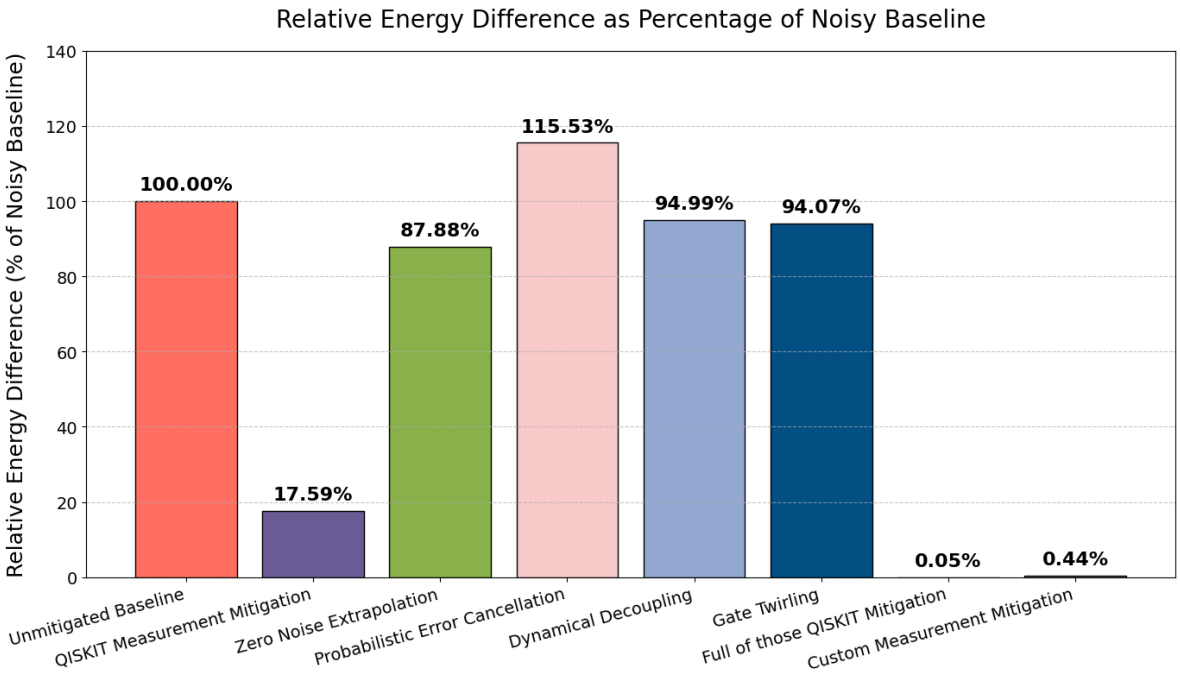

Figure 4.13: Relative Energy Difference (%) of Various Error Mitigation Techniques Compared to Unmitigated Baseline with 8192 shots in IBM quantum device. Our custom Measurement Mitigation demonstrates the lowest relative energy difference at 4.62%, while PEC shows the highest increase at 115.53% relative to the noisy baseline.

Figure 4.13 presents a comparative analysis of various error mitigation techniques, including Qiskit's built-in methods, by evaluating the relative energy difference on an IBM quantum device using 8192 shots. The unmitigated baseline is set at 100% as a reference point. Among Qiskit methods, zero-noise extrapolation achieves a notable reduction to 17.59%, demonstrating its effectiveness in diminishing noise-related errors. Other Qiskit techniques, such as dynamical decoupling and gate twirling, hover close to the baseline, indicating only modest improvement in accuracy.

Our custom measurement mitigation method drastically reduces relative energy difference to just 0.44%, surpassing all Qiskit approaches in efficacy. This substantial improvement suggests that our method is more tailored to suppress measurement-induced noise, likely offering a more precise calibration to the specific device characteristics compared to generalized Qiskit methods. Interestingly, PEC shows an increase to 115.53%, possibly due to additional sampling noise, which may exacerbate error rates in NISQ environments. This comparison underscores the potential of custom-tailored mitigation techniques in optimizing quantum computation accuracy, particularly when benchmarked against standard library-based methods.

The analysis in Figure 4.14 provides a detailed comparison of various error mitigation techniques, showing their effectiveness in reducing relative energy difference and their associated runtime costs. The unmitigated baseline, serving as the reference, has a short runtime of 12 seconds, indicating that without mitigation, computations are both rapid and highly noisy.

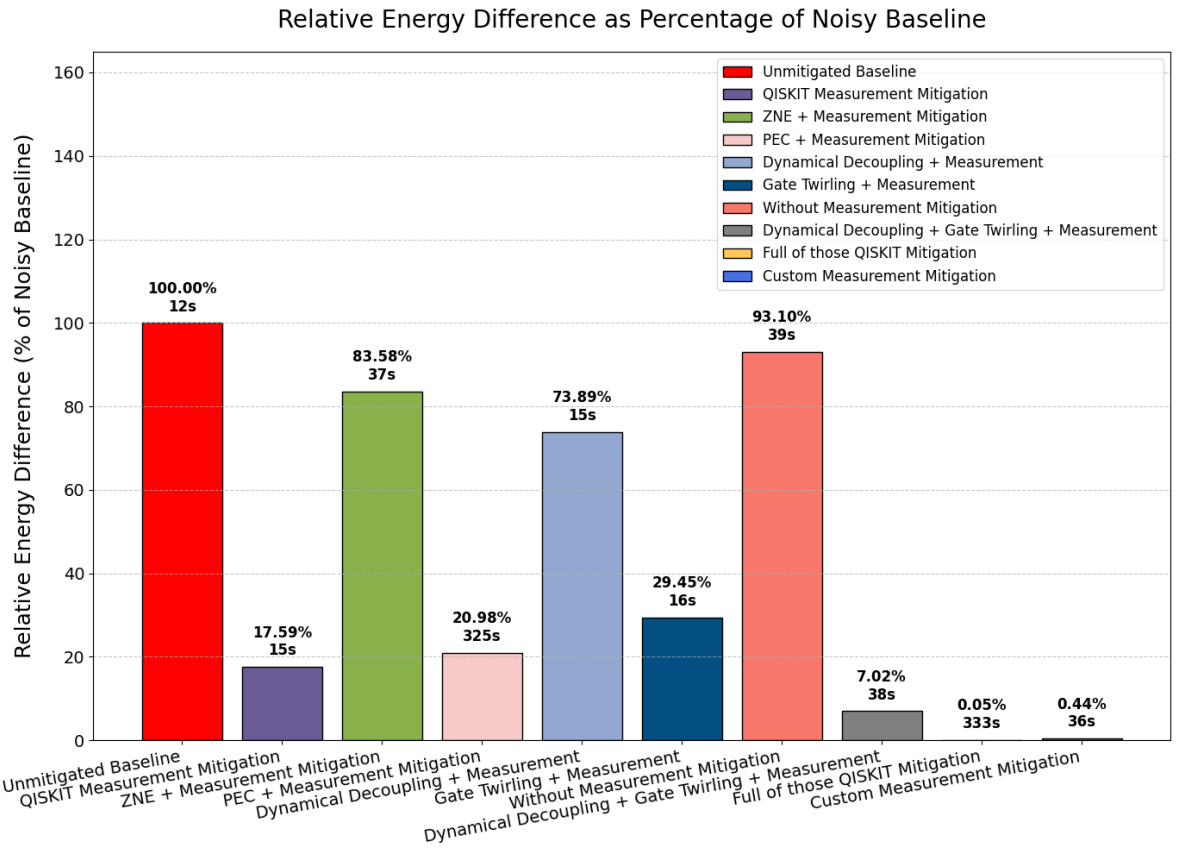

Figure 4.14: This figure presents a comparative analysis of error mitigation techniques applied to the VQE algorithm, showing the relative energy difference as a percentage of the unmitigated baseline and the runtime for each method. Notable observations include the effectiveness of QISKIT Measurement Mitigation, which achieves a substantial error reduction to 17.6% with minimal runtime increase, suggesting that measurement error correction alone can provide meaningful accuracy improvements with low computational cost. More advanced methods like Dynamical Decoupling and ZNE with measurement mitigation yield further error reductions (to around 7% and 21%, respectively), but with increased runtime, indicating a trade-off between accuracy and computational demand. Custom Measurement Mitigation demonstrates the lowest relative energy difference (0.44%) at a moderate runtime, highlighting the potential of tailored mitigation strategies to deliver high accuracy efficiently. Meanwhile, the Full QISKIT Mitigation approach shows diminishing returns, offering limited accuracy gains (93.1%) compared to the unmitigated baseline but at a higher computational cost, suggesting that selective use of mitigation techniques may be more effective. Overall, these results underscore the importance of balancing accuracy and computational efficiency when selecting error mitigation strategies for NISQ devices.

Each mitigation technique or combination applied yields varying improvements in accuracy but at different runtime costs. For instance, Qiskit's measurement mitigation, which reduces the error to 17.59%, has a moderate runtime increase to 15 seconds, demonstrating a balanced improvement in accuracy with minimal time overhead. The combination of ZNE and measurement mitigation, achieving 83.58% relative energy difference, takes 37 seconds, suggesting that ZNE adds significant time without proportional accuracy gains in this context. That means that compared to the PEC, our mitigation can lower the time cost by ten times with 250 times precisely the output simultaneously.

When combined with measurement mitigation, PEC produces a relative error of 73.89% and

takes only 15 seconds, but its error reduction is less effective than other methods. Dynamical decoupling combined with gate twirling shows improved accuracy (29.45%) with a modest runtime increase to 16 seconds, highlighting its efficiency for certain quantum noise types.

The most effective approach, as observed, is our custom measurement mitigation, which achieves an extremely low relative error of 0.44% within 36 seconds, showing a clear advantage over other methods in balancing accuracy and time. Another noteworthy setup is the full suite of Qiskit mitigation techniques, which reduces the error to 0.05% but with a significant runtime increase to 333 seconds, indicating that while highly accurate, it is not time-efficient.

In summary, our custom measurement mitigation stands out for achieving near-optimal accuracy with relatively low runtime, making it a practical solution for high-precision quantum computations. Other methods, such as full Qiskit mitigation, are highly accurate but less feasible for time-sensitive applications, emphasizing the importance of selecting mitigation strategies based on specific performance and time constraints.

4.3 Future Works

For future work, there is a need to investigate the underlying causes of the limited performance observed with PEC in our benchmarks. While PEC is theoretically powerful, our results indicate it provides less accuracy improvement than other methods and, in some cases, even increases the relative energy difference. This discrepancy suggests that certain practical factors, such as noise model mismatch, additional sampling overhead, or the compounding effects of device-specific noise, may reduce PEC's effectiveness on our current hardware. We aim to explore these factors in depth, conducting targeted experiments to isolate which aspects of PEC implementation are responsible for this performance gap. Additionally, we will explore optimized combinations of error mitigation techniques tailored to specific noise profiles, allowing for a more nuanced and efficient approach to reducing errors.

Another approach to reducing the energy difference involves transforming the observable to bring its expectation value closer to zero, minimizing the gap between noisy and noiseless results. This transformation adjusts the observable in a way that reduces the impact of noise on the measurement, allowing for a more accurate estimation of the true value by effectively aligning the expectation closer to the zero point, where the difference is minimized.

To formalize this approach, we define the transformation U as follows:

$$O' = UO \tag{4.27}$$

The expectation value of O' in the noisy state then becomes:

$$\left\langle O' \right\rangle_{\text{noisy}} = \langle UO \rangle_{\text{ideal}} - \langle UO \rangle_{\text{noisy}} = 0 \tag{4.28}$$

where $\langle O \rangle_{\text{noisy}}$ is the expectation value of O measured in the noisy environment. The relative energy difference is thereby reduced, as the measurement error induced by noise is now expressed as a small offset around zero, enhancing the accuracy of the quantum computation.

These strategies and relationships can be validated using the Lipkin model, which was simulated in the previous work and involves only one variational parameter. Achieving this validation suggests that our method could become a more versatile and widely applicable approach for future calculations and deployments.

5
Conclusion

Using the Nuclear Shell Pairing Model as a test model, this study investigates the intricate relationship between gate fidelity, the number of variational parameters in *ansatz* configurations, quantum volume, and the accuracy of energy estimation in quantum simulations. By developing a noise model tailored to IBMQ Heron and Eagle devices—characterized by distinct quantum gate sets and quantum volumes—we examined how device characteristics and *ansatz* configurations influence energy estimation accuracy in the VQE algorithm.

A key finding of our research is the linear correlation between energy estimation error and the number of gates, rather than the number of variational parameters, across different ansatz configurations. Specifically, for our custom-designed effective ansatz, the gate count scales linearly with the addition of parameters, offering a significant advantage over traditional *ansatz* choices like EfficientSU(2). This efficient scaling enabled our *ansatz* to achieve a relative error of 1e-3 to 1e-4 on Eagle r3 devices for IBMQ Brisbane, surpassing the performance of conventional *ansatz* approaches on comparable quantum volumes.

In addition to analyzing gate fidelity, we explored how the number of parameters in the *ansatz* influences the convergence of energy estimates. Our findings reveal that while increasing parameters can improve the expressiveness of the *ansatz*, it also escalates gate requirements, which, in turn, impacts the cumulative error due to imperfect gate fidelity. This highlights a balance between *ansatz* complexity and hardware limitations, suggesting that optimizing the number of parameters is crucial for accurate and efficient simulations on NISQ devices.

We further investigated how quantum volume a metric of a device's effective capability for complex quantum computations—interacts with error mitigation strategies to enhance VQE performance. By creating the corresponding noise model to the quantum volumes of IBMQ devices in different generations, we accounted for device-specific error rates, enabling a more realistic evaluation of energy estimation. Our custom error mitigation techniques for quadratic corrections, designed to address gate and measurement errors, effectively reduced discrepancies between the estimated and actual ground state energy. These mitigation strategies allowed us to lower the impact of gate fidelity and readout process more precisely up to $250x$ referring to the unmitigated result, isolating noise's effects and improving our energy estimates' reliability to reduce the usage of other heavy mitigation strategies like PEC and Pauli gate twirling, so the total time cost can be saved up to $10x$ on QPU that means ten times cheaper than before.

Overall, our work underscores the importance of integrating device-specific error models, parameter optimization in the *ansatz*, and tailored error mitigation techniques to advance the accuracy of quantum simulations in the NISQ era. This research contributes to the foundational understanding needed to develop scalable and reliable quantum algorithms for realistic applications in nuclear physics, not only for the nuclear pairing model but also for others beyond, paving the way for more sophisticated quantum computations as hardware continues to evolve.

A
Appendix

A.1 Introduction to the Theoretical Background

Effective Field Theory (EFT) provides a powerful framework for describing interactions at low energies, particularly for non-relativistic scattering processes, which align with the assumptions outlined earlier [5, 9]. By employing EFT, we can systematically include higher-order terms, thereby accommodating a variety of interaction operators. In the non-relativistic energy regime, interactions are typically expressed in terms of four-fermion operators. The use of EFT allows us to reduce the complexity of the DM-nucleon interaction by simplifying the two-body problem into an effective one-body problem with the reduced mass $\mu_N = \frac{m_\chi m_N}{m_\chi + m_N}$, where m_χ is the mass of the dark matter particle and m_N is the mass of the nucleon.

Before delving into EFT-based calculations, it is beneficial to first evaluate a simple relativistic case. This will highlight the advantages of EFT and illustrate its purpose in addressing low-energy interactions.

A.1.1 Relativistic Calculations of Dark Matter-Nucleon Scattering

We begin by considering the relativistic form of the interaction without using Effective Field Theory (EFT). EFT is advantageous because it allows us to describe scattering processes using general symmetry considerations without needing to specify the exact form of the interaction potential. The symmetries of the scattering cross-section are reflected in several conserved quantities:

- **Spherical symmetry** of the potential ensures angular momentum conservation.
- **Parity symmetry** guarantees that the physics remains invariant under spatial reflection.
- **Translational symmetry** ensures the conservation of total four-momentum.
- **Low-energy behavior** (low momentum transfer limit) indicates that the cross-section primarily depends on these symmetries rather than the specific details of the interaction potential.

In relativistic dynamics, the relationship between energy E and momentum $\vec{p}$ is encapsulated by the well-known expression:

$$E^2 = \vec{p}^2 c^2 + m^2 c^4, \tag{A.1}$$

where m is the rest mass of the particle and $\vec{p}$ is the three-momentum. In the relativistic framework, it is more convenient to use the four-momentum $p^\mu = (E/c, \vec{p})$. The four-momentum transfer in a scattering process is given by:

$$q^\mu = p_i^\mu - p_f^\mu, \tag{A.2}$$

where p_i^μ and p_f^μ are the initial and final four-momenta of the particle. The invariant magnitude of the four-momentum transfer is:

$$q^2 = (p_i - p_f)^2 = (E_i - E_f)^2 - (\vec{p}_i - \vec{p}_f)^2. \tag{A.3}$$

For a scattering process involving a point-like dark matter particle of mass m, the momentum transfer q^μ will play a central role. In this analysis, we are interested in the differential cross-section and the event transition rate, both of which can be computed using Fermi's Golden Rule. The transition rate is determined by the matrix element of the interaction potential.

Assuming the internal structure of the nucleus remains unchanged, we have $\phi_i(\vec{R}) = \phi_f(\vec{R})$. The initial wavefunction is given by:

$$\psi_i = \exp\left(\frac{i}{\hbar}\vec{p}_l \cdot \vec{r}\right)\phi_i(\vec{R}), \tag{A.4}$$

where $\vec{p}_l$ is the three-momentum of the incident particle.

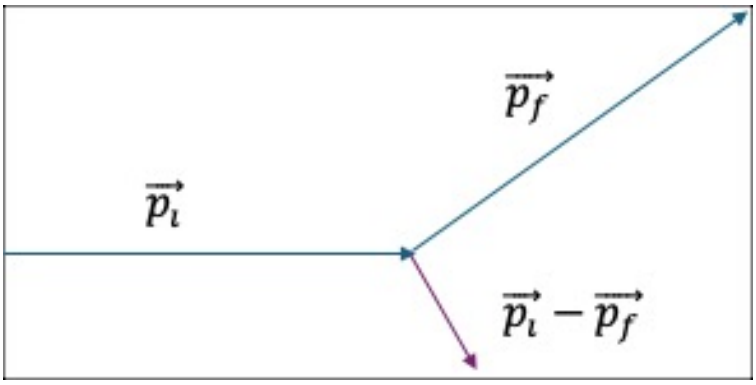

Figure A.1: A diagram illustrating the DM-nucleus scattering process, with momentum transfer $\vec{q} = \overrightarrow{p_l} - \overrightarrow{p_f}$. In this case, only low momentum transfer occurs, with no internal interaction or excitation, so all particles are treated as point-like.

As shown in Fig. A.1, the matrix element for the scattering process is given by:

$$\langle f|\hat{V}|i\rangle = \int \psi_f^*(r)\hat{V}(r)\psi_i(r)d^3r. \tag{A.5}$$

In this calculation, two distinct forms of the particle-nucleus interaction will be evaluated:

$$\begin{aligned} V_1(\vec{r},\vec{R}) &= C_1 \exp\left(-\frac{|\vec{r}-\vec{R}|}{d}\right), \\ V_2(\vec{r},\vec{R}) &= C_2 \exp\left(-\frac{(\vec{r}-\vec{R})^2}{2d^2}\right). \end{aligned} \tag{A.6}$$

For V_1, the matrix element according to Eq. A.5 is:

$$\langle f|\hat{V}_1|i\rangle = C_1 \int \psi_f^* \exp\left(-\frac{|r-R|}{d}\right)\psi_i d^3r, \tag{A.7}$$

which expands as:

$$\langle f|\hat{V}_1|i\rangle = C_1 \int \left(\exp\left(\frac{i}{\hbar}\overrightarrow{p_f}\cdot\vec{r}\right)\phi_f(\vec{R})\right)^* \exp\left(-\frac{|r-R|}{d}\right)\exp\left(\frac{i}{\hbar}\overrightarrow{p_l}\cdot\vec{r}\right)\phi_i(\vec{R})d^3r. \tag{A.8}$$

This integral can be simplified to:

$$C_1 \int \exp\left(\frac{i}{\hbar}\overrightarrow{p_f}\cdot\vec{r}\right)^* \exp\left(-\frac{|r-R|}{d}\right)\exp\left(\frac{i}{\hbar}\overrightarrow{p_l}\cdot\vec{r}\right)d^3r. \tag{A.9}$$

The dependence on R factors out due to the property $\phi_i^*(\vec{R})\phi_i(\vec{R}) = 1$, and we set the nucleus position to $R = 0$. The matrix element then becomes:

$$\langle f|\hat{V}_1|i\rangle = C_1 \int \exp\left(\frac{i}{\hbar}(\overrightarrow{p_l} - \overrightarrow{p_f})\cdot\vec{r}\right)\exp\left(-\frac{|r-R|}{d}\right)d^3r. \tag{A.10}$$

Further simplifying using spherical coordinates, we have:

$$\langle f|\hat{V}_1|i\rangle = C_1 \int_0^\infty \int_0^\pi \int_0^{2\pi} \exp\left(\frac{i}{\hbar}\vec{q}r\cos\theta\right)\exp\left(-\frac{r}{d}\right)r^2\sin\theta d\phi d\theta dr, \tag{A.11}$$

where $\vec{q} = \overrightarrow{p_l} - \overrightarrow{p_f}$ and $q^2 = (p_i - p_f)^2 = 2p^2(1-\cos\theta)$. The volume element is $d^3r = r^2\sin\theta dr d\theta d\phi$. Solving the integral, we obtain the following scattering amplitude:

$$\langle f|\hat{V}_1|i\rangle = 4\pi C_1 \int_0^\infty \exp\left(-\frac{r}{d}\right)r^2\frac{\sin\left(\frac{qr}{\hbar}\right)}{\frac{qr}{\hbar}}dr = \frac{4\pi C_1 d^3}{(q^2d^2+\hbar^2)^2}. \tag{A.12}$$

For the Gaussian potential V_2, the matrix element is given by:

$$\langle f|\hat{V}_2|i\rangle = C_2 \int \exp\left(\frac{i}{\hbar}(\overrightarrow{p_i} - \overrightarrow{p_f})\cdot\vec{r}\right)\exp\left(-\frac{(\vec{r}-\vec{R})^2}{2d^2}\right)d^3r. \tag{A.13}$$

Using the same method as before, the integral in spherical coordinates becomes:

$$\langle f|\hat{V}_2|i\rangle = C_2 \int_0^\infty \int_0^\pi \int_0^{2\pi} \exp\left(\frac{i}{\hbar}qr\cos\theta\right)\exp\left(-\frac{r^2}{2d^2}\right)r^2\sin\theta d\phi d\theta dr, \tag{A.14}$$

which simplifies to:

$$\langle f|\hat{V}_2|i\rangle = \frac{4\pi^{3/2}C_2 d^3}{\hbar^3}\exp\left(-\frac{q^2d^2}{2\hbar^2}\right). \tag{A.15}$$

Now, applying Fermi's Golden Rule (FGR) to get the scattering amplitude, we compute the differential cross-section as a simple 2-to-2 phase space Feynman diagram in the centre of mass frame with the integral all over the phase by the Lippmann-Schwinger equation Π_{LIPS}.

$$d\sigma = \frac{1}{4E_\chi E_N\,|\vec{v}_\chi - \vec{v}_N|}|\mathcal{M}|^2 d\Pi_{\text{LIPS}} \tag{A.16}$$

The differential cross-sections for the exponential and Gaussian potentials are proportional to the square of the matrix element:

$$\frac{d\sigma_1}{d\Omega} \propto \left|\langle f|\hat{V}_1|i\rangle\right|^2 = \frac{1}{(q^2d^2+\hbar^2)^4} \tag{A.17}$$

$$\frac{d\sigma_2}{d\Omega} \propto \left|\langle f|\hat{V}_2|i\rangle\right|^2 = \exp\left(-\frac{q^2d^2}{\hbar^2}\right) \tag{A.18}$$

Within the low momentum transfer limit $\left(q^2d^2 \ll \hbar^2\right)$, the differential cross-section can be expanded by letting the denominator be a series in a binomial expansion:

$$\left(1+\frac{q^2d^2}{\hbar^2}\right)^{-4} \approx 1-4\frac{q^2d^2}{\hbar^2}+\mathcal{O}\left(\left(\frac{q^2d^2}{\hbar^2}\right)^2\right) \tag{A.19}$$

$$\exp\left(-\frac{q^2d^2}{\hbar^2}\right) \approx 1-\frac{q^2d^2}{\hbar^2}+\mathcal{O}\left(\left(\frac{q^2d^2}{\hbar^2}\right)^2\right) \tag{A.20}$$

By setting the and considering the rest as the constant, both the two potentials with exponential and Gaussian forms will approximately have the equivalent cross-section.

$$\frac{d\sigma_1}{d\Omega} \propto const\left(1-4\frac{q^2d^2}{\hbar^2}\right), \frac{d\sigma_2}{d\Omega} \propto const\left(1-\frac{q^2d^2}{\hbar^2}\right) \tag{A.21}$$

So in the low-energy limit, both the exponential and Gaussian potentials yield scattering nearly constant cross-sections, with small corrections that depend on q^2. This shows that in this limit, the exact form of the potential becomes irrelevant, and both potentials yield equivalent behaviour, which justifies the use of EFT, where symmetry and low-energy behaviour are more important than the specific form of the interaction.

A.1.2 Introduction to Effective Field Theory for Dark Matter Interactions

As demonstrated in the previous section, it is now evident that the calculation is no longer dependent on the wave function of the nucleus ground state but rather on the charge distribution, also known as the form factor [66].

In the framework of Effective Field Theory (EFT) [5, 9, 67], the interactions are treated systematically through an expansion in terms of the momentum transfer and relative velocity of the dark matter (DM) particle. The relative velocity between the incoming DM particle and the nucleon, in the nucleon rest frame, with the incoming kinetic energy $E_{\text{initial}} = \frac{1}{2}\mu_N v^2$ and momentum transfer $\vec{q} = \vec{p}_{\text{final}} - \vec{p}_{\text{initial}}$, is given by:

$$\vec{v} \equiv \vec{v}_{\chi,\text{in}} - \vec{v}_{N,\text{in}}, \quad \vec{v_0} = \frac{\vec{q}}{\mu_N} \tag{A.22}$$

In the non-relativistic limit, the outgoing energy is described by:

$$E_{\text{out}} = \frac{1}{2}\mu_N\left(\vec{v}+\frac{\vec{q}}{\mu_N}\right)^2 \tag{A.23}$$

Applying energy conservation to the scattering process, we have the following conditions:

$$E_{\text{in}} = E_{\text{out}} \tag{A.24}$$

$$\vec{v}\cdot\vec{q} = -\frac{q^2}{2\mu_N} \tag{A.25}$$

This ensures that the total energy remains conserved during the interaction. The advantage of using EFT is that it simplifies the treatment of low-energy scattering processes by capturing the relevant physics through effective operators, which can be systematically derived based on symmetries and scales relevant to the problem. For the momentum operator, it ideally follows the relation below.

$$\hat{p}^\dagger = (-i\hbar\nabla)^\dagger = i\hbar\left(\nabla^\dagger\right) = i\hbar(-\nabla) = -i\hbar\nabla = \hat{p} \tag{A.26}$$

The $\nabla^\dagger = -\nabla, \nabla^2 = \left(\nabla^2\right)^\dagger$ comes out from the derivation as a scalar function $\nabla = \left(\frac{\partial}{\partial x}, \frac{\partial}{\partial y}, \frac{\partial}{\partial z}\right)$, in the non-relativistic EFT form, the kinetic action with the property $\phi = \phi^- + \phi^+, N = N^- + N^+$ for DM ϕ and Nuclei N are

$$\phi^-(y) \equiv \int \frac{d^3p}{(2\pi)^3}\frac{1}{\sqrt{2m_\chi}}e^{-ip\cdot y}a_p^\dagger, \phi^+(y) \equiv \int \frac{d^3p}{(2\pi)^3}\frac{1}{\sqrt{2m_\chi}}e^{ip\cdot y}a_p \tag{A.27}$$

$$N^-(y) \equiv \int \frac{d^3k}{(2\pi)^3}\frac{1}{\sqrt{2m_N}}e^{-ik\cdot y}a_k^\dagger, N^+(y) \equiv \int \frac{d^3k}{(2\pi)^3}\frac{1}{\sqrt{2m_N}}e^{ik\cdot y}a_k \tag{A.28}$$

Where y is the space variable in 3D, the relation shows the crossing symmetry $(\phi^-)^\dagger = \phi^+, (N^-)^\dagger = N^+$, corresponding to Hermitian conjugation exchanges incoming for outgoing particles. In effective theory the kinetic part of the action in non-relativistic form will be

$$\mathcal{L}_{\text{kin}} = 2m_\phi\phi^+(y)\left(i\frac{\partial}{\partial t} - \frac{\nabla^2}{2m_\phi}\right)\phi^-(y) \tag{A.29}$$

The Hermitian conjugate of the temporal derivative is given by

$$\left(i\phi^+(y)\frac{\partial}{\partial t}\phi^-(y)\right)^\dagger = (i)^\dagger\left(\phi^+(y)\right)^\dagger\left(\frac{\partial}{\partial t}\phi^-(y)\right)^\dagger = -i\phi^-(y)\frac{\partial}{\partial t}\phi^+(y) \tag{A.30}$$

The spatial term Hermitian conjugate is

$$\left(-\frac{\nabla^2}{2m_\phi}\phi^+(y)\phi^-(y)\right)^\dagger = -\frac{\nabla^2}{2m_\phi}\left(\phi^+(y)\right)^\dagger\left(\phi^-(y)\right)^\dagger = -\frac{\nabla^2}{2m_\phi}\phi^-(y)\phi^+(y) \tag{A.31}$$

Combining those two terms, we could find $\mathcal{L}_{\text{kin}}^\dagger$

$$\left(2m_\phi\phi^+(y)\left(i\frac{\partial}{\partial t} - \frac{\nabla^2}{2m_\phi}\right)\phi^-(y)\right)^\dagger = 2m_\phi\phi^-(y)\left(-i\frac{\partial}{\partial t} - \frac{\nabla^2}{2m_\phi}\right)\phi^+(y) \tag{A.32}$$

$$= -2m_\phi\phi^+(y)\left(i\frac{\partial}{\partial t} + \frac{\nabla^2}{2m_\phi}\right)\phi^-(y) \tag{A.33}$$

According to Eq.A.33, it shows the crossing symmetry for the effective field theory; the order will be changed since there's a hermitian conjugate applied to Eq.A.29. To keep all the DM-Nuclei interaction operators as Hermitian, we have to rewrite the form of velocity we used to satisfy $\vec{v}^\perp \cdot \vec{q} = 0$, so the modified perpendicular velocity with Hermiticity is

$$\vec{v}^\perp \equiv \vec{v} + \frac{\vec{q}}{2\mu_N} \tag{A.34}$$

The perpendicular velocity will be examined for Hermitian operators $\hat{A}$ and $\hat{B}$. It keeps the linearity property: $(\hat{A} - \hat{B})^\dagger = \hat{A}^\dagger - \hat{B}^\dagger$.

$$\vec{v}_\perp^\dagger = \left(\vec{v} + \frac{\vec{q}}{2\mu_N}\right)^\dagger = \vec{v}^\dagger + \left(\frac{\vec{q}}{2\mu_N}\right)^\dagger \tag{A.35}$$

We can expand the expression from the definition of $q = p' - p$; here, we unify the index by using in and out.

$$\vec{v}_\perp^\dagger = (\vec{v}_{\chi,\text{in}} - \vec{v}_{N,\text{in}})^\dagger + \left(\frac{p_\text{out} - p_\text{in}}{2\mu_N}\right)^\dagger \tag{A.36}$$

$$= (\vec{v}_{\chi,\text{out}} - \vec{v}_{N,\text{out}}) + \left(\frac{\vec{v}_{\chi,\text{out}} m_\chi - \vec{v}_{\chi,\text{in}} m_\chi}{2\mu_N}\right)^\dagger \tag{A.37}$$

$$= (\vec{v}_{\chi,\text{out}} - \vec{v}_{N,\text{out}}) + \left(\frac{\vec{v}_{\chi,\text{in}} m_\chi - \vec{v}_{\chi,\text{out}} m_\chi}{2\mu_N}\right) \tag{A.38}$$

Since the $\vec{v} \xrightarrow{\dagger} \vec{v}_{\chi,\text{out}} - \vec{v}_{N,\text{out}} = \vec{v} + \frac{\vec{q}}{\mu_N}$, we can get it by cancelling the minus sign in the second term.

$$\vec{v}_\perp^\dagger = \left(\vec{v} + \frac{\vec{q}}{\mu_N}\right) - \left(\frac{\vec{v}_{\chi,\text{out}} m_\chi - \vec{v}_{\chi,\text{in}} m_\chi}{2\mu_N}\right) \tag{A.39}$$

$$= \left(\vec{v} + \frac{\vec{q}}{\mu_N}\right) - \frac{\vec{q}}{2\mu_N} = \vec{v} + \frac{\vec{q}}{2\mu_N} = \vec{v}_\perp \tag{A.40}$$

Under the crossing symmetry it is truly that $\vec{v}_\perp^\dagger = \vec{v}_\perp$, but the operator $\vec{q}$ is not hermitian as shown in Eq.A.38, so we have to construct a hermitian operator as $i\vec{q}$, which can be proved as

$$(i\vec{q})^\dagger = (-i)(\vec{q})^\dagger \tag{A.41}$$

$$(-i)(p_\text{out} - p_\text{in})^\dagger = (-i)(\vec{v}_{\chi,\text{out}} m_\chi - \vec{v}_{\chi,\text{in}} m_\chi)^\dagger \tag{A.42}$$

$$= (-i)(\vec{v}_{\chi,\text{in}} m_\chi - \vec{v}_{\chi,\text{out}} m_\chi) = i(\vec{v}_{\chi,\text{out}} m_\chi - \vec{v}_{\chi,\text{in}} m_\chi) = i\vec{q} \tag{A.43}$$

Now we have the Hermitian physical variables for $i\vec{q}, \vec{v}^\perp, \vec{S}_\chi, \vec{S}_N$ in use with crossing symmetry. Note that the expression for the spin operator $\vec{S}$ such spin-$\frac{1}{2}$ particle with Pauli matrix σ (also Hermitian) is

$$\sigma_x = \begin{pmatrix} 0 & 1 \\ 1 & 0 \end{pmatrix} \sigma_y = \begin{pmatrix} 0 & -i \\ i & 0 \end{pmatrix} \sigma_z = \begin{pmatrix} 1 & 0 \\ 0 & -1 \end{pmatrix} \tag{A.44}$$

Where the spin operators hold the hermitian property

$$\hat{S}^\dagger = \left(\frac{\hbar}{2}\hat{\sigma}\right)^\dagger = \frac{\hbar}{2}\hat{\sigma}^\dagger = \frac{\hbar}{2}\hat{\sigma} = \hat{S} \tag{A.45}$$

Where $\vec{S} = \frac{\hbar}{2}\vec{\sigma_i}$, and the index i from $1-3$ for x,y,z dimension. Since the non-relativistic theory has to satisfy Lorentz invariance, it must have time reverse symmetry T [68, 69]. Spins for nucleons and DM particles also follow T symmetry due to the angular momentum behaviour $T : \omega \to -\omega$. It will be the opposite sign when the spin flips under T. Velocity and momentum also have the same feature: $T : O \to -O$.

The constraints of CP violation should be taken care of here. Even though the physical properties above will not change the sign in P symmetry, we will also use the even and odd to distinguish the operators. Here is a transformation table for them: $+1$ means the sign will not change, and -1 for a sign will change. Finally, we can learn the operators' signs by multiplying the terms [5].

	Hermitian	T	P
$\vec{S}$	$+1$	-1	$+1$
$i\vec{q}$	$+1$	$+1$	-1
$\vec{v}^{\perp}$	$+1$	-1	-1

Considering different scattering configurations, the categories can distinguish the two-body interaction operator. Some operators will depend on spin, others will be spin-independent, and some will depend on spin-spin or spin-orbital interaction. The total sets of operators can be expressed and shown in Tab.A.1.

Operator	**Expression**
Scalar and Velocity-Squared Operators	
$\mathcal{O}_1$	$1_\chi 1_N$
$\mathcal{O}_2$	$\left(v^{\perp}\right)^2$
$\mathcal{O}_3$	$i\vec{S}_N \cdot \left(\frac{\vec{q}}{m_N} \times \vec{v}^{\perp}\right)$
Spin-Spin Operators	
$\mathcal{O}_4$	$\vec{S}_N \cdot \vec{S}_\chi$
$\mathcal{O}_5$	$i\vec{S}_\chi \cdot \left(\frac{\vec{q}}{m_N} \times \vec{v}^{\perp}\right)$
$\mathcal{O}_6$	$\left(\vec{S}_\chi \cdot \frac{\vec{q}}{m_N}\right)\left(\vec{S}_N \cdot \frac{\vec{q}}{m_N}\right)$
Spin-Velocity Operators	
$\mathcal{O}_7$	$\vec{S}_N \cdot \vec{v}^{\perp}$
Spin-Velocity Cross Product Operators	
$\mathcal{O}_8$	$\vec{S}_\chi \cdot \vec{v}^{\perp}$
$\mathcal{O}_9$	$i\vec{S}_\chi \cdot \left(\vec{S}_N \times \frac{\vec{q}}{m_N}\right)$
Momentum-Spin Operators	
$\mathcal{O}_{10}$	$i\vec{S}_N \cdot \frac{\vec{q}}{m_N}$
$\mathcal{O}_{11}$	$i\vec{S}_\chi \cdot \frac{\vec{q}}{m_N}$
Complex Spin-Orbit Operators	
$\mathcal{O}_{12}$	$\vec{S}_\chi \cdot \left(\vec{S}_N \times \vec{v}^{\perp}\right)$
$\mathcal{O}_{13}$	$i\left(\vec{S}_\chi \cdot \vec{v}^{\perp}\right)\left(\vec{S}_N \cdot \frac{\vec{q}}{m_N}\right)$
$\mathcal{O}_{14}$	$i\left(\vec{S}_\chi \cdot \frac{\vec{q}}{m_N}\right)\left(\vec{S}_N \cdot \vec{v}^{\perp}\right)$
$\mathcal{O}_{15}$	$-\left(\vec{S}_\chi \cdot \frac{\vec{q}}{m_N}\right)\left[\left(\vec{S}_N \times \vec{v}^{\perp}\right) \cdot \frac{\vec{q}}{m_N}\right]$

Table A.1: List of effective field theory operators for dark matter direct detection. Here, $\vec{S}_\chi$ is the WIMP spin, $\vec{S}_N$ is the nucleon spin, $\vec{q}$ is the momentum transfer, and $\vec{v}^{\perp}$ is the perpendicular component of the relative incoming velocity. Operators are categorized based on their spin, momentum, and velocity dependence [9].

So the total interaction Hamiltonian that sums all of the possible interaction operators for nucleons with the corresponding coupling coefficients c_i^x can be expressed as [9]

$$\mathcal{H} = \sum_{x=N} \sum_{i=1}^{15} c_i^x \mathcal{O}_i^x \tag{A.46}$$

So the DM response function $R^{x,x'}$ can be expressed as

$$R^{x,x'} = \left| \left\langle f \left| \sum_{x=N} \sum_{i=1}^{15} c_i^x \mathcal{O}_i^x \right| i \right\rangle \right|^2 \tag{A.47}$$

Then we need to determine the matrix element for the transition rate in order to obtain the nuclear (target) response function, which can be represented as $\langle f | X_{JT} | i \rangle$. The FGR can be used to describe the scattering probability for a system with a perturbation H' acting on the Hamiltonian H mentioned above.

$$\Gamma_{i \to f} = \frac{2\pi}{\hbar} \left| \left\langle f \left| H' \right| i \right\rangle \right|^2 \rho\left(E_f\right) \tag{A.48}$$

Where $\rho\left(E_f\right)$ is the density of states, $\Gamma_{i \to f}$ is the transition rate between the initial and final state. With the definition above, the state $|\Psi_i\rangle$ is often the ground state of the nucleus, and $|\Psi_f\rangle$ can be an excited state or the ground state (in the case of elastic scattering, since the energy transfer will not excite the nuclear, that's the case our project aiming to).

The Wigner-Eckart theorem states that the matrix element of a tensor operator can be separated into a reduced matrix element and a Clebsch-Gordan coefficient as shown in Eq.A.49. This means that the complex total expression can be broken down into the sum of product terms [70]. The matrix elements are scalars that depend only on the quantum numbers of the states. The nuclear response operators $X_{J_T}^x$ are effectively shown in Tab.A.2, where J_T is the angular momentum rank of the operator.

$$\left| \left\langle f \left| H' \right| i \right\rangle \right|^2 = \left\langle \Psi_f \left\| X_{J_T}^x \right\| \Psi_i \right\rangle \left\langle \Psi_i \left\| X_{J_T}^{x'} \right\| \Psi_f \right\rangle \tag{A.49}$$

Types of X_{JT}	Expression of Nuclear Response Operators
M_{JM}	$M_{JM}(q\vec{x}) \equiv j_J(qx) Y_{JM}\left(\Omega_x\right)$
Δ_{JM}	$\vec{M}_{JM} \cdot \frac{1}{q}\vec{\nabla}$
Σ'_{JM}	$-i\left\{\frac{1}{q}\vec{\nabla} \times \vec{M}_{JJM}\right\} \cdot \vec{\sigma}$
Σ''_{JM}	$\left\{\frac{1}{q}\vec{\nabla} M_{JM}\right\} \cdot \vec{\sigma}$
$\tilde{\Phi}'_{JM}$	$\left(\frac{1}{q}\vec{\nabla} \times \vec{M}_{JM}\right) \cdot \left(\vec{\sigma} \times \frac{1}{q}\vec{\nabla}\right) + \frac{1}{2}\vec{M}_{JM} \cdot \vec{\sigma}$
Φ''_{JM}	$i\left(\frac{1}{q}\vec{\nabla} M_{JM}\right) \cdot \left(\vec{\sigma} \times \frac{1}{q}\vec{\nabla}\right)$

Table A.2: Table of symbols and their corresponding expressions. The M_{JM} term in the equation refers to a nuclear response function that describes the charge or scalar response of the nucleus in interactions with dark matter. Specifically, M_{JM} represents the multipole operator associated with the charge operator in the nuclear medium. It is constructed from Bessel spherical harmonics and is defined as:$M_{JM}(q\vec{x}) \equiv j_J(qx) Y_{JM}\left(\Omega_x\right)$, where $j_J(qx)$ is a spherical Bessel function, and $Y_{JM}\left(\Omega_x\right)$ is a spherical harmonic that depends on the angles Ω_x.

The general form of Spherical Harmonics Y_{JM} and Spherical Bessel Functions j_J are

$$Y_{JM}(\theta, \phi) = (-1)^M \sqrt{\frac{(2J+1)}{4\pi} \frac{(J-M)!}{(J+M)!}} P_J^M(\cos\theta) e^{iM\phi} \tag{A.50}$$

$$j_J(qx) = (-qx)^J \left(\frac{1}{qx}\frac{d}{d(qx)}\right)^J \left(\frac{\sin(qx)}{qx}\right) \tag{A.51}$$

Where the P_J^M is the Legendre polynomials in quantum mechanics. With the convention of matrix element given above, the nuclear response function is defined by

$$W_X^{x,x'} = \sum_{J_T} \left\langle \Psi_f \left\| X_{J_T}^x \right\| \Psi_i \right\rangle \left\langle \Psi_i \left\| X_{J_T}^{x'} \right\| \Psi_f \right\rangle \tag{A.52}$$

$W_X^{x,x'}$ provides a measure of the response function of the nucleus to different types of dark matter-induced interactions. Where a, b denotes the single-particle orbitals, and the target one body density matrices $\rho_J^{fi}(a,b)$ can be given out by changing the basis to a, b as shown in Ref.[9] in order to represent the operators with orbital index with a normalising constant.

$$\left\langle \Psi_f \| X_{J_T}^x \| \Psi_i \right\rangle = \sum_{a,b} \left\langle a || X_{J_T}^x \| b \right\rangle \rho_J^{fi}(a,b) \tag{A.53}$$

Note that the density matrix usually has the form of $\rho = |\psi\rangle \langle\psi|$, but here we will expand the wavefunction with orthonormal basis with a, b as $|\psi\rangle = \sum_a |a\rangle \langle a| |\psi\rangle$, so the density matrix will be represented by

$$\rho = \left(\sum_a |a\rangle \langle a| |\psi\rangle \right) \left(\sum_b \langle\psi| |b\rangle \langle b| \right) = \sum_{a,b} \langle a| |\psi\rangle \langle\psi| |b\rangle |a\rangle \langle b| \tag{A.54}$$

So the density matrix with $|\Psi_{i,f}\rangle$ will in the form of $\rho_i = |\Psi_i\rangle \langle\Psi_i|, \quad \rho_f = |\Psi_f\rangle \langle\Psi_f|$, which have the matrix element

$$\rho_i(a,b) = \langle a \mid \Psi_i\rangle \langle\Psi_i \mid b\rangle, \quad \rho_f(a,b) = \langle a \mid \Psi_f\rangle \langle\Psi_f \mid b\rangle \tag{A.55}$$

$$\rho_{J_T}^{fi}(a,b) = \langle a \mid \Psi_f\rangle \langle\Psi_i \mid b\rangle \tag{A.56}$$

Then it could be inserted as the matrix element from the Eq.A.53 with the reduced matrix element $\left\langle a \left\| X_{J_T}^x \right\| b \right\rangle$ through the Wigner–Eckart theorem [9].

$$\left\langle \Psi_f \left\| X_{J_T}^x \right\| \Psi_i \right\rangle = \sum_{a,b} \left\langle a \left\| X_{J_T}^x \right\| b \right\rangle \langle a \mid \Psi_f\rangle \langle\Psi_i \mid b\rangle \tag{A.57}$$

Here we introduce $\hat{c}_a^\dagger$ and $\tilde{c}_b$ are the fermion creation for state $|a\rangle$ and annihilation operators for $|b\rangle$ that coupled to a total angular momentum J_T , and recover the basis by $\langle a \mid \Psi_f\rangle$ and $\langle\Psi_i \mid b\rangle$ through Eq.A.56

$$\rho_{J_T}^{fi}(a,b) = \langle\Psi_f| \left(|a\rangle \langle a| \left[\hat{c}_a^\dagger \otimes \tilde{c}_b \right]_{J_T} |b\rangle \langle b| \right) |\Psi_i\rangle \tag{A.58}$$

$$\rho_{J_T}^{fi}(a,b) = \frac{1}{\sqrt{2J_T+1}} \left\langle \Psi_f \left\| \left[\hat{c}_a^\dagger \otimes \tilde{c}_b \right]_{J_T} \right\| \Psi_i \right\rangle \tag{A.59}$$

The factor $\sqrt{2J_T+1}$ arises from the sum of all the magnetic quantum numbers of a spherical tensor operator. It accounts for the fact that a reduced matrix element is normalized over $2J_T+1$ magnetic substates. The potential energy interval for WIMP is around $10 - 1000$ GeV, the target nuclei for Xenon detector(Xenon isotopes) have masses around 130 atomic mass units that are equivalent to 121 GeV, only approximate 100 keV will transfer to the nucleus. So the initial and final states we expected are all in the ground state transitions $|\Psi_i\rangle = |\Psi_f\rangle$. Note that these will still affect the surface charge density, so that's why we could design to detect it [71, 72]. Mathematically the creation operator $\hat{c}_a^\dagger$ in matrix form, all the non-zero elements will be above the diagonal index:

$$\hat{c}_a^\dagger = \begin{pmatrix} 0 & 1 & 0 & 0 & \cdots \\ 0 & 0 & \sqrt{2} & 0 & \cdots \\ 0 & 0 & 0 & \sqrt{3} & \cdots \\ 0 & 0 & 0 & 0 & \cdots \\ \vdots & \vdots & \vdots & \vdots & \ddots \end{pmatrix} \tag{A.60}$$

The annihilation operator $\tilde{c}_b$ in matrix form:

$$\tilde{c}_b = \begin{pmatrix} 0 & 0 & 0 & 0 & \cdots \\ 1 & 0 & 0 & 0 & \cdots \\ 0 & \sqrt{2} & 0 & 0 & \cdots \\ 0 & 0 & \sqrt{3} & 0 & \cdots \\ \vdots & \vdots & \vdots & \vdots & \ddots \end{pmatrix} \tag{A.61}$$

For the detection theory part, we care about the cross-section and event rate. Integrating the nuclear response functions and transition probabilities can compute the cross section for dark matter-nucleus scattering. Derive the differential event rates, which describe the number of scattering events as a function of recoil energy [9]. With the dark matter flux $\Phi_\chi = n_\chi v$, and scattering rate for a single nucleus $R_{\text{single}} = \Phi_\chi \sigma(v)$, the differential scattering cross-section can be expressed as

$$\frac{\mathrm{d}R_{\text{single}}}{\mathrm{d}E_r} = \Phi_\chi \frac{\mathrm{d}\sigma}{\mathrm{d}E_r} \tag{A.62}$$

$\frac{\mathrm{d}\sigma}{\mathrm{d}E_r}$ is the differential scattering rate, and for the number of target nuclei R, the total rate for a detector containing N_T target nuclei are

$$\frac{\mathrm{d}R}{\mathrm{d}E_r} = N_T n_\chi v \frac{\mathrm{d}\sigma}{\mathrm{d}E_r}, E_r = \frac{{\mu_T}^2}{m_T} v^2 (1 - \cos\theta) \tag{A.63}$$

To account for all possible velocities, we integrate over the velocity distribution by DM particles.

$$\frac{\mathrm{d}R}{\mathrm{d}E_r} = N_T n_\chi \int \frac{\mathrm{d}\sigma}{\mathrm{d}E_r} v f(\vec{v}) \mathrm{d}^3 v \tag{A.64}$$

Converting the expression into the standard mass basis and truncating the velocity $v < v_{min}$

$$\frac{\mathrm{d}R}{\mathrm{d}E_r} = \frac{\rho_\chi}{m_\chi} \frac{N_T}{m_T} \int_{v \geq v_{\text{min}}} \frac{\mathrm{d}\sigma}{\mathrm{d}E_r} v f(\vec{v}) \mathrm{d}^3 v \tag{A.65}$$

The detectors' efficiencies $\varepsilon(E_r)$ depend on the recoil energy E_r. We introduce the detector efficiency, so the final expression for the differential event rate is:

$$\frac{\mathrm{d}N}{\mathrm{d}E_{\text{r}}} = \varepsilon(E_r) N_T n_\chi \int \frac{\mathrm{d}\sigma}{\mathrm{d}E_{\text{r}}} \tilde{f}(\vec{v}) |\vec{v}| \mathrm{d}^3 \vec{v} \tag{A.66}$$

Where the $\varepsilon(E_r)$ is the detector efficiency, N_T is the total number of target nuclei inside the detector. And the distribution of simple halo model $f(\vec{v})$ with $v_0 = 220$ km/s from the paper [71] is defined by

$$f(\vec{v}) = \frac{\Theta(v_{\text{esc}} - |\vec{v}|)}{\pi^{3/2} v_0^3 N_{\text{esc}}} e^{-\vec{v}^2/v_0^2} \tag{A.67}$$

Where the galactic escape velocity will cut-off at $v_{\rm esc} = 550$ km/s. Since $q^2 = 2m_T E_T$, the DM-nucleus interaction for a particular isotope differential cross-section with target mass m_T can be expressed as

$$\frac{\mathrm{d}\sigma}{\mathrm{d}E_r} = \frac{2m_T}{4\pi v^2} T(v,q) \tag{A.68}$$

Then, the DM-Nuclei interaction can be effectively treated as a two-body scattering problem. The total unpolarized differential cross-section can be evaluated by summing over the Mandelstam variables s, t, and u channels, with the scattering amplitude $\mathcal{M}$:

$$\frac{dR}{dE_R} = \frac{\rho_\chi m_T}{\mu_T^2 m_\chi v} \frac{d\sigma}{d\cos\theta} \tag{A.69}$$

where R represents the event rate, ρ_χ is the local dark matter density, m_T is the target mass, μ_T is the reduced mass of the dark matter and nucleus system, and v is the relative velocity of the dark matter particle.

The differential cross-section is expressed as:

$$\frac{d\sigma}{d\cos\theta} = \frac{1}{2J_\chi + 1} \frac{1}{2J_T + 1} \sum_{\text{spins}} \frac{1}{32\pi} \frac{|\mathcal{M}|^2}{(m_\chi + m_T)^2} \tag{A.70}$$

where J_χ and J_T are the total angular momenta of the dark matter particle and the target nucleus, respectively. The term $|\mathcal{M}|^2$ represents the square of the scattering amplitude, averaged over initial and summed over final spin states.

The DM-nucleus scattering probability can be calculated using the total angular momentum operator J and the magnetic operator M. With the Hamiltonian $\mathcal{H}$ for the allowed interaction as shown in Eq. A.46 and the operators listed in Table A.1, the scattering probability is given by the Fermi's Golden Rule (FGR) as:

$$T(v,q) = \frac{1}{2J_\chi + 1} \frac{1}{2J_T + 1} \sum_{M_i, M_f} |\langle J_T M_f | \mathcal{H} | J_T M_i \rangle|^2 = \frac{1}{2J_\chi + 1} \frac{1}{2J_T + 1} |\langle J_T \| \mathcal{H} \| J_T \rangle|^2 \tag{A.71}$$

This expression allows us to determine the transition probabilities between different nuclear states caused by dark matter scattering, as discussed in Ref. [5]. The final transition probability due to the electro-weak operators in Table A.2, specifically for $i = 7 \to M\Phi''$ and $i = 8 \to \Delta\Sigma'$, is given by:

$$T(v,q) = \frac{4\pi}{2J_T + 1} \sum_{x=N} \sum_{x'=N} \sum_{i=1}^{8} R_i^{x,x'}(v^2, q^2) W_i^{x,x'}(q) \tag{A.72}$$

The spin-independent nuclear response function, which depends on the charge distribution for the nuclear matrix element $W_i^{x,x'}$, is given by:

$$\langle J_f \| M_J(q) \| J_i \rangle \propto \int d^3r \, \rho(\vec{r}) \, j_J(q\vec{r}) \, Y_{JM}(\Omega_r) \tag{A.73}$$

Where $\rho(\vec{r})$ is the charge density distribution of the nucleus and the spherical function are shown below the Tab.A.2, and $Y_{JM}(\Omega_r)$ is the spherical harmonic, describing the angular dependence. Under the Long-Wavelength limit for low momentum transfer case, the nuclear response will be dominated by the total charge distribution inside the nucleus(number of protons Z) $\langle J_f \| M_J(q) \| J_i \rangle \propto Z^2$, and the charge density directly determines the response.

$$\langle J_f \| M_J(q) \| J_i \rangle \propto \int d^3 r \rho(\vec{r}) \tag{A.74}$$

To calculate the total ground state energy for a specific nucleus, we need to use the nuclear pairing model, a more complex nuclear Hamiltonian model [10]. The total progress to calculate the DM-Nuclei scattering in our project has been shown in the Fig.A.2 below.

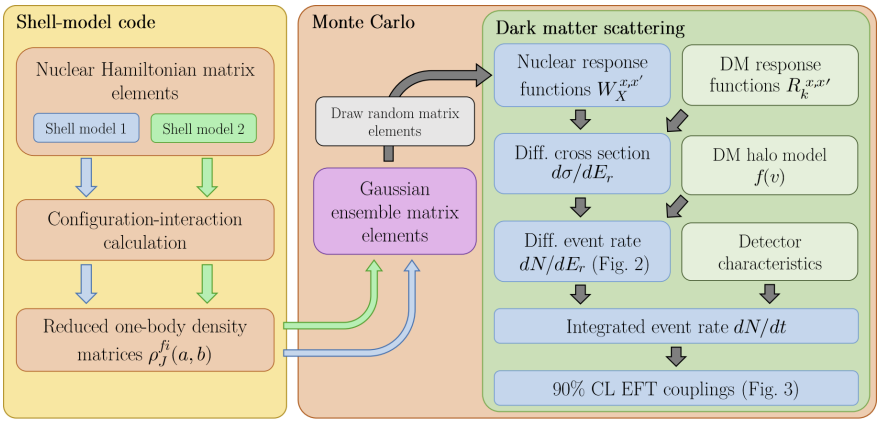

Figure A.2: A schematic illustrating the general procedure for calculating upper limits on dark matter-nucleon effective field theory coupling coefficients, along with the propagation of uncertainties from configuration-interaction calculations for a specific isotope [9, 10]. The Shell-model code will be used to analyse the spectrum of the nucleons, with generated matrix elements contributing to the nuclear response function. The derivation and calculation of event rates will give out the EFT couplings.

The challenge of analyzing nuclear responses to external probes, such as dark matter scattering, lies in the complexity of many-body systems, where transition probabilities between valence nucleon configurations are encoded in reduced matrix elements and the density matrix. These systems present significant numerical challenges when handled by classical computational methods. The sheer scale of data and computational power required to model large atomic nuclei often becomes prohibitively expensive. This has motivated researchers to explore alternative, more efficient computational methods, including the application of quantum information processing [8].

Quantum computing offers a potential solution by leveraging its inherent parallelism to simulate and analyze complex nuclear interactions more efficiently than classical methods [10]. By employing advanced quantum algorithms, such as the Variational Quantum Eigensolver (VQE) [34], we can bypass manually fitting wave functions or performing resource-intensive calculations. Instead, we use the quantum platform to iteratively optimize the parameters of a trial wave function until convergence, enabling us to simulate the ground state energy of large nucleon systems such as Fluorine, Helium, Xenon, and Argon [73]. This approach addresses the scalability challenges of classical methods and enhances our ability to model increasingly complex nuclear configurations.

With these motivations in mind, we now apply these ideas within the EFT framework for a more realistic calculation of dark matter-nuclei interactions. In the next section, we explore a practical application of EFT to model and calculate scattering processes.

A.1.3 EFT-Based Realistic Calculations for Dark Matter-Nucleon Scattering

In this section, we aim to provide a simple case for calculating the nuclear response to dark matter interactions within the framework of EFT. The wave function $\psi(\mathbf{r})$ of a nucleus in its ground state can be modelled as:

$$\psi(\mathbf{r}) = \left(\frac{\alpha}{\pi}\right)^{3/4} \exp\left(-\frac{\alpha \mathbf{r}^2}{2}\right) \tag{A.75}$$

For simplicity, we will use the simplest scalar interaction operator $\mathcal{O}_1 = 1_\chi 1_N$ as the total Hamiltonian for this calculation, where $\mathcal{O}_1$ corresponds to a spin-independent scalar interaction. The total Hamiltonian is then given by:

$$\mathcal{H} = c_1^x \mathcal{O}_1^x \tag{A.76}$$

Since we are focusing on the simplest scenario, the coefficient c_1^x is set to 1, as there is only one possible interaction. For this example, we consider **Deuterium** (the hydrogen-1 isotope) as the target nucleus, which consists of one proton and one neutron. The WIMP-nucleus response function for this interaction is:

$$R_1^{x,x'} = |\langle f\,|\mathcal{O}_1|\,i\rangle|^2 \tag{A.77}$$

Since we are dealing with spin-independent interactions, we use the Wigner-Eckart Theorem to express the matrix element of the nuclear response operator $X_{JT} = M_{JM}(q) = j_L(qx)Y_{JM}(\Omega)$, where j_L is the spherical Bessel function and Y_{JM} is the spherical harmonic. The matrix element is given by:

$$\langle f\,|X_{JT}|\,i\rangle = \langle f||\Sigma_{JT}||i\rangle \times (\text{Clebsch-Gordan coefficients}) \tag{A.78}$$

The nuclear target response function $W_X(q)$ can then be written as:

$$W_X(q) = \sum_{J,T} \langle \Psi_f \,\|M_{JM}(q)\|\, \Psi_i\rangle^2 = \sum_{J,T} \langle f||j_L(qx)Y_{JM}(\Omega)||i\rangle\, \langle i\,\|j_L(qx)Y_{JM}(\Omega)\|\, f\rangle\, F(q) \tag{A.79}$$

For a nucleus like protium (a single proton), the charge density ρ is simply the charge distribution of the proton itself. This simplifies the form factor $F(q)$ for low momentum transfer, as the internal structure of the nucleus is not probed.

Under the long-wavelength approximation for low momentum transfer q, the spherical Bessel function can be expanded in a series:

$$j_L(qx) \sim \frac{(qx)^L}{(2L+1)!!} \quad \text{for small } q \tag{A.80}$$

Where the !! denotes the double factorial. For $L = 0$ case, the spherical Bessel function becomes:

$$j_0(qx) = \frac{\sin(qx)}{qx} \tag{A.81}$$

For small qx (i.e., in the long-wavelength approximation, where the momentum transfer is small compared to the size of the nucleus), this can be approximated as:

$$j_0(qx) \approx 1 - \frac{(qx)^2}{6} + \mathcal{O}\left((qx)^4\right) \tag{A.82}$$

In the limit of small $\boldsymbol{q}$, the higher-order terms can be neglected, and we obtain $(qx) \approx 1$, which means the nucleus behaves like a point charge and its internal structure is not resolved. Since the monopole operator $M_{00}(q)$ corresponds to the spherical harmonic $Y_{00}(\Omega)$ (which is just a constant) and the spherical Bessel function $j_0(qx) \approx 1$, the whole operator $M_{00}(q)$ simplifies to approximately 1 for small q.

In general, the form factor of target nucleus can be written as $F(q) = \frac{1}{Z}\int \rho(\vec{x})e^{i\vec{q}\cdot\vec{x}}d^3x$, If we assume the charge distribution of the nucleus is spherically symmetric and can be approximated by a Gaussian distribution:

$$\rho(r) = \frac{Z}{(2\pi R^2)^{3/2}} \exp\left(-\frac{r^2}{2R^2}\right) \tag{A.83}$$

$$F(q) = \frac{2\pi}{Z}\int_0^\infty \frac{Z}{(2\pi R^2)^{3/2}} \exp\left(-\frac{r^2}{2R^2}\right) \frac{\sin(qr)}{qr} r^2 dr \tag{A.84}$$

This integral can be computed analytically. The standard result for an integral of this form is:

$$\int_0^\infty r^2 \exp\left(-\frac{r^2}{2R^2}\right) \frac{\sin(qr)}{qr} dr = \frac{\sqrt{\pi}R^3}{2} \exp\left(-\frac{q^2R^2}{6}\right) \tag{A.85}$$

In the long-wavelength approximation, $F(q) \approx 1 - \frac{q^2R^2}{6} \approx \exp\left(-\frac{q^2R^2}{6}\right)$. The final form of the target nucleus response will be

$$W_X(q) = |F(q)|^2 = \exp\left(-\frac{q^2R_d^2}{3}\right) \tag{A.86}$$

where R_d is the Deuteron radius. The root-mean-square (RMS) charge radius of deuterium is approximately $R_d \approx 2.13$fm, which includes contributions from both the proton and the neutron. The expression for differential cross-section with mass $m_d \approx 1.8756\text{GeV/c}^2$ will be

$$\frac{d\sigma}{dE_r} = \frac{m_d}{2\pi v^2} R(q)|F(q)|^2 = \frac{2m_T}{4\pi v^2} T(v,q) \tag{A.87}$$

The momentum transfer q is related to the recoil energy E_r by the expression $q = \sqrt{2m_dE_r}$, substituting everything into the expression for the differential cross-section, we have:

$$\frac{d\sigma}{dE_r} = \frac{m_d}{2\pi v^2} \exp\left(-\frac{q^2R_d^2}{3}\right) \tag{A.88}$$

To calculate the total cross-section σ, we integrate over the recoil energy E_r :

$$\sigma = \int_0^{E_r^{\max}} \frac{d\sigma}{dE_r} dE_r \tag{A.89}$$

where $E_r^{\max}$ is the maximum possible recoil energy, which can be approximated as:

$$E_r^{\max} = \frac{2\mu^2 v^2}{m_d} \tag{A.90}$$

where $\mu = \frac{m_\chi m_d}{m_\chi + m_d}$ is the reduced mass of the dark matter particle (m_χ) and the deuteron (m_d). Substituting the expression for $\frac{d\sigma}{dE_T}$:

$$\sigma = \int_0^{E_r^{\max}} \frac{m_d}{2\pi v^2} \exp\left(-\frac{2m_dE_rR_d^2}{3}\right) dE_r \tag{A.91}$$

This integral can be computed analytically. Let's denote the constant factor $A = \frac{2m_dR_d^2}{3}$. Thus, the integral becomes:

$$\sigma = \frac{m_d}{2\pi v^2} \int_0^{E_r^{\max}} \exp\left(-AE_r\right) dE_r \tag{A.92}$$

The integral of $\exp(-Ax)$ is straight forward to get:

$$\int_0^{E_r^{\max}} \exp\left(-AE_r\right) dE_r = \frac{1-\exp\left(-AE_r^{\max}\right)}{A} \tag{A.93}$$

Thus, the total cross-section is:

$$\sigma = \frac{m_d}{2\pi v^2 A}\left(1-\exp\left(-AE_r^{\max}\right)\right) \tag{A.94}$$

Substitute $A = \frac{2m_d R_d^2}{3}$ and $E_r^{\max}$, we can get the **total cross-section** for the dark matter-deuteron interaction.

$$\sigma = \frac{3}{4\pi v^2 R_d^2}\left(1-\exp\left(-\frac{4\mu^2 v^2 R_d^2}{3m_d}\right)\right) \tag{A.95}$$

So, the scattering transition probability based on Eq. A.56 with the recoil energy E_r can be simplified as:

$$T(v,q) = \frac{4\pi}{2j_T+1} R^1_{x,x'}(v^2,q^2) W^1_{x,x'}(q) \tag{A.96}$$

Given that we are working with spin-independent interactions, and using the Wigner-Eckart Theorem to extract the matrix element, the probability becomes:

$$T(v,q) = \frac{4\pi}{2j_T+1}\left|\langle f\left|\mathcal{O}_1\right|i\rangle\right|^2 \exp\left(-\frac{q^2R_d^2}{3}\right) \tag{A.97}$$

Substituting for the spin-independent operator $\mathcal{O}_1 = 1_\chi 1_N$, we have:

$$T(v,q) = \frac{4\pi}{2j_T+1}\left|\langle \psi_f\left|1_\chi 1_N\right|\psi_i\rangle\right|^2 \exp\left(-\frac{(\sqrt{2m_dE_r})^2R_d^2}{3}\right) \tag{A.98}$$

Here, R_d is the deuteron radius, and m_d is the deuteron mass. The event rate R for dark matter detection can now be expressed based on the local dark matter density ρ_χ, the differential cross-section $\frac{d\sigma}{dE_r}$, and the dark matter velocity distribution $f(v)$:

$$R = \frac{\rho_\chi}{m_\chi}\int_{v_{\min}}^{v_{\max}} \frac{d\sigma}{dE_r} f(v)\vec{v}\, dv \tag{A.99}$$

Where:

- ρ_χ is the local dark matter density (approximately $0.3\,\mathrm{GeV/cm^3}$),
- m_χ is the mass of the dark matter particle,
- $f(v)$ is the velocity distribution of dark matter particles in the galactic halo.

This final expression allows us to compute the expected event rate based on the velocity and energy distribution of the dark matter particles.

A.2 Experimental Methods for Detecting Dark Matter

Nowadays, several leading experiments use direct detection for particle DM and visible matters like XENONnT and PandaX-4T [6, 7]. In order to detect dark matter interactions, experimental setups must be designed to maximize sensitivity to rare scattering events. Some apparatus have other aiming also could be used to detect the WIMP candidates like CUORE [74], using the TeO_2 crystals as the target, element like Xenon, which has a large number of nucleons (more than hundreds) will be modelled through nuclear configuration-interactions.

Like XENONnT, PandaX-4T's primary goal is to detect WIMPs [6, 7]. It is built underground at 2400m under a mountain in China, and a water shell surrounds the two-phase Xenon(Gas, Fulid) in a Time Projection Chamber(TPC) with self-shielding features to reduce radiation noise, so most of the cosmic rays and background noise can be reduced due to the shell absorption [75]. The Photomultiplier Tubes will be fixed at the top and bottom of the detector, which will be used to detect the flash caused by the event so we can recover the information of the captured event. These experiments are typically located deep underground to reduce interference from cosmic rays and other background radiation.

The detection mechanism can be decomposed into two steps: for primary scintillation, when a WIMP collides with a xenon nucleus in the detector, it can transfer energy to the nucleus, causing the nucleus to recoil [7]. It excites xenon atoms, causing them to emit ultraviolet scintillation light (S1). For secondary scintillation, the recoiling nucleus also ionizes surrounding xenon atoms. An electric field in the chamber drifts these ionization electrons to the gas phase above the liquid xenon, producing secondary scintillation light (S2) as they accelerate through the gas.

The signal of S1 and S2 allows researchers to recover the event position in 3D and its time and energy by analysing the nuclear response. So, it is essential to know how to build a nuclear response theory to use it effectively. In summary, the workflow of the detection experiment can be concluded as

1. **Detector Setup and Calibration:** This step involves setting up the PandaX-4T detector, including installing the liquid xenon target and calibrating the detector systems (like photomultiplier tubes, electric fields, etc.) to ensure accurate data collection.

2. **Data Collection (Cryogenic Conditions):** The detector operates at cryogenic temperatures to keep xenon in a liquid state. Data is collected during this phase by detecting scintillation (S1) and ionization (S2) signals generated by interactions within the detector.

3. **Data Processing (Signal Filtering and Calibration):** Raw data collected from the detector is processed to filter out noise and calibrate the signals, ensuring that only valid interaction events are retained for further analysis.

4. **Event Reconstruction (S1 and S2 Signal Identification):** This step involves reconstructing events from the processed signals and identifying and classifying S1 and S2 signals to determine the energy and position of potential dark matter interactions.

5. **Data Analysis (Event Selection and Background Reduction):** The reconstructed events are analysed to select events consistent with expected dark matter signatures while reducing backgrounds from known radioactive sources or other noise.

6. **Results Interpretation (Dark Matter Limits and Signal Search):** The analyzed data is interpreted to search for evidence of dark matter particles. This involves setting limits on the dark matter-nucleon cross-section or identifying potential signals.

A.3 Noisy Channel

To describe the qubit noise via the quantum channel, we will first define some operators, such as the Karus operator [76, 77].

Kraus operators denoted as $\{K_i\}$, are used to represent the evolution of open quantum systems. The completeness relation defines them:

$$\sum_i K_i^\dagger K_i = I \tag{A.100}$$

where $K_i^\dagger$ is the adjoint of K_i, and I is the identity operator. The evolution of a quantum state ρ is given by:

$$\rho \to \rho' = \sum_i K_i \rho K_i^\dagger \tag{A.101}$$

Measurements in quantum mechanics can also be represented using Kraus operators. For a projective measurement described by projectors $\{P_k\}$, the Kraus operators are simply $K_k = P_k$. Upon the quantum measurement, if we ignore the measurement error then the state of the system collapses according to:

$$\rho \to \frac{P_k \rho P_k}{\mathrm{Tr}\,(P_k \rho)} \tag{A.102}$$

With the definition above, any quantum channel $\mathcal{E}$ can be represented as a sum of unitary operations:

$$\mathcal{E}(\rho) = \sum_i p_i U_i \rho U_i^\dagger \tag{A.103}$$

where $\{U_i\}$ are unitary operators and $\{p_i\}$ are probabilities. This form is sometimes called a random unitary channel, which is a special case where each Kraus operator can be associated with a unitary transformation and a probability.

Here in Fig.A.3, the phase flip and the depolarizing channel for the noisy quantum channel are shown below.

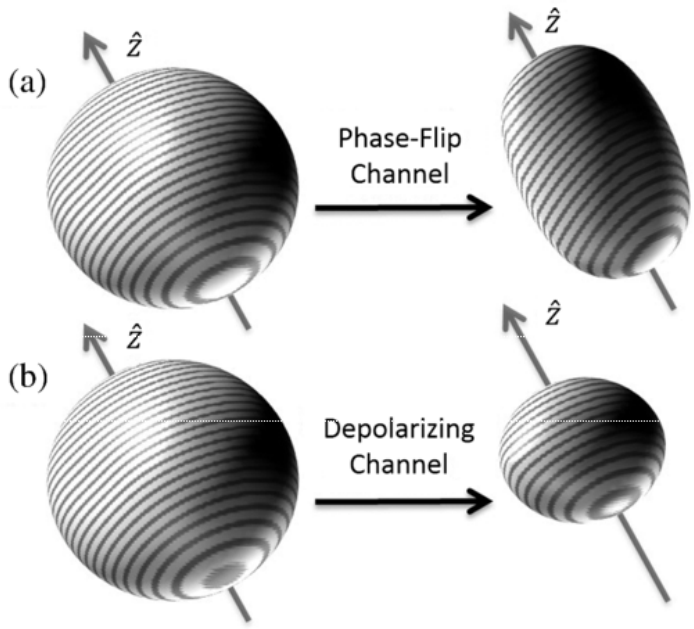

Figure A.3: Illustration of the effects of noise channels on a quantum state represented on the Bloch sphere [77]. The initial state is represented by the left Bloch sphere in both subfigures, while the right Bloch spheres show the effects of different noise channels: (a) The Phase-Flip Channel: This channel flips the phase of the quantum state, leading to a distortion along the z-axis. (b) The Depolarizing Channel: This channel randomizes the state, causing the Bloch sphere to shrink uniformly towards the centre.

Notably, there is a difference between the quantum operation and the quantum channel, a key to identifying the quantum channel is trace-preserving of the density matrix, a subset from the quantum operation, which holds completely positive (CP) and non-trace-increasing maps on the space of density matrices [78]. Since the trace operation is linear, and using the condition for trace preservation $\sum_i K_i^\dagger K_i = I$, we substitute to get:

$$\mathrm{Tr}(\mathcal{E}(\rho)) = \mathrm{Tr}\left(\rho \sum_i K_i^\dagger K_i\right) = \mathrm{Tr}(\rho I) = \mathrm{Tr}(\rho) \tag{A.104}$$

We summarized the different types of channels below:

- **Depolarizing Channel**: This channel randomly flips the state of a qubit with a certain probability, effectively mixing the quantum state with the maximally mixed state. It represents a uniform distribution of errors affecting all qubit states equally.

- **Dephasing Channel**: This channel causes phase errors, leading to the loss of coherence between the components of a superposition state. Dephasing errors are particularly detrimental to algorithms relying on quantum interference.

- **Amplitude Damping Channel**: This channel models energy dissipation processes, where qubits relax from an excited state to the ground state, resulting in the loss of quantum information.

A.4 Zero Noise Extrapolation

The core idea of ZNE is to intentionally increase the noise level in a quantum circuit and then extrapolate back to a "zero noise" level to estimate the error-free outcome. This process involves

running the quantum circuit multiple times with varying levels of artificially introduced noise [53, 79]. The main component for this strategy is unitary folding, both for circuit and operation since for any ideal quantum transformation U have the property $U^\dagger U = I$.

$$U \to U \left(U^\dagger U\right)^n \tag{A.105}$$

For a rotation gate $R(\theta_j)$, the noise effect can be regarded as an extra term on the parameter $\theta'_j = \theta_j + \hat{\epsilon}_j$, here is an idea to reduce that term that is scaling the noise term [79].

$$\theta'_j \xrightarrow{\text{parameter noise scaling}} \theta'_j + \hat{\delta}_j \tag{A.106}$$

$$\theta'_j = \theta_j + \sqrt{\lambda}\hat{\epsilon}_j \tag{A.107}$$

On the right of Fig.A.4, a graph plots the expectation value of interest against the noise amplification/stretch factor. The blue dots represent measured expectation values $E(c_1\lambda)$ and $E(c_2\lambda)$ at different stretch factors c_1 and c_2. The red dashed line is an extrapolation towards zero noise (stretch factor of 0), predicting the noise-free expectation value E^*. The shaded regions indicate uncertainty in the measurements and extrapolation. This visual demonstrates how varying the noise level and extrapolating to zero allows for estimating an error-free result. We can gather a range of noisy outputs by systematically varying the noise levels (using different values of λ). These outputs are then used to extrapolate back to the result in the absence of noise. This process helps reduce the effect of noise without the need for additional qubits for error correction, which is particularly beneficial for near-term quantum devices that are limited in both qubit count and coherence time. We will perform an extrapolation to mitigate the noise and estimate the ideal expectation value E^* as shown in Fig.A.4.

$$E(\lambda_i) = E^* + \alpha\lambda_i + \mathcal{O}\left(\lambda_i^2\right) \tag{A.108}$$

$$E^* \approx \frac{c_2 E(c_1\lambda) - c_1 E(c_2\lambda)}{c_2 - c_1} \tag{A.109}$$

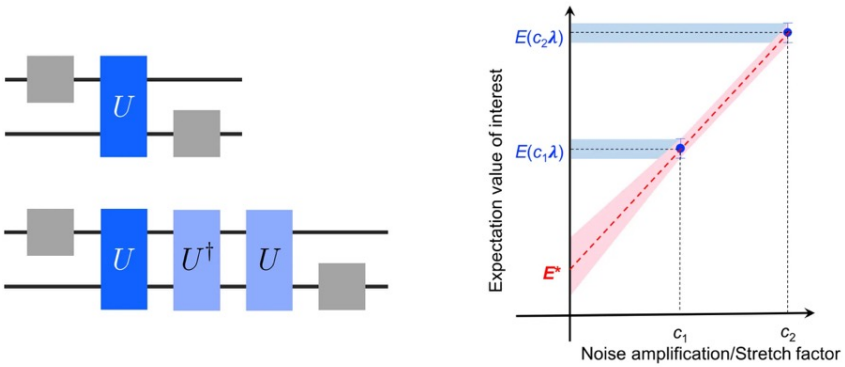

Figure A.4: The figure illustrates the concept of ZNE for quantum error mitigation. On the left, two quantum circuits are shown. In the left subfigure, the top circuit represents the original circuit with a unitary operation U. The bottom circuit demonstrates a noise amplification technique by appending an identity operation through a combination of U and its inverse $U^\dagger$, followed by U again, effectively tripling the gate count to stretch the noise [12].

For U=CNOT operation, ideally when noiseless the form of $U^\dagger$ is

$$U^\dagger = U = \begin{bmatrix} 1 & 0 & 0 & 0 \\ 0 & 1 & 0 & 0 \\ 0 & 0 & 0 & 1 \\ 0 & 0 & 1 & 0 \end{bmatrix}, UU^\dagger U = U \tag{A.110}$$

In our project, we assume all of the single-qubit operations are nearly perfect, and the depolarisation error will dominate on the two-qubit gates of CNOT; to investigate the features of CNOT noise extrapolation, such as linear or polynomial fitting, we will insert multiple extra two more CNOT operations to utilise ZNE analysis by extending the fitting curve back to where the noise level tends to zero $E^* = \lim_{\lambda \to 0} E(\lambda)$.

A.5 Probabilistic Error Cancellation

Probabilistic error cancellation (PEC) is a quantum error mitigation technique designed to reduce errors in quantum computations without requiring a full error-correcting code [80]. In PEC, the error-prone quantum operations are effectively "inverted" using a probabilistic mixture of noisy operations, allowing one to estimate the ideal, error-free result. This process works by statistically cancelling out errors: the noise affecting the quantum gates is carefully modelled, and a series of correction operations are applied, weighted by probabilities that account for the error model. While PEC does not eliminate errors, it significantly reduces them, allowing for more accurate quantum computations at the cost of increased sampling overhead, as the probabilistic nature of the process requires a larger number of measurements to achieve reliable results. PEC is particularly valuable on near-term quantum devices, where error rates are high and full quantum error correction is not yet feasible.

In PEC, the ideal target circuit's effect can be represented as a linear combination of implementable noisy circuits:

$$\mathcal{O}_{\text{ideal}} = \sum_i \eta_i \mathcal{O}_{\text{noisy},i} \tag{A.111}$$

The ideal circuit's outcome is thus reproduced by sampling from an ensemble of noisy circuits defined by this linear combination. When the coefficients η_i form a probability distribution, they directly serve as ensemble probabilities. However, if some η_i are negative, they constitute a quasiprobability distribution. This distribution induces a sampling overhead related to its negativity, characterized by

$$\gamma = \sum_i |\eta_i| \geq 1 \tag{A.112}$$

$$\mathcal{O}_{\text{ideal}} = \left(\sum_i \eta_i \right) \mathcal{O}_{\text{ideal}} + \sum_i \eta_i \Delta_i \tag{A.113}$$

To cancel noise, the coefficients η_i are chosen such that

$$\sum_i \eta_i = 1 \quad \text{and} \quad \sum_i \eta_i \Delta_i = 0. \tag{A.114}$$

Here is a PEC workflow using Mitiq, which is also compatible with QISKIT [12]. The process begins with a quantum program defined by the user, which is processed by Mitiq's PEC module. Mitiq generates a set of probabilistically sampled circuits, each representing a noisy version of the

ideal target circuit. These noisy circuits are executed on quantum hardware, producing measurement results that are then returned to Mitiq. Finally, Mitiq aggregates these measurement results to infer an error-mitigated expectation value for the quantum program, minimizing the impact of noise.

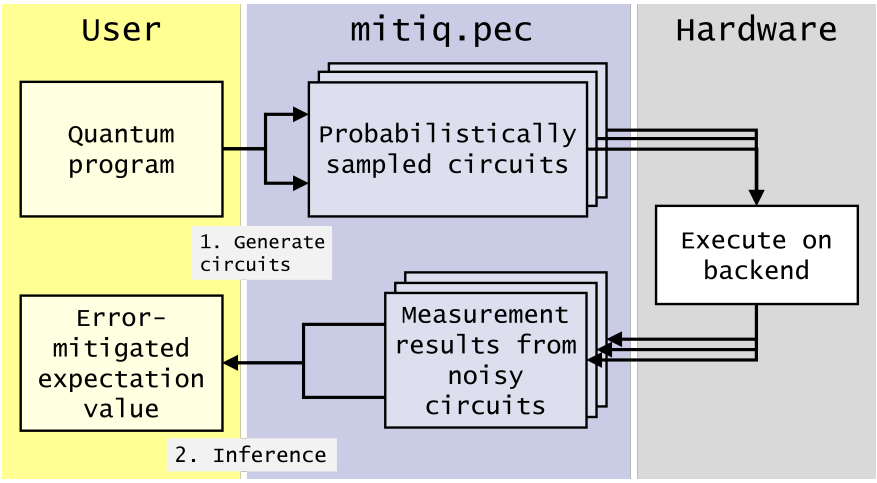

Figure A.5: The user defines a quantum program, which Mitiq translates into a collection of noisy circuits sampled based on a quasi-probability distribution. These circuits, designed to statistically counteract noise, are run on the quantum hardware, and the results are gathered back into Mitiq. By averaging these noisy results according to the quasi-probability weights, Mitiq reconstructs an expectation value close to what the ideal, noise-free circuit would produce. This approach leverages classical post-processing to approximate the ideal outcome.

A.6 Quantum Error Suppression

A.6.1 Dynamical Decoupling

Dynamical decoupling (DD) is a quantum error mitigation technique designed to reduce decoherence in quantum systems by periodically applying control pulses [81]. In NISQ devices, where decoherence and other noise sources limit qubit coherence times, DD is a valuable strategy for preserving quantum information during computation. The core idea of DD is to apply sequences of gate operations that counteract certain types of noise, effectively "refocusing" the quantum state and mitigating errors.

In DD, a sequence of unitary operations $\{U_1, U_2, \ldots, U_n\}$ is applied to an idle qubit during idle intervals of the computation, typically satisfying the condition:

$$U_n U_{n-1} \cdots U_1 = I \tag{A.115}$$

where I is the identity operation. This ensures that the sequence has no net effect on the qubit's state in the absence of noise. However, in the presence of noise, the sequence cancels out certain noise terms, effectively reducing decoherence.

One common DD sequence is the XX sequence, in which X gates (Pauli X operators) are applied at regular intervals.

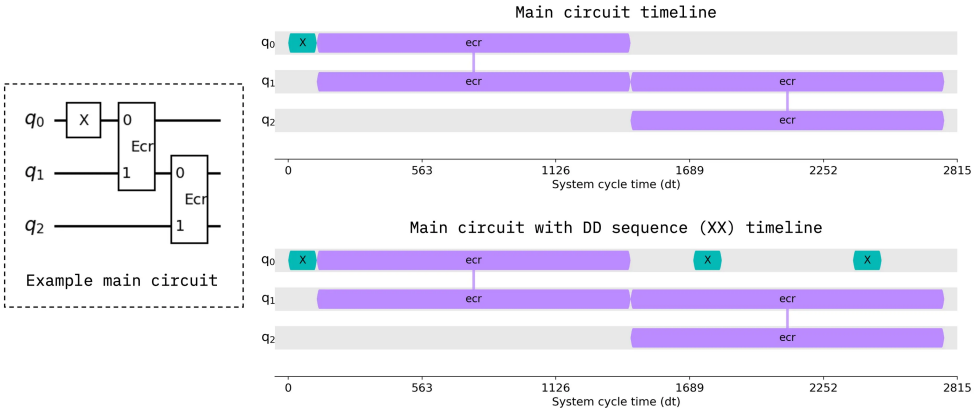

Figure A.6: Example quantum circuit and its execution timelines with and without dynamical decoupling using the XX sequence. The circuit on the left shows a sample setup with single and two-qubit gates: an X gate on qubit q_0 and two ECR gates acting on qubit pairs (q_0, q_1) and (q_1, q_2). The "Main circuit timeline" in the top right shows the timing and order of gate execution without any DD pulses. The "Main circuit with DD sequence (XX) timeline" below it shows the same circuit, but with additional X gates (representing the XX dynamical decoupling sequence) inserted at regular intervals. These added X gates help mitigate decoherence by effectively refocusing certain types of noise, particularly for idle qubits, during the execution of other gates. Ref. [12]

However, if the operations in the circuit are densely packed, keeping the qubits occupied most of the time and adding dynamic decoupling pulses may not enhance performance. It could potentially degrade performance due to imperfections in the pulses themselves.

A.6.2 Pauli Gate Twirling

There is a solution for the randomized noise channel on quantum devices called Pauli Twirling [82]. Unlike Dynamical Decoupling, this strategy will insert extra gates and cause higher time costs on the QPU, so in the application, it will be deployed only on the noisy gate.

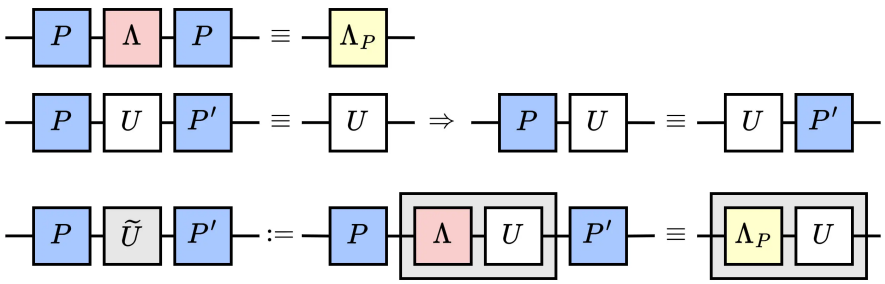

Figure A.7: Illustration of Pauli twirling applied to a noisy quantum operation. In the first row, Pauli twirling transforms a noisy channel Λ into an effective depolarized channel Λ_P by randomly applying a Pauli gate P before and after the channel. In the second row, a unitary operation U is sandwiched by Pauli gates P and P', resulting in a twirled unitary U that behaves equivalently in the twirling ensemble. The third row shows an effective noise model for the noisy unitary $\tilde{U}$, where the Pauli twirling operation creates a composite noise channel Λ_P combined with the unitary U, achieving a depolarized effect across the sequence. This sequence illustrates how Pauli twirling randomizes the errors in a quantum operation, making the resulting noise more uniform and transforming arbitrary noise into a form that resembles depolarizing noise, simplifying error characterization and mitigation in quantum circuits. Ref.[12]

In near-term devices, most of the errors come from multi-qubit gates like CNOT and ECR, so most of the time, this strategy is designed for two-qubit gates. The Fig.A.8 shows the process of applying gate twirling sequence on them.

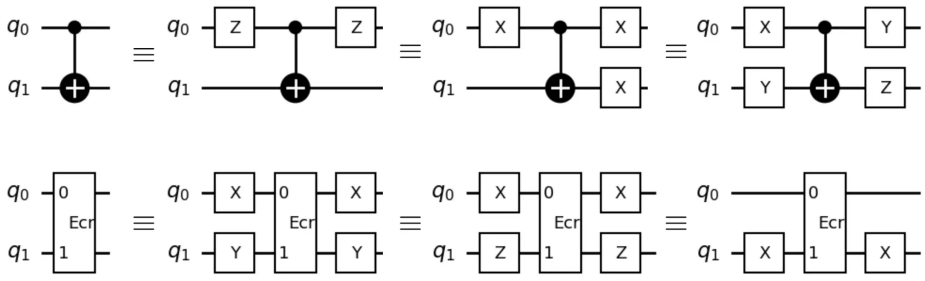

Figure A.8: Illustration of Pauli twirling for two-qubit gates using Pauli gates and the ECR gate. The top row demonstrates the Pauli twirling of a CNOT gate by applying different combinations of Pauli gates (X, Y, Z) before and after the gate, effectively altering the noise characteristics. Each configuration of Pauli gates produces an equivalent operation that behaves uniformly under noise averaging, achieving a depolarizing effect.

The bottom row shows the Pauli twirling applied to the ECR gate. Similar to the CNOT gate, various Pauli gates (X, Y, Z) are applied before and after the ECR gate, creating different but equivalent configurations. This procedure ensures that the noise introduced by the ECR gate becomes isotropic, transforming the noise into a depolarizing form and simplifying error analysis and correction.

A.7 Quantum Error Correction

In this section, we will review the single error correction, which means the error could be X, Y, Z. But only the method to correct X, Z is needed due to the Y could be represented by the combination of the other two X, Z [83, 84].

An X error, or bit-flip error, occurs when a qubit's state is flipped from $|0\rangle$ to $|1\rangle$ or from $|1\rangle$ to $|0\rangle$. Mathematically, this is represented by the application of the Pauli-X operator:

$$X = \begin{bmatrix} 0 & 1 \\ 1 & 0 \end{bmatrix}$$

Here is the method to correct the single X errors.

1. **Encoding:** The logical qubit state $|\psi\rangle = a|0\rangle + b|1\rangle$ is encoded into a three-qubit state:

$$|0_L\rangle = |000\rangle, \quad |1_L\rangle = |111\rangle$$

   The general encoded state is:

$$|\psi_L\rangle = a|000\rangle + b|111\rangle$$

2. **Error Detection:** After encoding, each qubit can undergo a bit-flip error, and the state might become, for example, $a|010\rangle + b|101\rangle$ if the second qubit is flipped. To detect an error, we measure two syndromes:

   - Measure Z_1Z_2 and Z_2Z_3 operators (parity checks between qubits 1 and 2, and qubits 2 and 3).
   - Each parity check reveals whether there is an error between the corresponding pair of qubits.

3. **Error Correction:** Based on the syndrome outcomes:

   - If both measurements return 0, no error is detected.
   - If $Z_1Z_2 = -1$ and $Z_2Z_3 = +1$, the first qubit is likely in error, apply an X gate to correct it.
   - Similarly, if $Z_1Z_2 = +1$ and $Z_2Z_3 = -1$, the third qubit is likely in error, apply an X gate to correct it.
   - If both syndromes return -1, correct the middle qubit.

A Z error, or phase-flip error, changes the relative phase of the qubit's superposition state. The phase flip occurs between the $|0\rangle$ and $|1\rangle$ states and is represented by the Pauli-Z operator:

$$Z = \begin{bmatrix} 1 & 0 \\ 0 & -1 \end{bmatrix}$$

To correct a Z error, we use a similar method to the three-qubit repetition code but adapted for phase-flip errors:

1. **Encoding:** The logical qubit state $|\psi\rangle = a|0\rangle + b|1\rangle$ is encoded into a three-qubit state in the phase basis. To detect phase errors, the encoded states are:

$$|+_L\rangle = |+++\rangle, \quad |-_L\rangle = |---\rangle$$

where $|+\rangle = \frac{|0\rangle+|1\rangle}{\sqrt{2}}$ and $|-\rangle = \frac{|0\rangle-|1\rangle}{\sqrt{2}}$.
The general encoded state is:

$$|\psi_L\rangle = a|+++\rangle + b|---\rangle$$

2. **Error Detection:** After encoding, each qubit can undergo a phase-flip error, and the state might become, for example, $a|+-+\rangle + b|-+-\rangle$ if the second qubit is flipped. To detect an error, we measure two syndromes:

   - Measure X_1X_2 and X_2X_3 operators (parity checks between the phase states of qubits 1 and 2, and qubits 2 and 3).
   - Each parity check reveals whether there is a phase error between the corresponding pair of qubits.

3. **Error Correction:** Based on the syndrome outcomes:

   - If both measurements return 0, no error is detected.
   - If $X_1X_2 = -1$ and $X_2X_3 = +1$, the first qubit is likely in error, apply a Z gate to correct it.
   - Similarly, if $X_1X_2 = +1$ and $X_2X_3 = -1$, the third qubit is likely in error, apply a Z gate to correct it.
   - If both syndromes return -1, correct the middle qubit with a Z gate.

The method given above can detect and correct all of the single qubit errors. However, in real quantum computing, multiple errors could also occur, and strategies like Shor code could be deployed to solve them [83, 85, 86].

A.8 Matrix Product State

Matrix Product States (MPS) are a versatile and highly efficient framework for representing quantum states in many-body systems, particularly in one-dimensional (1D) quantum lattices [12, 63]. The MPS formalism leverages the intrinsic structure of entanglement in quantum systems, allowing for a compact representation of quantum states that would otherwise require an exponentially large number of parameters. By expressing the quantum state as a product of matrices associated with each site in the system, MPS efficiently encode correlations and entanglement, making them a powerful tool for both theoretical studies and numerical simulations [87, 88]. The many-body quantum state $|\Psi\rangle$ can be decomposed in to the square matrices product form with the given basis with number of eigen state s(for qubit s up to 2).

$$|\Psi\rangle = \sum_s \mathrm{Tr}\left[A_1^{(s_1)} A_2^{(s_2)} \cdots A_N^{(s_N)}\right] |s_1 s_2 \ldots s_N\rangle \tag{A.116}$$

The structure can be demonstrated as the Fig.A.9
Like for an N-qubit entangled state, which is called GHZ state.

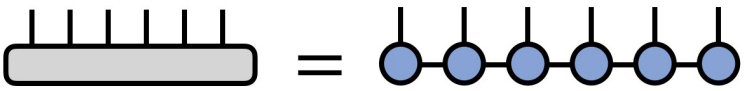

Figure A.9: On the left, the entire quantum state is represented as a single tensor (grey block), while on the right, the same state is decomposed into a series of interconnected smaller tensors (blue circles). Each circle represents a local tensor, and the lines connecting them indicate the entanglement or correlations between different parts of the quantum system. The vertical lines correspond to physical indices (local states), and the horizontal lines represent virtual indices (bond dimensions) that capture the entanglement between subsystems. This decomposition allows for efficient representation and computation of quantum states, particularly in one-dimensional systems with limited entanglement.

$$|\mathrm{GHZ}\rangle = \frac{|0\rangle^{\otimes N} + |1\rangle^{\otimes N}}{\sqrt{2}} \tag{A.117}$$

It can be decomposed by the square matrices $A^{(0,1)}$

$$A^{(0)} = \begin{bmatrix} 1 & 0 \\ 0 & 0 \end{bmatrix} \quad A^{(1)} = \begin{bmatrix} 0 & 0 \\ 0 & 1 \end{bmatrix} \tag{A.118}$$

So, for $N = 3$ case, the total form can be expressed by the tensor product of three body, and the coefficients stored in our computer algorithms could be reduced from $2 \cdot 2^3 = 16 \to 4$:

$$AAA = \begin{bmatrix} |000\rangle & 0 \\ 0 & |111\rangle \end{bmatrix} \tag{A.119}$$

Note that this method will be quicker and have less memory cost than the density matrix and state vector simulation method, so it is the most often used method in our program.

A.9 Previous Work about the Lipkin Model

Quantum computing is needed for the Lipkin-Meshkov-Glick model (LMG model, also known as the Lipkin model) and other similar many-body systems due to the exponential growth in the complexity of classical calculations as the system size increases. Classical computation methods face significant challenges in handling the large Hilbert spaces and intricate interactions in heavy and complex nuclei. Quantum computers, with their ability to efficiently simulate quantum systems, offer a promising alternative. They can potentially perform these calculations with higher accuracy and less computational cost, enabling more precise modelling of nuclear structures. This is particularly crucial for applications like dark matter detection, where accurate modelling of nuclear targets is essential for interpreting experimental results and understanding the fundamental interactions between dark matter and baryonic matter [89].

The Lipkin model describes a system comprising N fermions [90, 91]. The Lipkin model is an essential testbed for studying many-body interactions in nuclear physics. Classical computation methods struggle with the exponential growth of the Hilbert space as the number of particles increases, leading to significant computational challenges, especially for heavy, complex nuclei. The model assumes N particles are distributed over N sites, with each particle being either in an 'up' or 'down' state, simplifying the complex interactions into single-particle energies and two-particle interactions.

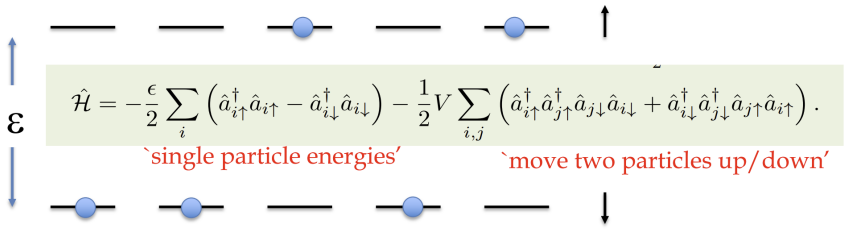

Figure A.10: The first term of the Lipkin Hamiltonian, $-\frac{\epsilon}{2}\sum_i \left(\hat{a}^\dagger_{i\uparrow}\hat{a}_{i\uparrow} - \hat{a}^\dagger_{i\downarrow}\hat{a}_{i\downarrow}\right)$, accounts for the single-particle energies. The second term, $-\frac{1}{2}V\sum_{i,j}\left(\hat{a}^\dagger_{i\uparrow}\hat{a}^\dagger_{j\uparrow}\hat{a}_{j\downarrow}\hat{a}_{i\downarrow} + \hat{a}^\dagger_{i\downarrow}\hat{a}^\dagger_{j\downarrow}\hat{a}_{j\uparrow}\hat{a}_{i\uparrow}\right)$, represents the two-particle interactions [89].

For the Fig A.10, the parameter ϵ denotes the energy difference between the single-particle states. The operators $\hat{a}^\dagger_{i\uparrow}$ and $\hat{a}^\dagger_{i\downarrow}$ are creation operators for particles in the spin-up and spin-down states, respectively, and $\hat{a}_{i\uparrow}$ and $\hat{a}_{i\downarrow}$ are the corresponding annihilation operators. The parameter V is the interaction strength. This term describes processes where two particles are either moved to a higher energy state or a lower one. These fermions are apportioned among two energy levels, each level exhibiting an N-fold degeneracy with an energy separation denoted by ϵ. Here, the fermionic creation and annihilation operators for a fermion in state p at level σ, where σ can be either $+1$ or -1, are defined as $c^\dagger_{\sigma p}$ and $c_{\sigma p}$, respectively. Reviewing the previous work based on the nuclear physics, the Hamiltonian of the system is then expressed as:

$$\begin{aligned}\tilde{H} =& \frac{1}{2}\epsilon\sum_{\sigma,p}\sigma c^\dagger_{\sigma p}c_{\sigma p} \\ &+ \frac{1}{2}\bar{V}\sum_{\sigma,p,p'} c^\dagger_{\sigma p}c^\dagger_{\sigma p'}c_{-\sigma p'}c_{-\sigma p}.\end{aligned} \tag{A.120}$$

Here it is essential to introduce the quasi-spin operators to simplify the Hamiltonian form

$$\begin{aligned}J_+ &= \sum_p c^\dagger_{+1p}c_{-1p} = (J_-)^\dagger \\ J_0 &= \frac{1}{2}\sum_{\sigma,p}\sigma c^\dagger_{\sigma p}c_{\sigma p}\end{aligned} \tag{A.121}$$

So the Hamiltonian form could be rewritten as

$$\tilde{H} = \epsilon J_0 + \frac{1}{2}\tilde{V}\left(J^2_+ + J^2_-\right) \tag{A.122}$$

For the N particles case, the total quasi-spin could be written as $\mathbf{J} = \sum_{p=1}^N \mathbf{J}^{(p)}$, with the representation of the new Hamiltonian form and to adapt the $SU(2)$ algebra for qubits

$$H = \sum_{p=1}^N J_0^{(p)} + V\sum_{\substack{p,q=1\\ q\neq p}}^N \left(J_+^{(p)}J_+^{(q)} + J_-^{(q)}J_-^{(p)}\right) \tag{A.123}$$

To analyze the Hamiltonian, we need to define an appropriate basis. For the $N = 3$ case, the basis states can be represented by the eigenstates of the Pauli matrices σ_x, σ_y, and σ_z, which

describe the spin states of the qubits. The basis states for three qubits can be written as tensor products of the individual qubit states from Eq 3.1, such as $|000\rangle$, $|001\rangle$, $|010\rangle$, etc. The Hamiltonian in Eq.A.123 could be represented by the sum of the Pauli product form

$$\begin{aligned} H \doteq & \frac{1}{2}\left(\sigma_3 \otimes 1 \otimes 1 + 1 \otimes \sigma_3 \otimes 1 + 1 \otimes 1 \otimes \sigma_3\right) \\ & + \frac{V}{2}\left(1 \otimes \sigma_1 \otimes \sigma_1 + \sigma_1 \otimes \sigma_1 \otimes 1 + \sigma_1 \otimes 1 \otimes \sigma_1\right. \\ & \left. -1 \otimes \sigma_2 \otimes \sigma_2 - \sigma_2 \otimes \sigma_2 \otimes 1 - \sigma_2 \otimes 1 \otimes \sigma_2\right) \end{aligned} \tag{A.124}$$

Then we can expand the Eq 4.5 to the matrix form by the given basis, where the operator 1 will be relevant to the identity matrix.

$$RHS = \begin{pmatrix} \frac{3}{2} & 0 & 0 & V & 0 & V & V & 0 \\ 0 & \frac{1}{2} & 0 & 0 & 0 & 0 & 0 & V \\ 0 & 0 & \frac{1}{2} & 0 & 0 & 0 & 0 & V \\ V & 0 & 0 & -\frac{1}{2} & 0 & 0 & 0 & 0 \\ 0 & 0 & 0 & 0 & \frac{1}{2} & 0 & 0 & V \\ V & 0 & 0 & 0 & 0 & -\frac{1}{2} & 0 & 0 \\ V & 0 & 0 & 0 & 0 & 0 & -\frac{1}{2} & 0 \\ 0 & V & V & 0 & V & 0 & 0 & -\frac{3}{2} \end{pmatrix} \tag{A.125}$$

The optimal variational ansatz(trial wave function) by doing the exact diagonalization to get the exact solution described by the parameter θ (with the normalized relation $cos(\theta)^2 + sin(\theta)^2 = 1$) given by

$$\begin{aligned} |\psi(\theta)\rangle = & \cos(\theta)|\downarrow\downarrow\downarrow\rangle \\ & - \frac{1}{\sqrt{3}}\sin(\theta)(|\uparrow\uparrow\downarrow\rangle + |\uparrow\downarrow\uparrow\rangle + |\downarrow\uparrow\uparrow\rangle), \end{aligned} \tag{A.126}$$

With $\alpha \equiv 2\arccos\left(-\sqrt{\frac{2}{3}}\sin\theta\right)$, $\beta \equiv -\frac{\pi}{4} - \arctan\left(\frac{\tan\theta}{\sqrt{3}}\right)$, the quantum circuit can be shown as

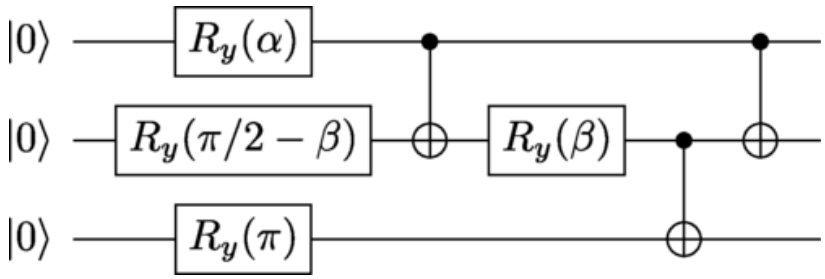

Figure A.11: The quantum *Ansatz* for Lipkin model of $N = 3$ case to prepare the three-qubit VQE trial state, which prepares a three-qubit VQE trial state using rotational gates and CNOT gates to entangle the qubits. Parameters α and β are represented by θ, and all the qubits will connected by the CNOT gates [90]. The mathematical definition for the gates can be found in Eq $3.7 - 3.10$.

Then, the ground state energy of this case could be estimated using the VQE algorithm via quantum estimator, which involves iterating the parameters to the optimal point.

References

1. Prézeau, G. DENSE DARK MATTER HAIRS SPREADING OUT FROM EARTH, JUPITER, AND OTHER COMPACT BODIES. *The Astrophysical Journal* **814,** 122. ISSN: 1538-4357. http://dx.doi.org/10.1088/0004-637X/814/2/122 (2015-11).
2. Group, P. Planck2013 results. I. Overview of products and scientific results. *Astronomy amp; Astrophysics* **571,** A1. ISSN: 1432-0746. http://dx.doi.org/10.1051/0004-6361/201321529 (2014-10).
3. Bertone, G., Hooper, D. & Silk, J. Particle dark matter: evidence, candidates and constraints. *Physics Reports* **405,** 279–390. ISSN: 0370-1573. http://dx.doi.org/10.1016/j.physrep.2004.08.031 (2005-01).
4. Bertone, G. & Hooper, D. History of dark matter. *Reviews of Modern Physics* **90.** ISSN: 1539-0756. http://dx.doi.org/10.1103/RevModPhys.90.045002 (2018-10).
5. Fitzpatrick, A. L., Haxton, W., Katz, E., Lubbers, N. & Xu, Y. The effective field theory of dark matter direct detection. *Journal of Cosmology and Astroparticle Physics* **2013,** 004 (2013).
6. Search for New Physics in Electronic Recoil Data from XENONnT. *Physical Review Letters* **129.** ISSN: 1079-7114. http://dx.doi.org/10.1103/PhysRevLett.129.161805 (2022-10).
7. Meng, Y. *et al.* Dark Matter Search Results from the PandaX-4T Commissioning Run. *Physical Review Letters* **127.** ISSN: 1079-7114. http://dx.doi.org/10.1103/PhysRevLett.127.261802 (2021-12).
8. Bharti, K. *et al.* Noisy intermediate-scale quantum algorithms. *Rev. Mod. Phys.* **94,** 015004. https://link.aps.org/doi/10.1103/RevModPhys.94.015004 (1 2022-02).
9. Heimsoth, D. J. *et al.* Uncertainties on the EFT coupling limits for direct dark matter detection experiments stemming from uncertainties of target properties. *Phys. Rev. D* **108,** 103031. https://link.aps.org/doi/10.1103/PhysRevD.108.103031 (10 2023-11).
10. Office of Science, U.S. Department of Energy. *High Energy Physics Quantum Information Science Abstracts 2020* https://science.osti.gov/-/media/_/pdf/initiatives/qis/HEP-QIS-Abstracts-2020.pdf. Accessed: November 8, 2024.
11. Arute, F. *et al.* Quantum supremacy using a programmable superconducting processor. *Nature* **574,** 505–510. https://doi.org/10.1038/s41586-019-1666-5 (2019).
12. Javadi-Abhari, A. *et al. Quantum computing with Qiskit* 2024. arXiv: 2405.08810 [quant-ph].
13. Preskill, J. Quantum Computing in the NISQ era and beyond. *Quantum* **2,** 79. ISSN: 2521-327X. https://doi.org/10.22331/q-2018-08-06-79 (2018-08).
14. Pan, F. & Zhang, P. Simulation of Quantum Circuits Using the Big-Batch Tensor Network Method. *Phys. Rev. Lett.* **128,** 030501. https://link.aps.org/doi/10.1103/PhysRevLett.128.030501 (3 2022-01).
15. Robledo, L. *et al.* High-fidelity projective read-out of a solid-state spin quantum register. *Nature* **477,** 574–578 (2011).

16. Schrader, D. *et al.* Neutral atom quantum register. *Physical Review Letters* **93,** 150501 (2004).

17. Blok, M. S. *et al.* Quantum information scrambling on a superconducting qutrit processor. *Physical Review X* **11,** 021010 (2021).

18. Kasirajan, V. in *Fundamentals of Quantum Computing: Theory and Practice* 75–104 (Springer International Publishing, Cham, 2021). ISBN: 978-3-030-63689-0. https://doi.org/10.1007/978-3-030-63689-0_3.

19. Kurzyński, P., Kołodziejski, A., Laskowski, W. & Markiewicz, M. Three-dimensional visualization of a qutrit. *Physical Review A* **93,** 062126 (2016).

20. Wikipedia contributors. *Unpolarized light – Poincaré sphere* https://en.wikipedia.org/wiki/Unpolarized_light{#}Poincar%C3%A9_sphere. Accessed: 2024-06-17. 2024.

21. Gaebler, J. P. *et al.* High-fidelity universal gate set for be 9+ ion qubits. *Physical review letters* **117,** 060505 (2016).

22. Dawson, C. M. & Nielsen, M. A. The solovay-kitaev algorithm. *arXiv preprint quant-ph/0505030* (2005).

23. Zindorf, B. & Bose, S. *Quantum Computing with Hermitian Gates* 2024. arXiv: 2402.12356 [quant-ph]. https://arxiv.org/abs/2402.12356.

24. Georgescu, I. M., Ashhab, S. & Nori, F. Quantum simulation. *Reviews of Modern Physics* **86,** 153–185 (2014).

25. Sieberer, L. M. *et al.* Digital quantum simulation, trotter errors, and quantum chaos of the kicked top. *npj Quantum Information* **5,** 78 (2019).

26. Poulin, D., Qarry, A., Somma, R. & Verstraete, F. Quantum Simulation of Time-Dependent Hamiltonians¡? format?¿ and the Convenient Illusion of Hilbert Space. *Physical review letters* **106,** 170501 (2011).

27. Bravyi, S. B. & Kitaev, A. Y. Fermionic Quantum Computation. *Annals of Physics* **298,** 210–226. ISSN: 0003-4916. http://dx.doi.org/10.1006/aphy.2002.6254 (2002-05).

28. Ollitrault, P. J., Baiardi, A., Reiher, M. & Tavernelli, I. Hardware efficient quantum algorithms for vibrational structure calculations. *Chemical Science* **11,** 6842–6855. ISSN: 2041-6539. http://dx.doi.org/10.1039/d0sc01908a (2020).

29. Tranter, A., Love, P. J., Mintert, F. & Coveney, P. V. A comparison of the Bravyi–Kitaev and Jordan–Wigner transformations for the quantum simulation of quantum chemistry. *Journal of chemical theory and computation* **14,** 5617–5630 (2018).

30. Nielsen, M. A. *et al.* The Fermionic canonical commutation relations and the Jordan-Wigner transform. *School of Physical Sciences The University of Queensland* **59,** 75 (2005).

31. Streltsov, A. I., Alon, O. E. & Cederbaum, L. S. General mapping for bosonic and fermionic operators in Fock space. *Physical Review A—Atomic, Molecular, and Optical Physics* **81,** 022124 (2010).

32. Tan, X. *Quantum Computing for Phonon Scattering Effects on Thermal Conductivity* 2024. arXiv: 2407.15808 [quant-ph]. https://arxiv.org/abs/2407.15808.

33. Miessen, A., Ollitrault, P. J. & Tavernelli, I. Quantum algorithms for quantum dynamics: A performance study on the spin-boson model. *Phys. Rev. Res.* **3,** 043212. https://link.aps.org/doi/10.1103/PhysRevResearch.3.043212 (4 2021-12).

34. Peruzzo, A. *et al.* A variational eigenvalue solver on a photonic quantum processor. *Nature Communications* **5.** ISSN: 2041-1723. http://dx.doi.org/10.1038/ncomms5213 (2014-07).

35. Sayginel, H., Jamet, F., Agarwal, A., Browne, D. E. & Rungger, I. *A fault-tolerant variational quantum algorithm with limited T-depth* 2023. arXiv: 2303.04491 [quant-ph]. https://arxiv.org/abs/2303.04491.

36. Clemente, G., Crippa, A., Jansen, K. & Tüysüz, C. *New Directions in Quantum Music: concepts for a quantum keyboard and the sound of the Ising model* 2022. arXiv: 2204.00399.

37. Kandala, A. *et al.* Error mitigation extends the computational reach of a noisy quantum processor. *Nature* **567,** 491–495. ISSN: 1476-4687. https://doi.org/10.1038/s41586-019-1040-7 (2019).

38. Ziman, M. & Bužek, V. All (qubit) decoherences: Complete characterization and physical implementation. *Physical Review A—Atomic, Molecular, and Optical Physics* **72,** 022110 (2005).

39. Dewes, A. *et al.* Characterization of a two-transmon processor with individual single-shot qubit readout. *Physical review letters* **108,** 057002 (2012).

40. Schlosshauer, M. Quantum decoherence. *Physics Reports* **831,** 1–57. ISSN: 0370-1573. http://dx.doi.org/10.1016/j.physrep.2019.10.001 (2019-10).

41. Helsen, J., Roth, I., Onorati, E., Werner, A. & Eisert, J. General Framework for Randomized Benchmarking. *PRX Quantum* **3,** 020357. https://link.aps.org/doi/10.1103/PRXQuantum.3.020357 (2 2022-06).

42. Torlai, G., Wood, C., Acharya, A., *et al.* Quantum process tomography with unsupervised learning and tensor networks. *Nature Communications* **14,** 2858. https://doi.org/10.1038/s41467-023-38332-9 (2023).

43. Mohseni, M., Rezakhani, A. T. & Lidar, D. A. Quantum-process tomography: Resource analysis of different strategies. *Physical Review A—Atomic, Molecular, and Optical Physics* **77,** 032322 (2008).

44. Cai, Z. *et al.* Quantum error mitigation. *Reviews of Modern Physics* **95,** 045005 (2023).

45. Endo, S., Benjamin, S. C. & Li, Y. Practical quantum error mitigation for near-future applications. *Physical Review X* **8,** 031027 (2018).

46. Jozsa, R. Fidelity for Mixed Quantum States. *Journal of Modern Optics* **41,** 2315–2323. eprint: https://doi.org/10.1080/09500349414552171. https://doi.org/10.1080/09500349414552171 (1994).

47. Knill, E. *et al.* Randomized benchmarking of quantum gates. *Physical Review A* **77.** ISSN: 1094-1622. http://dx.doi.org/10.1103/PhysRevA.77.012307 (2008-01).

48. Huang, W. *et al.* Fidelity benchmarks for two-qubit gates in silicon. *Nature* **569,** 532–536 (2019).

49. Devitt, S. J., Munro, W. J. & Nemoto, K. Quantum error correction for beginners. *Reports on Progress in Physics* **76,** 076001 (2013).

50. Filippov, S. N., Maniscalco, S. & García-Pérez, G. *Scalability of quantum error mitigation techniques: from utility to advantage* 2024. arXiv: 2403.13542 [quant-ph]. https://arxiv.org/abs/2403.13542.

51. Miguel-Ramiro, J. *et al.* Superposed Quantum Error Mitigation. *Phys. Rev. Lett.* **131,** 230601. https://link.aps.org/doi/10.1103/PhysRevLett.131.230601 (23 2023-12).

52. Hicks, R., Kobrin, B., Bauer, C. W. & Nachman, B. Active readout-error mitigation. *Phys. Rev. A* **105,** 012419. https://link.aps.org/doi/10.1103/PhysRevA.105.012419 (1 2022-01).

53. Cai, Z. *et al.* Quantum error mitigation. *Rev. Mod. Phys.* **95,** 045005. https://link.aps.org/doi/10.1103/RevModPhys.95.045005 (4 2023-12).

54. Cross, A. W., Bishop, L. S., Sheldon, S., Nation, P. D. & Gambetta, J. M. Validating quantum computers using randomized model circuits. *Physical Review A* **100.** ISSN: 2469-9934. http://dx.doi.org/10.1103/PhysRevA.100.032328 (2019-09).

55. LaRose, R., Mari, A., Russo, V., Strano, D. & Zeng, W. J. *Error mitigation increases the effective quantum volume of quantum computers* 2022. arXiv: 2203.05489 [quant-ph]. https://arxiv.org/abs/2203.05489.

56. Van der Schoot, W., Wezeman, R., Eendebak, P. T., Neumann, N. M. P. & Phillipson, F. Evaluating three levels of quantum metrics on quantum-inspire hardware. *Quantum Information Processing* **22.** ISSN: 1573-1332. http://dx.doi.org/10.1007/s11128-023-04184-x (2023-12).

57. Hochstuhl, D., Hinz, C. M. & Bonitz, M. Time-dependent multiconfiguration methods for the numerical simulation of photoionization processes of many-electron atoms. *The European Physical Journal Special Topics* **223,** 177–336. https://doi.org/10.1140/epjst/e2014-02092-3 (2014).

58. Gorton, O. C., Johnson, C. W., Jiao, C. & Nikoleyczik, J. dmscatter: A fast program for WIMP-nucleus scattering. *Computer Physics Communications* **284,** 108597. ISSN: 0010-4655. http://dx.doi.org/10.1016/j.cpc.2022.108597 (2023-03).

59. Cambiaggio, M. C. & Piastino, A. Quasi spin pairing and the structure of the Lipkin Model. *Z Physik A* **288,** 153–159 (1978).

60. Frauendorf, S. & Macchiavelli, A. Overview of Neutron-Proton Pairing. *Progress in Particle and Nuclear Physics* **78** (2014-05).

61. Virtanen, P. *et al.* SciPy 1.0: Fundamental Algorithms for Scientific Computing in Python. *Nature Methods* **17,** 261–272 (2020).

62. Pellow-Jarman, A., Sinayskiy, I., Pillay, A. & Petruccione, F. A comparison of various classical optimizers for a variational quantum linear solver. *Quantum Information Processing* **20.** ISSN: 1573-1332. http://dx.doi.org/10.1007/s11128-021-03140-x (2021-06).

63. Crosswhite, G. M. & Bacon, D. Finite automata for caching in matrix product algorithms. *Phys. Rev. A* **78,** 012356. https://link.aps.org/doi/10.1103/PhysRevA.78.012356 (1 2008-07).

64. Wang, J., Guo, G. & Shan, Z. SoK: Benchmarking the Performance of a Quantum Computer. *Entropy* **24,** 1467. https://www.mdpi.com/1099-4300/24/10/1467 (2022).

65. Funcke, L. *et al.* Measurement error mitigation in quantum computers through classical bit-flip correction. *Physical Review A* **105.** ISSN: 2469-9934. http://dx.doi.org/10.1103/PhysRevA.105.062404 (2022-06).

66. Burkert, V. D. *Nucleon resonances and transition form factors* 2022. arXiv: 2212.08980 [hep-ph]. https://arxiv.org/abs/2212.08980.

67. Anand, N., Fitzpatrick, A. L. & Haxton, W. C. Weakly interacting massive particle-nucleus elastic scattering response. *Physical Review C* **89.** ISSN: 1089-490X. http://dx.doi.org/10.1103/PhysRevC.89.065501 (2014-06).

68. Collaboration, 5. *et al. Effective field theory interactions for liquid argon target in DarkSide-50 experiment* 2020. arXiv: 2002.07794 [hep-ex]. https://arxiv.org/abs/2002.07794.

69. Akerib, D. S. *et al.* Constraints on effective field theory couplings using 311.2 days of LUX data. *Physical Review D* **104.** ISSN: 2470-0029. http://dx.doi.org/10.1103/PhysRevD.104.062005 (2021-09).

70. Racah, G. Theory of Complex Spectra. II. *Phys. Rev.* **62,** 438–462. https://link.aps.org/doi/10.1103/PhysRev.62.438 (9-10 1942-11).

71. Drukier, A. K., Freese, K. & Spergel, D. N. Detecting cold dark-matter candidates. *Phys. Rev. D* **33,** 3495–3508. https://link.aps.org/doi/10.1103/PhysRevD.33.3495 (12 1986-06).

72. Freese, K., Frieman, J. & Gould, A. Signal modulation in cold-dark-matter detection. *Phys. Rev. D* **37,** 3388–3405. https://link.aps.org/doi/10.1103/PhysRevD.37.3388 (12 1988-06).

73. Akerib, D. S. *et al. Snowmass2021 Cosmic Frontier Dark Matter Direct Detection to the Neutrino Fog* 2022. arXiv: 2203.08084 [hep-ex]. https://arxiv.org/abs/2203.08084.

74. Arnaboldi, C. *et al.* CUORE: a cryogenic underground observatory for rare events. *Nuclear Instruments and Methods in Physics Research Section A: Accelerators, Spectrometers, Detectors and Associated Equipment* **518,** 775–798. ISSN: 0168-9002. http://dx.doi.org/10.1016/j.nima.2003.07.067 (2004-02).

75. Ahlen, S. *et al.* First dark matter search results from a surface run of the 10-L DMTPC directional dark matter detector. *Physics Letters B* **695,** 124–129. ISSN: 0370-2693. http://dx.doi.org/10.1016/j.physletb.2010.11.041 (2011-01).

76. Sudarshan, E. C. G., Mathews, P. M. & Rau, J. Stochastic Dynamics of Quantum-Mechanical Systems. *Physical Review* **121,** 920–924. ISSN: 0031-899X (1961-02).

77. Caruso, F., Giovannetti, V., Lupo, C. & Mancini, S. Quantum channels and memory effects. *Rev. Mod. Phys.* **86,** 1203–1259. https://link.aps.org/doi/10.1103/RevModPhys.86.1203 (4 2014-12).

78. Shaji, A. & Sudarshan, E. Who's afraid of not completely positive maps? *Physics Letters A* **341,** 48–54. ISSN: 0375-9601. https://www.sciencedirect.com/science/article/pii/S0375960105005748 (2005).

79. Giurgica-Tiron, T., Hindy, Y., LaRose, R., Mari, A. & Zeng, W. J. *Digital zero noise extrapolation for quantum error mitigation* in *2020 IEEE International Conference on Quantum Computing and Engineering (QCE)* (IEEE, 2020-10). http://dx.doi.org/10.1109/QCE49297.2020.00045.

80. Mari, A., Shammah, N. & Zeng, W. J. Extending quantum probabilistic error cancellation by noise scaling. *Phys. Rev. A* **104,** 052607. https://link.aps.org/doi/10.1103/PhysRevA.104.052607 (5 2021-11).

81. Ezzell, N., Pokharel, B., Tewala, L., Quiroz, G. & Lidar, D. A. Dynamical decoupling for superconducting qubits: A performance survey. *Physical Review Applied* **20.** ISSN: 2331-7019. http://dx.doi.org/10.1103/PhysRevApplied.20.064027 (2023-12).

82. Geller, M. R. & Zhou, Z. Efficient error models for fault-tolerant architectures and the Pauli twirling approximation. *Physical Review A* **88.** ISSN: 1094-1622. http://dx.doi.org/10.1103/PhysRevA.88.012314 (2013-07).

83. Roffe, J. Quantum error correction: an introductory guide. *Contemporary Physics* **60,** 226–245. ISSN: 1366-5812. http://dx.doi.org/10.1080/00107514.2019.1667078 (2019-07).

84. Chiaverini, J. *et al.* Realization of quantum error correction. *Nature* **432,** 602–605. https://doi.org/10.1038/nature03074 (2004).

85. Huang, S., Brown, K. R. & Cetina, M. *Comparing Shor and Steane Error Correction Using the Bacon-Shor Code* 2023. arXiv: 2312.10851 [quant-ph]. https://arxiv.org/abs/2312.10851.

86. Knill, E. Quantum computing with realistically noisy devices. *Nature* **434,** 39–44. ISSN: 1476-4687. http://dx.doi.org/10.1038/nature03350 (2005-03).

87. Vidal, G. Efficient Classical Simulation of Slightly Entangled Quantum Computations. *Physical Review Letters* **91.** ISSN: 1079-7114. http://dx.doi.org/10.1103/PhysRevLett.91.147902 (2003-10).

88. Schollwöck, U. The density-matrix renormalization group in the age of matrix product states. *Annals of Physics* **326,** 96–192. ISSN: 0003-4916. http://dx.doi.org/10.1016/j.aop.2010.09.012 (2011-01).

89. Johnson, C. *The Lipkin Model* https://indico.cern.ch/event/826783/contributions/4929986/attachments/2480004/4257124/johnson_calvin_dubrovnik_2.pdf. Accessed: 2024-07-10.

90. Cervia, M. J. *et al.* Lipkin model on a quantum computer. *Phys. Rev. C* **104,** 024305. https://link.aps.org/doi/10.1103/PhysRevC.104.024305 (2 2021-08).

91. Beaujeault-Taudiere, Y. & Lacroix, D. *Solving the Lipkin model using quantum computers with two qubits only with a hybrid quantum-classical technique based on the Generator Coordinate Method* 2023. arXiv: 2312.04703 [quant-ph]. https://arxiv.org/abs/2312.04703.